Nanostructured Materials and Electrodes Engineering for Efficient CO_2 Conversion

by

Guobin Wen

A thesis

presented to the University of Waterloo

in fulfillment of the

thesis requirement for the degree of

Doctor of Philosophy

in

Chemical Engineering

Waterloo, Ontario, Canada, 2020

Examining Committee Membership

The following served on the Examining Committee for this thesis. The decision of the Examining Committee is by majority vote.

External Examiner	Prof. **Ali Seifitokaldani** Department of Chemical Engineering, McGill University
Supervisors	Prof. **Zhongwei Chen** Department of Chemical Engineering, University of Waterloo
	Prof. **Jeff Gostick** Department of Chemical Engineering, University of Waterloo
Internal Member	Prof. **Eric Croiset** Department of Chemical Engineering, University of Waterloo
Internal Member	Prof. **David Simakov** Department of Chemical Engineering, University of Waterloo
Internal-external Member	Prof. **Zhongchao Tan** Department of Mechanical & Mechatronics Engineering, University of Waterloo

Author’s Declaration

I hereby declare that this thesis consists of materials, all of which I authored or co-authored: see Statement of Contributions included in the thesis. This is a true copy of the thesis, including any required final revisions, as accepted by my examiners.

I understand that my thesis may be made electronically available to the public.

Statement of Contributions

The body of this thesis is based upon a combination of published papers. Various chapters are adapted from the following list of publications.

Chapter 3 of this thesis consists of the following paper that was co-authored by myself, my supervisors, two Ph.D. students (Bohua Ren and Zachary P. Cano), and six collaborators (Dong Un Lee, Fathy M. Hassan, Gaopeng Jiang, Eric Croiset, Zhengyu Bai, and Lin Yang,). Reproduced with permission from "Orbital Interaction in Bi-Sn Bimetallic Electrocatalyst for Highly Efficient CO_2 Reduction" ***Adv. Energy Mater*.** **2018**, 8, 1802427." Copyright 2018 2018 WILEY-VCH Verlag GmbH & Co. KGaA, DOI: org/10.1002/aenm.201802427. *Featured on Cover.*

Chapter 4 of this thesis consists of the following paper that was co-authored by myself, my supervisors, four Ph.D. students (Bohua Ren, Haozhen Dou, Zhen Zhang, and Yaping Deng), and six collaborators (Moon G. Park, Jie Yang, Zhengyu Bai, Lin Yang, Gianluigi A. Botton, and Yongfeng Hu). Reproduced with permission from "Ternary Sn-Ti-O Electrocatalyst Boosts the Stability and Energy Efficiency of CO_2 Reduction", ***Angew. Chem. Int. Edit.*** **2020**, 59, 12860." Copyright 2020 Wiley-VCH Verlag GmbH & Co. KGaA. DOI: org/10.1002/anie.202004149. *Featured on Cover.*

Chapter 5 of this thesis is a part of a manuscript that was co-authored by myself, my supervisors, and other collaborators.

Abstract

The conversion of CO_2 to valuable chemicals via electrochemical CO_2 reduction reactions (CO_2RR) offers a clean approach for recycling CO_2 with sustainable and environmental benefits. Among a variety of derived chemicals, carbon monoxide (CO) and formic acid (HCOOH) are attracting attention on the basis that fewer electrons are needed and they have large potential markets (CO for synthetic gas and formic acid for hydrogen carrier). Nevertheless, CO_2RR is difficult and needs harsh reaction conditions due to CO_2 is thermodynamically stable. Up till now, the research of efficient materials is still at the early stage and far from the requirements of high activity, high selectivity, long stability, and low overpotential. Nonetheless, the prospect of an efficient electrolytic cell has drawn attention recently on account of scaling-up the CO_2RR process and integration with smart energy-grids.

This thesis composes of three works and starts with nanostructured catalysts investigations: **Chapters 3** focuses on CO_2-to-formate transformation, while **Chapter 4** digs into CO_2-to-CO transformation. Then **Chapter 5** proposes a new kind of flow cells for potential implementation into the economic continuous CO_2RR scaling-up process.

In the first work, a highly selective and durable electrocatalyst for CO_2-to-formate transformation is developed, consisting of tin (Sn) nanosheets decorated with bismuth (Bi) nanoparticles. Due to the formation of active sites through favorable orbital interactions at the Sn/Bi interfaces, the Bi-Sn bimetallic catalyst converts CO_2 to formate with a remarkably high Faradaic efficiency (96 %) and production rate (0.74 mmol h^{-1} cm^{-2}) at -1.1 V versus reversible hydrogen electrode (RHE). Additionally, the catalyst maintains its initial efficiency over an unprecedented 100 hours of operation. This study provides a general methodology for bimetallic catalyst developments and surface engineering design for highly selective CO_2 electroreduction.

In the second work, to further investigate the Sn-based materials with different decorations and for CO_2-to-CO conversion, a series of ternary Sn-Ti-O electrocatalysts were synthesized. Among these, 3D ordered mesoporous (3DOM) $Sn_{0.3}Ti_{0.7}O_2$ achieves a trade-off between active sites exposure and structural stability, demonstrating up to 71.5% half-cell EE over 200 hours and 94.5% Faradaic efficiency for CO at an overpotential as low as 430 mV. Density functional theory (DFT) and X-ray absorption fine structure (XAFS) analysis revealed an electron density reconfiguration in the Sn-Ti-O system. A downshift of the orbital band center of Sn and a charge depletion of Ti collectively facilitated the dissociative adsorption of desired intermediate COOH* for CO formation. It was also beneficial in maintaining a local alkaline environment to suppress H_2 and formate formation and in stabilizing oxygen atoms to prolong durability. These findings provide a new strategy of material design for efficient CO_2 conversion and beyond.

In the last work, a “Zero-gap” aqueous flow-through cell (AFT cell) was engineered for efficient continuous CO_2RR. Meanwhile, a one-dimensional (1D) diffusion/transport model and a 2D reaction/diffusion model were built respectively to quantify the boundary layer (BL) thicknesses and the species distribution around the electrode surface. AFT cell has the following advantages: (I) The neutral electrolyte flowed through the porous electrode, reducing the BL thickness to less than 2 μm with minimized mass transport resistance. (II) The wetted porous electrode was pressed onto the membrane ensuring the shortest possible ionic conduction pathways between the electrode−electrolyte interface; (III) Flowing electrolyte with carbon sources in the form of dissolved CO_2 and HCO_3^-, eliminating the degradation related to electrolyte flooding and carbonate precipitation. (IV) While using synthesized 3DOM $Sn_{0.3}Ti_{0.7}O_2$ electrode, AFT cell achieved production rate toward CO over 4.0 mL/min/cm^2 and partial current density for CO (J_{CO})

exceeding 300 $mA \cdot cm^{-2}$ at the cell overpotential around 1.0 V; ten times higher than the H-cell with the same condition of FE_{CO} (> 90%).

Acknowledgements

I would like to express my deepest gratitude and appreciation to my supervisors, Prof. ***Zhongwei Chen*** and Prof. ***Jeff Gostick***, for their convincing guidance, motivation, and helpful advice during my Ph.D. study. I would never have accomplished so much without their great support. I would also like to extend my appreciation and thanks to my Ph.D. exam committee members for their valuable comments.

Special thanks to Prof. ***Eric Croiset*** at the University of Waterloo, Prof. ***Jingxu (Jesse) Zhu*** at Western University, and Prof. ***Yuanyuan Shao*** at Tianjin University (China) for giving me the opportunity of participating in this collaboration program to earn my Ph.D. degree at the University of Waterloo. I appreciate my former supervisors during my master's study, Prof. ***Yongli Sun*** and Prof. ***Lvhong Zhang*** at Tianjin University for their encouragement and support.

Thanks to all of my labmates and colleagues in Waterloo for their timely and generous help and useful suggestions, especially to Dr. Dong Un Lee, Dr. Fathy M. Hassan, Dr. Zhengyu Bai, Dr. Gaopeng Jiang, Dr. Haozhen Dou, Dr. Moon G. Park, Dr. Zachary P. Cano, Luo Dan, Yaping Deng, Zhen Zhang, and Yong Wook Kim. Thanks to my wife Bohua Ren, giving me strong support on both my research and life. Also, to all my friends, thanks a lot for your encouragement.

Without their persistent and kindly assistance, the goal of this project would not have been realized.

Dedication

I dedicate this dissertation to my beloved wife *Bohua Ren* for always being by my side; to my parents *Shenghui Wen*, *Yudun Zhan,* and parents-in-law *Demin Ren*, *Fenge Zhang* for their unconditional love and encouragement for me to overcome challenges in the past years.

Table of Contents

List of Figures

List of Tables

List of Abbreviations

3DOM	3D ordered mesoporous
AFT	Aqueous flow-through
BET	Brunauer-Emmett-Teller
Bi	Bismuth
BL	Boundary layer
CCS	Carbon capture & storage
CCU	Carbon capture & utilization
CD	Current density
CF	Carbon fibers
CO_2RR	Electrochemical CO_2 reduction reaction at room temperature
CPE	Constant potential electrolysis
DFT	Density functional theory
EDX	Energy dispersive X-Ray
EE	Energy efficiency
FE	Faradaic efficiency
GC	Gas chromatography
GDE	Gas diffusion electrode
GDL	Proton exchange membrane
HER	Hydrogen evolution reaction
LSV	Linear sweep voltammetry
NMR	Nuclear magnetic resonance

NP	Nanoparticles
PCD	Partial current density
PEM	Proton exchange membrane
RHE	Reversible hydrogen electrode
SCE	Saturated calomel electrode
SEM	Scanning electron microscopy
Sn	Tin
SOEC	Solid oxide electrolytic cells
TEM	Transmission electron microscopy
Ti	Titanium
TPB	Triple-phase boundary
XAFS	X-ray absorption fine structure spectroscopy
XPS	X-Ray photoelectron spectroscopy
XRD	X-Ray diffraction

Chapter 1. Introduction and Motivation

1.1. Background

Carbon dioxide (CO_2) is constantly accumulating in the atmosphere, which is mainly released through human activities such as deforestation, land-use changes, and excessive utilization of coal and petroleum as the main energy sources.[1-12] The increase of atmospheric CO_2 concentration, from 280 ppm (parts per million by volume) in 1750 to 410 ppm now,[13-14] raises lots of associated problems, such as global mean temperature rise, global average sea-level rise, and earth's polar ice sheets mass loss. A serious impetus exists to capture and utilize this kind of greenhouse gas.[15] In the meantime, global population, and subsequently the global energy demand, is projected to continue increasing, calling for a worldwide debate about carbon-neutral technology and energy sustainability.[16-21] Our reliance on fossil fuels needs to be reduced by turning to renewable energy.[22] While solar and wind renewable energy sources already enjoys an important and impressively increasing role in the global energy mix, storage is still an issue due to intrinsic intermittency.[23] The residual electricity from these intermittent sources can be used to transform CO_2 to valuable fuels and chemicals, acting as one class of energy storage.

Owing to its linear and centrosymmetric molecular structure, CO_2 is thermodynamically stable and can only be converted into other carbon compounds under harsh reaction conditions, such as high pressure, high temperature, or high overpotentials.[24] Hitherto, several routes have been developed to convert CO_2 into other carbon compounds, these methods include thermocatalytic hydrogenation,[25-26] photochemical conversion,[27] biological conversion[28], electrochemical voncersion[6-7], etc. Among these, the conversion of CO_2 into fuels and chemicals using renewable electricity is one promising method, which has many advantages including but not limited: Utilize and convert CO_2; Store surplus intermittent renewable energies; Produce chemicals for long term storages or further factory usages; Control reaction rates/selectivity through the applied voltages; Wide scalability of the process due to modular electrolytic cells.[15]

The electrochemical CO_2 transformation can take place over a wide range of temperatures, from room temperature to over 1000 ℃.[29] For example, solid oxide electrolytic cells (SOEC) reduce CO_2 to CO efficiently at high current densities,[30-31] however, SOEC requires high operating temperatures of 750−900 °C and has limited product distribution.[32] The room temperature electrochemical CO_2 reduction reaction (CO_2RR) is considered as a promising strategy for sequestering CO_2.[33-34] This can be performed efficiently by coupling with renewable but intermittent sources of energies to form a sustainable recycling system and to create a global-scale sustainable carbon-neutral economy (**Figure 1-1**),[32, 35] allowing innovative carbon capture & utilization (CCU) instead of carbon capture & storage (CCS).[36-38]

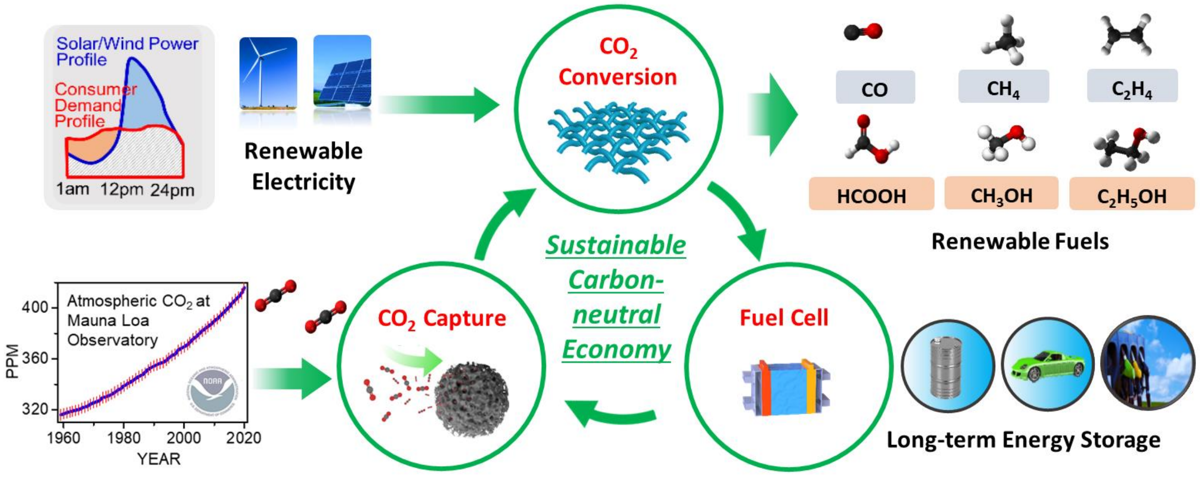

Figure 1-1. Schematic of the sustainable carbon-neutral economy composed of CO_2 capture, electrocatalytic CO_2 conversion, and fuel cells.

1.2. Challenges and Opportunities

1.2.1. Challenges

CO_2 has a linear and centrosymmetric molecular structure, consisting of a carbon atom covalently double bonded to two oxygen atoms with equivalent bonds (ca. 116.3 pm), which is 0.04 Å smaller than the C=O bond in ketone structures.[39] It must be noted that CO_2RR is a lot more complicated than water splitting, as many various products can be produced via proton-coupled and multi-electron transfer steps, including but not limited to carbon monoxide (CO), formate ($HCOO^-$) or formic acid (HCOOH), methane (CH_4), methanol (CH_3OH), ethylene (C_2H_4), ethanol (C_2H_5OH), etc.[40-42]

To develop the CO_2RR process with economical attractivity and practical possibilities, it is important to produce (i) any product as selectively as possible (Faradatic efficiency > 90 %); (ii) products with economic value; (iii) products that are easy to separate.[29] Although some hydrocarbons or alcohols, such as methane and methanol (**Table 1-1**), have been of primary interest, they are plagued by the fact of low selectivity and extensive energy input.[43-45]

Table 1-1. Theoretical equilibrium potentials of CO_2RR.

Half reactions of CO_2RR		Equilibrium potential (V) vs. RHE[46]	Major metallic catalysts
$CO_2 + H_2O + 2e^-$	$\rightarrow CO + 2OH^-$	-0.10	Au, Ag, Zn, Pd, Ga
$CO_2 + H_2O + 2e^-$	$\rightarrow HCOO^- + OH^-$	-0.03	Pb, Hg, In, Sn, Bi, Pd
$CO_2 + 5H_2O + 6e^-$	$\rightarrow CH_3OH + 6OH^-$	0.03	Cu
$CO_2 + 6H_2O + 8e^-$	$\rightarrow CH_4 + 8OH^-$	0.17	Cu
$CO_2 + 8H_2O + 12e^-$	$\rightarrow C_2H_4 + 12OH^-$	0.08	Cu
The half reaction of HER			
$2H_2O + 2e^-$	$\rightarrow 2H_2 + 2OH^-$	0.0	Pt, Ti, Fe, Ni

In the first stage of the investigation, researchers studied the CO_2RR on various types of single metallic foils with a focus on tuning the reaction conditions, such as the temperature, CO_2 concentration, and the types of electrolytes. Up till now, with the emergence of nanotechnology and the rapid development of advanced characterization techniques, a good deal of nanostructured materials to efficiently improve the performance of CO_2RR have been synthesized and reported. The key research area in this field has shifted towards finding nanostructured materials and the understanding of structure–performance relationships. With tuning the structural combinations (ensemble and segregated mixing,[47-48] core-shells,[49-50] ordering patterns[51]), surface modifications,[52-54] controlled surface coordination number (CN),[55] defect sites,[56] morphology,[45, 57] and size,[58] the nanostructured materials show different selectivity and activity. Through appropriate engineering, the performances of many types of catalysts, such as metals,[59] metal oxides,[60] carbon materials,[34] and molecular compounds[61-63] have been greatly improved for CO_2RR. Additionally, the adsorption configuration and bonding strength, which further transform reaction routes, result in distinct product distributions.[64-65] Even up till now, the research of efficient materials is still at the earlier stage and far from the requirements of high activity, high selectivity, long stability, and low overpotential. Meanwhile, the efficient electrolytic cell also draws attention recently due to the requirements of scaling-up the CO_2RR process and integration with smart renewable energy-grids.

1.2.2. Objective I

One interesting target product from CO_2RR is formate, which is a stable and non-toxic liquid and has large market potentials in various applications including hydrogen carrier systems[14, 66-67] and formic acid fuel cells.[68-69] Besides, it has a high normalized market price (16.1×10^{-3} \$·electron^{-1} in **Table 1-2**).[15] However, improvements in selectivity and activity with long operating times are still the challenges. The design of catalysts is a critical step to solve these challenges and achieve feasible CO_2-to-formate transformation.

In brief, sp post-transition metals such as In[1, 70], Pb[1], Bi[71-73], and Sn[58, 74-75] produce mostly formate during CO_2RR. Unfortunately, most of these suffered from low Faradaic efficiency (FE) and poor partial current density due to the competitive hydrogen evolution reaction (HER).[65, 76]

Recently, combining more than one element in the form of binary or multi-component catalysts has shown to be an effective approach to tune the selectivity of CO_2RR catalysts.[44, 77-78] However, the research on the interaction between non-precious metals is limited, such as Bi and Sn. Accordingly, the first objective of the thesis is to promote the selectivity and activity of the catalyst toward formate along with long operating time through bimetallic interaction between non-precious Bi and Sn metals.

Table 1-2. Market price and annual global production of major CO_2RR products.[15]

Product	Number of required electrons	Market price ($/kg)	Normalized price ($/electron) × 10^3	Annual global production (Mtonne)
Carbon monoxide (Syngas)	2	0.06	0.8	150.0
Carbon monoxide	2	0.60	8.0	-
Formic acid	2	0.70	16.1	0.6
Methanol	6	0.60	3.1	110.0
Methane	8	0.18	0.4	250.0
Ethylene	12	1.30	3.0	140.0

1.2.3. Objective II

One of the major challenges for renewably powered electrosynthesis to displace petrochemical processes is higher energy efficiency (EE).[79] EE defines the overall energy utilization toward the desired product. Nevertheless, EE of CO_2RR is typically limited by a low selectivity of the desired product and a large overpotential (> 0.8 V).[80]

On the other hand, Sn-based materials (SnO_x) are able to convert CO_2 to both CO and formic acid and the mechanism behind this is still unclear .[2, 49, 75, 81] Noticeably, oxygen (O) atoms in SnO_x play an important role in the adsorption of intermediates.[82-83] However, the introduction of O atoms also causes catalysts to become unstable due to the competition between metallic oxide reduction and CO_2RR under highly cathodic conditions.[84] Adding other atoms into materials to stabilize the oxidation state of the surface-active atoms is also reported as an important and useful route, e.g., copper (I) nitride (Cu_3N) could be used as Cu^+ support during CO_2RR, which affects the electronic structure and oxidation state of the surface Cu, decreasing the energy barrier associated with CO dimerization during CO_2RR.[85]

Therefore, I proposed to decorate Sn with titanium (Ti) to overcome the following limitations of CO_2RR, i.e. stabilizing O atoms, lowering the overpotential, increasing the energy efficiency, and extending the stability of Sn-based.

1.2.4. Objective III

CO_2RR is often studied in an “H-cell” that is composed of planar electrodes immersed in an aqueous electrolyte. H-cell has severely limited mass transport across the electrolyte and thick hydrodynamic boundary layer (BL).[6, 86] The reaction takes place at the electrode/electrolyte interfaces. The local CO_2 concentration close to the active surface is related to the formation of intermediates, which could have a significant effect on product formation,[6, 45] e.g. the reaction suffers from slow kinetics owing to the low local concentration of CO_2 surrounding typical reaction catalysts.[87]

Besides, this field also focuses on the development of practical CO_2 electrolytic cells.[88] Lots of reactors are proposed and tested, e.g. H-cell, Modified gas diffusion electrode (GDE) cell, Polymer electrolyte membrane (PEM) based cell, etc. However, the performance of these cells is still far away from the requirements of the economic CO_2RR process.

In this work, an aqueous flow-through (AFT) cell for continuous CO_2RR was proposed and had plenty of advantages, and compared it with the gas diffusion electrode (GDE) cell to further have a comprehensive understanding and shed a light onto the engineering of electrodes and electrolytic cells for CO_2RR.

1.3. Structure of Thesis

The three objectives of the proposed research are as follows:

1) Promote the selectivity and activity of CO_2-to-formate conversion, along with long operating time through the investigation of bimetallic catalysts, i.e. Bi and Sn;
2) Increase the energy efficiency, lower the overpotential, and extend the stability of Sn-based materials for CO_2-to-CO transformation by doping Ti;
3) Optimize electrolytic cells through a combination of experiments and simulations to achieve highly efficient continuous CO_2RR with higher current densities and lower cell overpotentials.

This thesis is organized into six chapters. **Chapter 1** introduces a general background, motivation, and the scope of the thesis. **Chapter 2** presents a literature review of the current status of materials syntheses, characterization techniques, and electrolytic cells used for CO_2RR. Three different tasks are presented to achieving objectives discussed above in subsequent chapters 3-5. **Chapter 3** focuses on a Bi-Sn bimetallic catalyst, aiming to CO_2-to-formate transformation with high activity, high selectivity, and long stability. **Chapter 4** further investigates the Sn-based materials with Ti decoration in order to achieve a low overpotential, high energy efficiency, and robust stability for CO_2-to-CO conversion. **Chapter 5** describes a new aqueous flow-through cell for continuous CO_2RR with a range of advantages and compares it with the GDE cell through a combination of experiments and simulations to have a comprehensive understanding of the engineering of electrodes and electrolytic cells for CO_2RR. **Chapter 6** summarizes the important results from this thesis and some discussions on the future directions and outlooks.

Chapter 2. Literature Review

2.1. Fundamentals and Metrics

2.1.1. Fundamentals of CO_2RR

The key parameters to evaluate the CO_2RR performance of materials are the current density, Faradaic efficiency (FE), overpotential, Energy efficiency (EE), and stability. It’s important to notice that these parameters are not only dependent on the materials itself, but also rely on the type of electrolyte,[89] system temperature, the hydrodynamics of the electrochemical cell, the purity of both the electrocatalyst and the electrolyte, and etc.[90-91]

In general, most materials’ performance was reported and tested by the H-type cell in 0.5 M or 0.1 M $KHCO_3$ or $NaHCO_3$ electrolyte at room temperature, while the oxygen evolution reaction (OER) takes place at the opposite anode side (**Figure 2-1a**). Linear sweep voltammetry (LSV) tests are performed to initially evaluate the CO_2RR performance of the prepared electrodes under N_2-bubbling and CO_2-bubbling electrolytes, respectively (**Figure 2-1b**). A series of constant potential electrolysis (CPE) measurements are followed to investigate the potential dependence of the materials’ performance. In order to obtain the selectivity of different products, the products in the gas phase are injected into gas chromatography (GC) to perform quantification during CPE measurements. Liquid products are dissolved in the electrolyte and quantified through a Nuclear magnetic resonance (NMR) spectrometer after the CO_2RR.

2.1.2. Onset Potential

The onset potential refers to the applied voltage on the electrocatalyst vs. the reference electrode, under which the desired product is yielded at a detectable amount. The onset potential is always lower than the standard reduction potentials due to the kinetic energy barrier. The difference between the onset potential and the standard reduction potential is defined as the onset overpotential. The onset potential could directly show the minimum overpotential for the CO_2RR toward the products.[92] Generally, the onset potential can be defined as the potential at which the current density was 0.2 mA·cm^{-2} higher than the initially stabilized current density.[93]

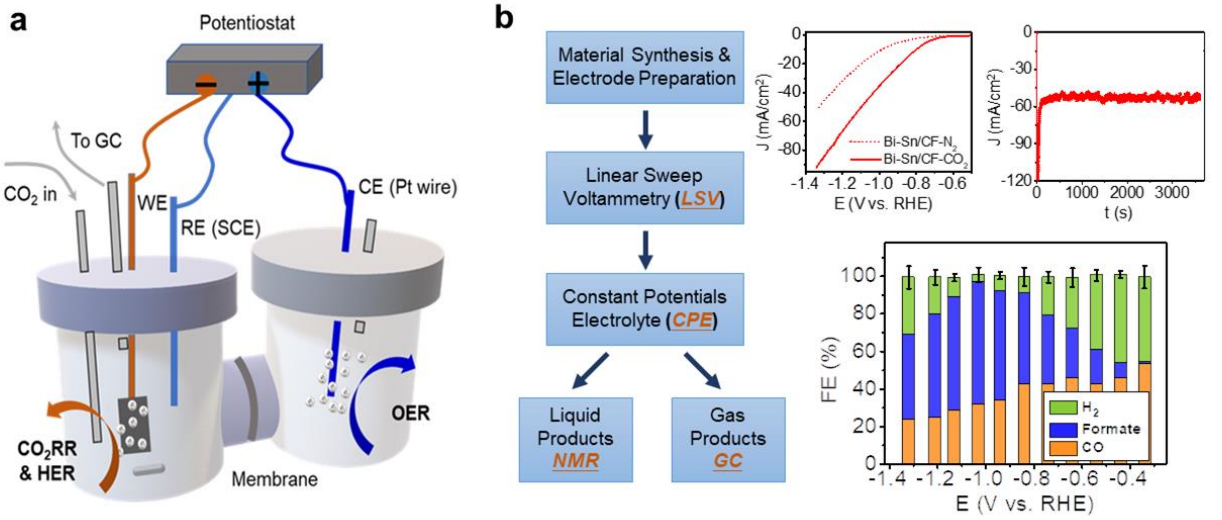

Figure 2-1. (a) Classic H-cell.[86] (b) Typical laboratory CO_2RR testing process and corresponding LSV, CPE and FE figures.[86]

2.1.3. Faradaic Efficiency

The Faradaic efficiency (FE) is defined as the percentage of the total charge supplied that is used to produce the desired product, which can also be seen as the yield based on the electrical charge passed during the electrolysis.[36] FE is directly related to the product selectivity, calculated using the following equation:

$$\mathrm{FE} = \frac{z \cdot n \cdot F}{Q},$$

where z is the number of electrons exchanged (z = 2 for reduction of CO_2 to CO or formate), n is the number of moles for a specific product, F is Faraday's constant, Q is the total charge passed (C).

2.1.4. Current Density

The current density (CD) is typically normalized over the surface area or the mass of the working electrodes. This parameter is a crucial indicator of the activity of the materials or the cells. The overall current density has an important relationship with the transformation rate. As a measure of the reaction rate, this parameter is crucial for practical applications, since it determines the electrolytic cell size and the cost needed for the process.

The partial current density (PCD) toward a specific product can be acquired through multiplying the corresponding FE by the CD.[24]

2.1.5. Overpotential

CO_2RR requires a significant overpotential to drive it at an economically viable rate. The electrocatalyst is often employed to reduce the overpotential for CO_2RR. Generally, the difference between the applied cathode potential and the standard reduction potential is defined as the cathodic overpotential.[24] While the cell overpotential also can be simply defined as the difference between operation voltages and onset cell potentials, which contains the result of activation polarization ($\eta_{\text{activation}}$) to overcome the activation energy barrier for reactions on the catalytic electrode surface and the mass transfer limitation of dissolved CO_2 ($\eta_{\text{diffusion}}$).[94] Meanwhile, to simplify the calculations, the ohmic drop (iR_S) across the electrolyte and ion exchange membrane is also considered as part of the overpotential although there are existing rigorous calculations.[80, 9495]

2.1.6. Energetic Efficiency

Energy efficiency (EE) is a crucial parameter, and increasing EE is one of the major challenges for renewable electricity-powered electrosynthesis to displace petrochemical processes.[79, 96] Considering FE and overpotential, the EE can be derived across the whole cell to indicate the conversion of applied energy toward chemically stored energy.[94]

$$\mathrm{EE} = \frac{E^0 \ \cdot \ \mathrm{FE}}{E^0 + \ \eta},$$

where E^0 is the thermodynamic reaction voltage; η is the total cell overpotential. Generally, half-cell EE or cathodic energy efficiency ($\mathrm{EE_{ca}}$) for CO_2RR in H-cell was calculated using the following equation.[80, 97]

$$\mathrm{EE_{ca}} = \frac{E_{\mathrm{eq,cell}} \ \cdot \ \mathrm{FE}}{E_{\mathrm{eq,cell}} + \ \eta_{\mathrm{cathode}}},$$

where $E_{\mathrm{eq,cell}}$ is the thermodynamic equilibrium potential between anode and cathode reactions, which is $E_{\mathrm{eq,cell}} = 1.23 + \left(-E_{\mathrm{eq}}\right)$ (1.23 V is the thermodynamic equilibrium potential for anode oxygen evolution reaction); E_{eq} is the thermodynamic equilibrium potential for cathode reaction (vs. RHE). $E_{\mathrm{eq,CO}} = \ -0.109$ V, $E_{\mathrm{eq,formate}} = \ -0.03$ V; η_{cathode} is the cathode overpotential, which is the applied cathode potential (vs. RHE) minus the thermodynamic equilibrium potential.

2.1.7. Tafel Slope

The Tafel slope is a plot slope of overpotential vs. the logarithm of the partial current density. The number is an indicator of the reaction path and the rate-determining step. In general, a smaller Tafel slope indicates better catalytic performance. In the case of CO_2RR, Tafel slope of 116 $\mathrm{mV \cdot dec^{-1}}$ implies that the rate-determining step for CO_2 reduction is the generation of the intermediate by the initial one-electron transfer step, while the slope of 59 $\mathrm{mV \cdot dec^{-1}}$ is indicative of a one-electron pre-equilibrium step before a later rate-limiting chemical step, which is commonly invoked for metal electrodes.[24]

2.1.8. Stability

The stability of the catalysts is crucial with respect to industrializing the electrolytic cell.[94] This metric can be measured at a specific constant potential under chrono-potentiometric tests, where the current is fixed at a proper level and the resulting potential over the half-cell or full cell is recorded.

2.2. Current Status of Electrocatalysts

2.2.1. CO_2-to-formate conversion

Sp post-transition metals such as In,[1, 70] Pb,[1] Bi,[71-73] and Sn[74-75] produce mostly formate during CO_2RR. However, most of these catalysts suffered from low FE, poor PCD,[65, 76] and high overpotentials with the high energy cost. The applied high voltages would also accelerate the HER, which is the competing reaction and reduces the selectivity of formate. The following sub-sections describe the up-to-date catalysts in the production of formate.

Tin

Tin (Sn), among the post-transition-metal block, is a promising electrocatalyst[36, 75, 98-101] because it showed high selectivity towards the conversion of CO_2 to formate. Additionally, Sn is one of Earth’s abundant elements, which is also non-toxic, which reinforces its potential applicability to energy-grid integration.[98, 102-105] Metallic Sn quantum sheets confined in graphene[75] with a higher electrochemical active area confers 9 times larger CO_2 adsorption capacity relative to the bulk Sn foils. The lowered Sn–Sn coordination numbers, revealed by X-ray absorption fine structure spectroscopy (XAFS), enable tin quantum sheets confined in graphene to efficiently stabilize the carbon dioxide radical anion. Hence, as **Figure 2-2** reveals, the tin quantum sheets confined in graphene show enhanced electrocatalytic activity and stability.

Another strategy is to design nanosheet structures with numerous coordinatively unsaturated sites.[73] The mesoporous SnO_2 nanosheets[106] on carbon cloth exhibited a high partial geometry current density of 45 mA·cm^{-2} when FE is around 87% toward formate. On the other hand, binary or multi-component metallic catalysts with unique nano-scale structures, such as alloy[76], core-shell structure[49-50], and linked monometallic nanoparticles[44, 77-78], show great advantages toward CO_2RR. For example, Pd-Sn nanoparticles[76] was reported with nearly 100% selectivity toward formate. From the Density functional theory (DFT) calculations, the Pd-Sn alloy catalyst surface leads to a more energetically favorable formation of the key reaction intermediate HCOO* as well as the product formic acid.

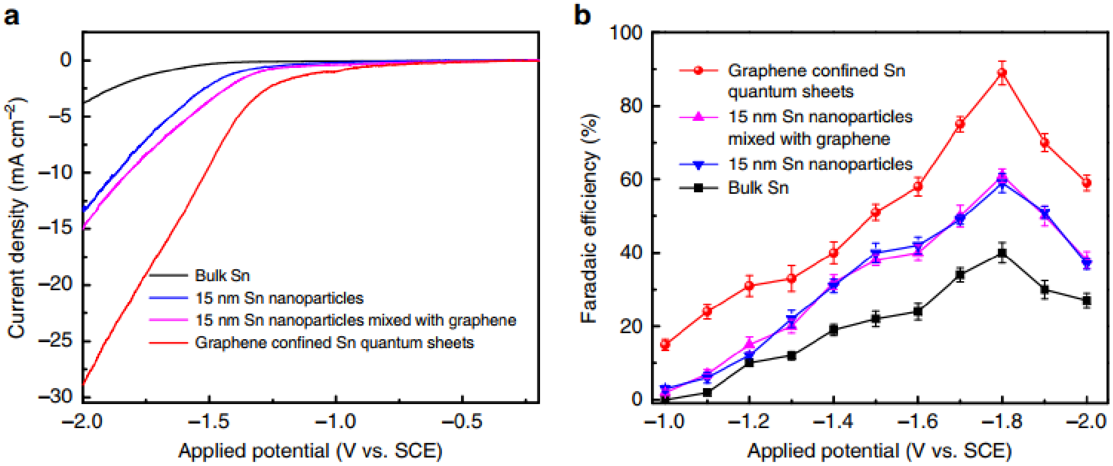

Figure 2-2. CO_2RR performances of Sn quantum sheets confined in graphene.[75] (a) LSV curves in the CO_2-saturated 0.1 M $NaHCO_3$ aqueous solution, (b) FE for formate at each applied potentials.

Bismuth

Due to the advantages of low cost and low toxicity, Bi has received attention as a promising candidate for CO_2RR as well. In reported studies, the Bi catalysts could convert CO_2 to CO with high FE of 74−96% in an aprotic electrolyte (e.g. acetonitrile) containing ionic liquids.[107-110]

However, in an aqueous electrolyte, Bi-based electrodes could selectively reduce CO_2 to formate, which is also the focus and a more practical catalytic environment in terms of cost-effectiveness than an aprotic electrolyte with an ionic liquid (**Table 2-1**).[72]

Table 2-1. CO_2RR properties of electrocatalysts for formate production.

Electrocatalysts		Electrolyte	Potential (V_{RHE})	FE for formate	Ref.
Sn	Sn/SnO_x thin film	0.5 M $NaHCO_3$	-0.70	40%	32
	SnO_x/graphene	0.1 M $NaHCO_3$	-1.16	94%	58
	Electroplated Sn/Cu foam	0.1 M $KHCO_3$	-1.19	84%	111
	Electroplated Sn/gas diffusion electrode	0.5 M $NaHCO_3$	-1.10	71%	112
	Electrodeposited Sn powder	0.5 M $KHCO_3$	-1.5	74%	113
	Electrodeposited Sn dendrite	0.1 M $KHCO_3$	-1.3	83%	114
	Nanoporous Sn foam	0.1 M $NaHCO_3$	-1.4	90%	115
	Etched Sn foil	0.1 M $KHCO_3$	-1.7	85%	116
	Sn nanoparticles	0.45 M $KHCO_3$	-1.5	70%	117
	Sn-Pb alloy	0.5 M $KHCO_3$	-1.4	80%	118
	Graphene/Sn/Graphene	0.1 M $NaHCO_3$	-1.8	89%	75
	Ag_3Sn nanoparticles	0.5 M $NaHCO_3$	-0.9	87%	50
Bi	Bi nanodendrite / Carbon paper	0.5 M $NaHCO_3$	-1.56	96%	72
	Bi nanoparticle/Cu foil	0.1 M $KHCO_3$	-1.46	95%	119
	Bi flake	0.1 M $KHCO_3$	-0.6	99%	71
In	Anodized In	0.5 M $KHCO_3$	-1.5	79%	120
Co	Partially oxidized Co nanoparticles	0.1 M Na_2SO_4	-0.2	45%	7
Pb	Oxide-derived Pb	0.5 M $NaHCO_3$	-0.8	98%	121
	Roughened Pb	0.1 M $KHCO_3$	-1.0	89%	122

Pd	Pd-Pt nanoparticle	0.1 M KH_2PO_4	-0.4	88%	[123]
	Electrodeposited Pd nanoparticles	0.1 M $KHCO_3$	-0.4	55%	[124]
	Pd nanoneedle	0.5 M $KHCO_3$	-0.2	91%	[6]
	Pd nanoparticle/ Carbon	0.5 M $NaHCO_3$	-0.25	94%	[125]

As reported, Bi nanoflakes were successfully grown on Cu foil through a pulse electrodeposition method.[71] Due to a larger number of edge and corner sites than conventional Bi films deposited by the direct current method, Bi nanoflakes resulted in strong local electric fields as confirmed by numerical simulation.[71] The local K^+ concentration around the catalyst was increased by the local electric field, which further activated the reaction. Meanwhile, the electric field produced a driving force that facilitates charges to move from the electrode to the surface of the catalyst (**Figure 2-3**). Bismuth nanoflakes achieved a maximum FE for formate close to 100%. The higher FE depends on the edge and corner sites on these nanostructured electrodes. These sharp sites produce strong electric field-induced reagent concentration (FIRC) close to the active CO_2RR surface.[6, 71, 126]

The Bi dendrite electrode reduced the overpotential of CO_2-to-formate conversion by 180 mV:[72] an overpotential of 890 mV to reach its maximum FE of ~79% for formate was required by the pristine Bi foil, while only 710 mV was needed for the Bi dendrite to achieve its maximum FE of ~89% for formation. Using DFT calculations, three possible CO_2RR pathways were investigated, where the path involving the formation of HCOO* intermediate was the most favorable from the calculations of reaction free energies. This further indicated that the high-index planes can efficiently stabilize the HCOO* intermediate to enhance CO_2-to-formate activity, which can be used to explain the origin of the enhancement performance of Bi dendrite compared to Bi foil.

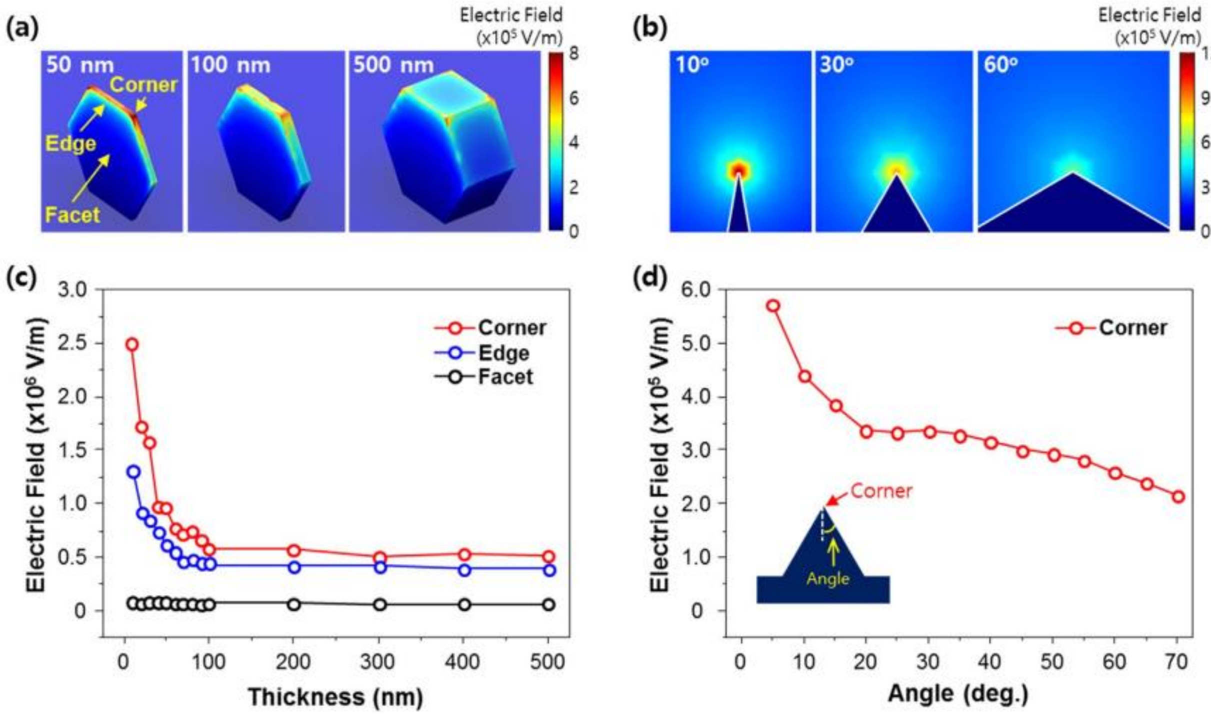

Figure 2-3. Simulated electric field distribution in (a) three-dimensional and (b) two-dimensional Bi nanostructures; strong electric field is formed as the shape is thinner and sharper. Electric field intensity plotted as a function of (c) thickness and (d) corner angle of Bi nanostructure.[126]

Other Catalysts

Ultra-thin Co-based Nanosheets

Ultra-thin Co-based nanosheets, which are only 4-atoms-thick, through a ligand-confined growth strategy were synthesized by Xie and co-workers (**Figure 2-4a, b**).[7, 127] Through controlling synthesis times of 3 h and 48 h, partially oxidized and pure Co two-dimensional nanosheets could be prepared, respectively. As shown from CO_2RR performance results (**Figure 2-4c**), the synthesized partially oxidized Co nanosheets exhibited the best activity compared to pure Co nanosheets and bulk Co under comparable conditions, and the overpotential was only 0.24 V. The partially oxidized 4-atom-thick Co nanosheets showed the highest FE for formate production of 90.1% at -0.85 V vs. the saturated calomel electrode (SCE) (**Figure 2-4d**). With abundant active sites and high electrical conductivity, the 4-atom-thick nanosheets were promising for substantially promoting of CO_2RR. This indicated that the correct morphology and oxidation state can transform material from one considered nearly non-catalytic for the CO_2RR into an active catalyst.

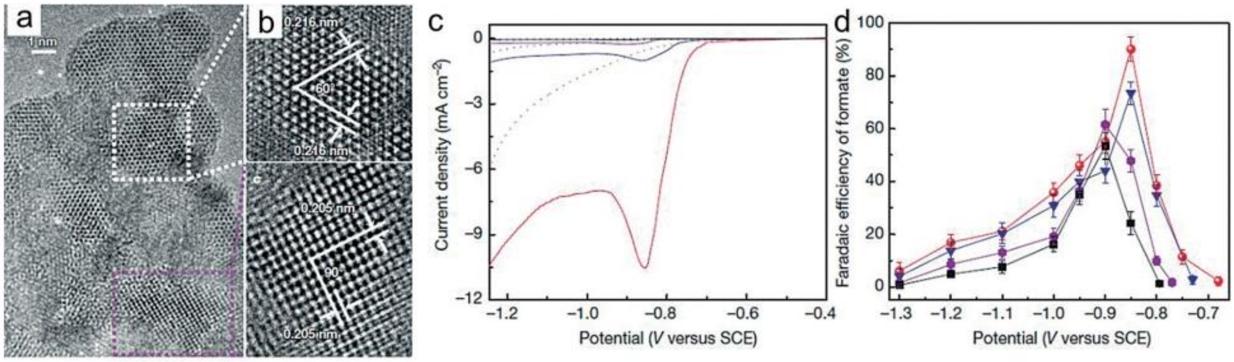

Figure 2-4. (a), (b) High-resolution TEM image. (c), (d) Linear sweep voltammograms curves in a CO_2-saturated (solid line) and N_2-saturated (dashed line) and the FE for formate on partially oxidized Co 4-atom-thick layers (red), Co 4-atom-thick layers (blue), partially oxidized bulk Co (violet), and bulk Co (black).[7]

Carbon-Based Electrodes

Carbon nanomaterial also attracts lots of research and is one kind of the most promising potential materials for CO_2RR and other new-energy related areas. It's considered as a replacement for expensive metals or metal oxides for electrocatalytic reactions.[24] For example, the N, S-co-doped mesoporous carbon nanosheets from graphene oxide polydopamine hybrids were synthesized and reported by Qiao et al., which showed great performances in both the oxygen reduction reaction (ORR) and the oxygen evolution reaction (OER).[128] In recent investigations, carbon nanomaterials were also found to effectively transform CO_2 to formate during CO_2RR,[129-130] e.g., Meyer et al. have selected nitrogen-doped carbon nanotubes as the catalyst for CO_2RR.[129] Noticeably, they were selective to CO_2-to-formate conversion and robust in aqueous electrolyte.

2.2.2. CO_2-to-CO conversion

Au has attracted a lot of attention because of the ability to convert CO_2 to CO selectively and efficiently, although the scarcity and high cost may hinder its further practical use.[6, 92, 131-132]

Meanwhile, Ag is also promising as a CO_2RR catalyst because of its relatively low overpotential and high selectivity.[133-135]

For the formation of CO, the reaction begins with the reductive adsorption of CO_2 on the catalyst surface leading to the formation of a *COOH intermediate, which is further explained in Section 2.4. The adsorbed *COOH intermediate is further reduced with the addition of extra proton and electron, forming CO and H_2O. Compared with the first two steps, which are electrochemical reactions and involving the transfer of an electron and a proton, the final step is the not-electrochemical and related to the release of CO from the electrode. Based on this reaction pathway, the promising materials should have a strong binding with *COOH intermediate and weak adsorption of CO in order to provide the facile conversion of *COOH into CO. Up till now, it has been found that materials with well-controlled size, surface structure, composition, and oxide-derived (OD) surfaces exhibited greatly enhanced performance for CO_2RR.[24]

The size of the particles (NPs) is crucial for the efficiency of CO_2RRR. Accordingly, nanoparticles with different sizes exhibit different performances in CO_2RR.[24] Noticeably, atoms at the corner or edge positions have a low coordination number and have higher surface energy. Based on this behavior we know, some materials we should avoid, and some materials may have synergic interaction, thus it will guide us in the synthesis of catalysts.

2.2.3. Strategies to Composite Nanostructured Materials

Binary or ternary catalysts have attracted extensive attention due to their tuneable chemical/physical properties. In changing from monometallic to binary or ternary metallic catalysts, an extra degree of freedom is introduced. Among a series of synergistic effects, the ensemble effect is crucial and has been identified and employed recently to alter the bonding strength of different intermediate for CO_2RR. C. Wang et al. reported a new strategy of design the ensemble size of active sites on Pd@Au bimetallic catalysts (**Figure 2-5a**) to enhance the efficiency of CO_2RR.[48] The study objectively combined the advantages of the two metals, and hypothesized that dispersion of strongly binding metal sites, such as Pd (Third case in **Figure 2-5b**), on the surface of a weak binding metal, e.g., Au (First case in **Figure 2-5b**) in order to simultaneously lower the energy barrier for CO_2 activation and mitigating *CO poisoning (Second case in **Figure 2-5b**). The element mapping based on HAADF-STEM (aberration-corrected high-angle annular dark-field scanning transmission electron microscopy) and EELS (electron energy loss spectroscopy) were used to follow the structural evolution at increasing Pd doses (**Figure 2-5c**). With the increasing of Pd atoms, continuous ensembles of Pd occur and form a semi-continuous layer. Ultimately, the Au NP became completely encapsulated in a Pd shell in the case of Pd_{20}@Au_{80}. Both the FE and partial current density (J_{CO}) toward CO exhibited a nonlinear behavior as the atomic ratio of Pd increases (**Figure 2-5d**). Among a series of Pd@Au NPs, when the ratio was 5:95, it showed the highest activity for the selective reduction of CO formation, with FE_{CO} and J_{CO} reaching ~80% and 1.6 mA/cm^2 at −0.5 V.

As shown in **Figure 2-5e**, the key role of ensemble effect played by the Ag/Cu interface in Ag/Cu nanoparticles (NP) was uncovered in promoting the performance of CO_2RR.[47] Nanodimers (ND) including the two constituent metals, which as segregated domains and shared a tunable interface, were obtained by developing a seeded growth synthesis. In this system, preformed Ag nanoparticles were used as nucleation seeds for the Cu domain. The type of metal precursor and the strength of the reducing agent act as a crucial role in achieving the desired chemical and structural control. Different ensemble structures, which lead to tandem catalysis and electronic effects, synergistically contributed to an enhancement in the FE for C_2H_4 by 3.4-fold and in the partial current density for CO_2RR by 2-fold compared with the pure Cu counterpart. The performance highly related to the ensemble structure was also unveiled through a range of bimetallic Cu−Pd catalysts with ordered/ disordered/ phase-separated atomic arrangements[136] and ordered/ disordered multi-metallic Au-Cu nanoparticles[51] (**Figure 2-5f** and **g**).

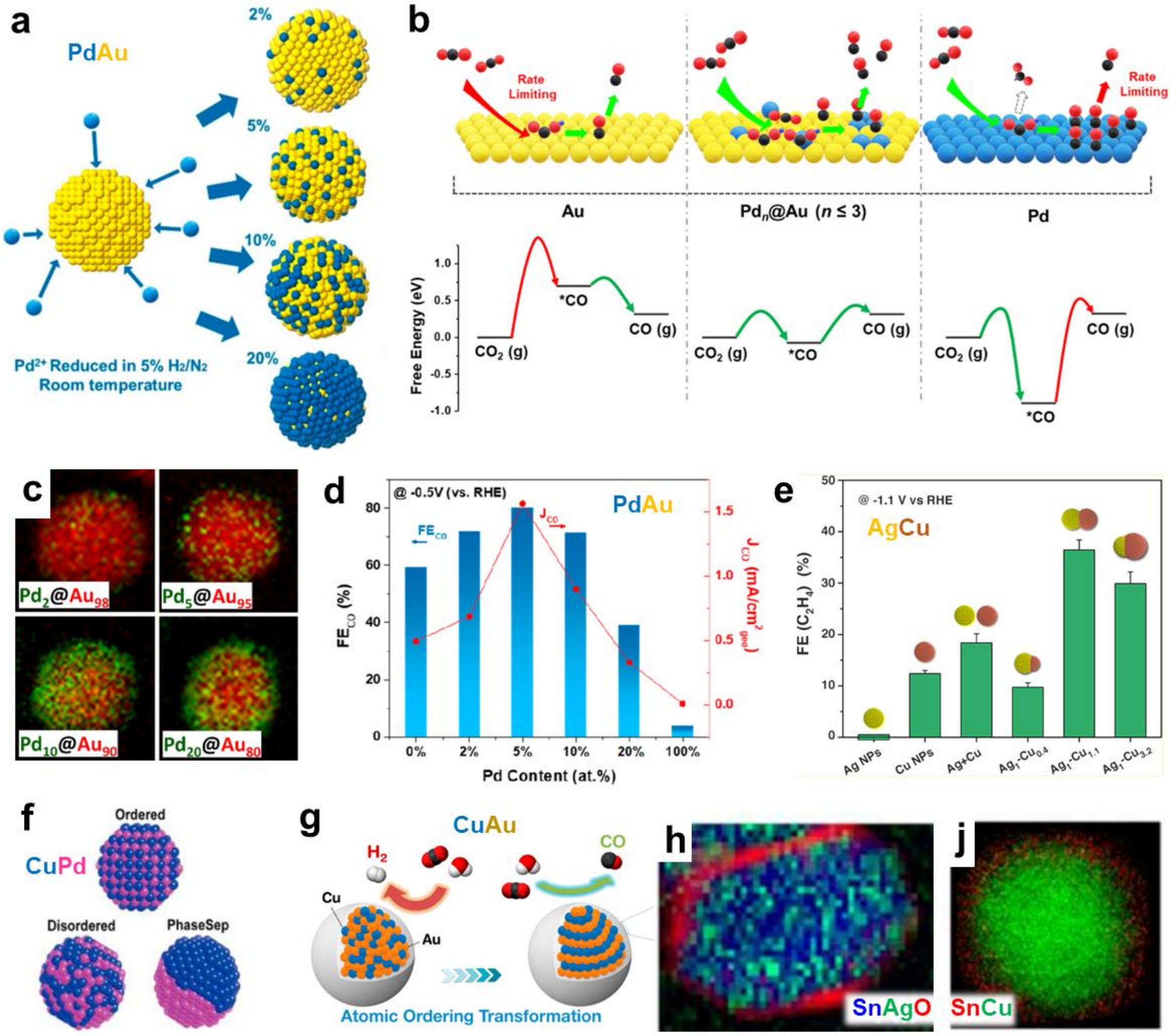

Figure 2-5. (a) Illustration of the synthetic scheme for the Pd@Au nanoparticles with control over the dose of Pd.[48] (b) Illustration of the concept using atomically dispersed Pd sites on the Au surface to enhance CO_2RR.[48] The yellow and blue spheres represent Au and Pd atoms, respectively. For the molecular structures, red, gray, and purple colors represent oxygen, carbon, and hydrogen, respectively. The red (vs. green) arrows represent the rate-limiting factors in the reaction kinetics. (c) EELS-based element maps for Pd_2@Au_{98}, Pd_5@Au_{95}, Pd_{10}@Au_{90}, and Pd_{20}@Au_{80}, where Au and Pd atoms are represented by red and green pixels, respectively.[48] (d) Dependences of FE_{CO} and J_{CO} at −0.5 V vs. RHE on the Pd content within the Pd@Au nanoparticles.[48] (e) FE for C_2H_4 obtained on different Ag/Cu nanocrystals, including Ag NPs, Cu NPs, Ag+Cu Mixture, Ag_1−$Cu_{0.4}$ NDs, Ag_1− $Cu_{1.1}$ NDs, and Ag_1−$Cu_{3.2}$ NDs at −1.1 V vs.

RHE.[47] (f) Illustration of prepared Cu-Pd nanoalloys with different atomic mixing patterns: ordered, disordered, and phase-separated.[136] (g) Atomic ordering transformation of Au-Cu bimetallic nanoparticles.[51] (h) EELS mapping of the selected region showing the elemental distribution of Sn (blue), Ag (green), and O (red).[50] (g) EELS elemental mapping of Cu (green) and Sn (red) of a 7/0.8 nm Cu/SnO_2 NP.[49]

Core−shell nanostructure as one of the important and earlier investigated engineering strategies to improve performance of CO_2RR might also be accounted for ensemble effects, such as Ag−Sn bimetallic electrocatalysts[50] and Cu-Sn bimetallic electrocatalysts[49] (**Figure 2-5h** and **j**). F. Jiao et al. showed the bimetallic core with an ultrathin partially oxidized shell, which achieved high electronic conductivity and efficient performance for CO_2RR. Otherwise, the reduction performance is Sn-thickness dependent when a thin layer of SnO_2 is coated over Cu NPs: the thicker (1.8 nm) shell shows Sn-like activity to produce formate whereas the thinner (0.8 nm) shell is selective to CO formation with FE_{CO} reaching 93% at −0.7 V. DFT calculations revealed that the 0.8 nm SnO_2 shell likely alloys with a trace of Cu, causing the SnO_2 lattice to be uniaxially compressed and favoring the production of CO over formate.

2.3. Electrode Structure and Reactor Design

Competing reactions (HER and undesired side reactions) and low reactant concentration around the surface of the catalyst are major obstacles preventing CO_2RR from widespread adoption.[87, 137] Especially at even higher currents, the CO_2 concentration at the electrode becomes quickly depleted due to the rapid consumption of CO_2 in the electrochemical reactions and unfavorable local pH conditions, further limiting the maximum current density of CO_2RR. These limits cannot be overcome only through CO_2 electro-kinetics on the electrode surface. Understanding the mass transport dynamics is essential due to the direct influence on observed catalyst performance.[87] Several electrochemical flow reactors or cells have been reported in the literature, such as aqueous electrolytic cells with the membrane,[138] solid oxide electrolysis cells,[139-140] and microfluidic electrolytic cells.[1, 141-142] Aqueous electrolytic cells with membrane are the focus of the thesis.

2.3.1. H-cell

Most reported CO_2RR were conducted using an H-type,[94, 99] also know as three-electrode cell, using the as-prepared electrode as the working electrode, Saturated Calomel Reference Electrode (SCE) as a reference electrode, and platinum wire as the counter electrode, respectively.[50, 75] The three electrodes were immersed an aqueous solution of 0.1 M or 0.5 M $KHCO_3$/ $NaHCO_3$ as the electrolytes. To avoid formic acid or other product oxidation by Pt counter electrode, a Nafion proton exchange membrane was adopted to separate the cathode and anode sides. The schematic of the H-cell is shown in **Figure 2-6**.

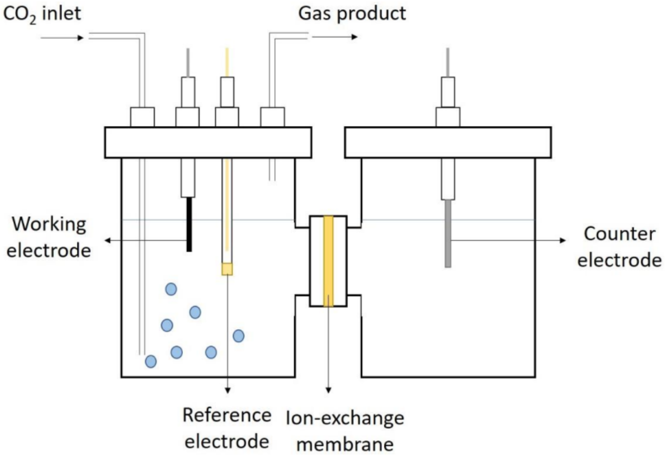

Figure 2-6. H-cell configuration for CO_2RR.[94]

2.3.2. Electrochemical Flow Cell

General Flow Cell

Jaramillo et al. reported an electrochemical flow cell for CO_2RR **(Figure 2-7a)**.[3, 143] The cell maintained the working electrode parallel to the counter electrode to achieve a uniform voltage. An anion exchange membrane was used to separate the CO_2RR and OER to prevent the oxidation of reduced CO_2 products. Although the membrane prohibits the passage of the anionic products acetate and formate, however, which still can be detected on the counter electrode side of the cell in low concentration after electrolysis. The cell was engineered to have a relatively large electrode area (1.5 cm × 3 cm) and a small electrolyte volume (8 mL) in each of the two compartments to increase the concentration of liquid products in the electrolyte. Electrolyte saturated with CO_2 flow through the chamber can obtain large current efficiencies for CO_2RR, presumably because of the existence of mass transport limitations in a quiescent cell.

PEM Based Flow Cell

Polymer electrolyte membrane (PEM) cells are widely used for hydrogen production by electrolysis. It is an advanced technology that uses the protons before recombination for CO_2 protonation. In this regard, CO_2 conversion using PEM cells at room temperature and ambient pressure had been extensively studied (**Figure 2-7b**). [144-146]

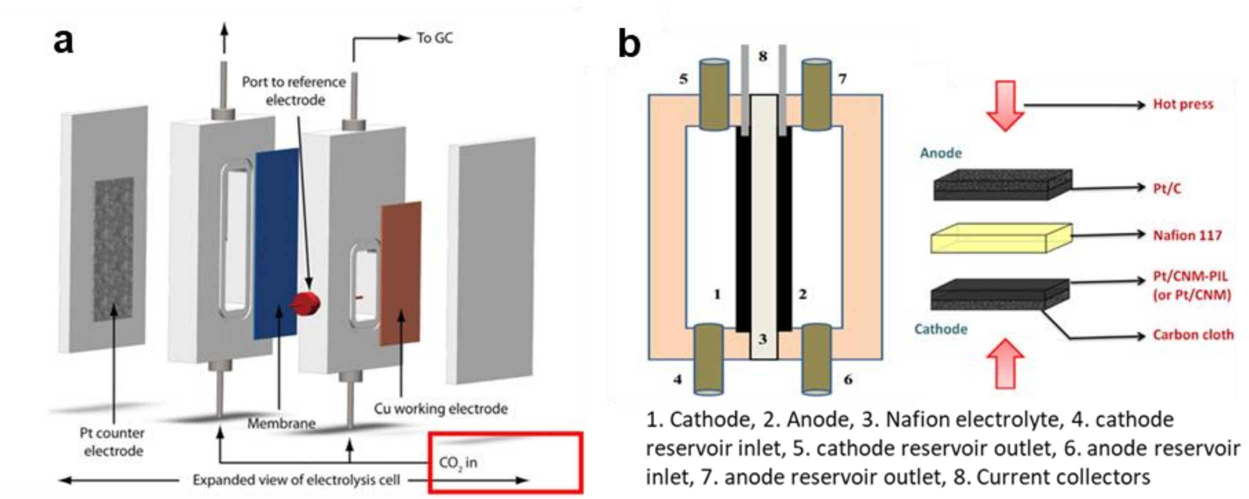

Figure 2-7. Schematic of (a) General electrochemical flow cell,[3] and (b) the PEM electrochemical cell and the membrane electrode assembly (MEA) fabrication.[144]

2.3.3. Gas Diffusion Electrode Cell

Alkaline GDE Cell

Kenis et al.[147] reported an electrochemical gas diffusion electrode (GDE) cell showing in (**Figure 2-8a**). An ionic exchange membrane was inserted between the cathode-side and anode-side chambers to prevent the re-oxidization of liquid products in case of diffusing to the anode. Stainless steel plates acted as current collectors and hold the flow cell together by a squeeze-action toggle plier clamp. The cathode current collector has a precisely machined 0.5×2.0 cm^2 window with 0.5-cm depth behind the GDE to allow for the transport of CO_2. The anode is open to the air, allowing oxygen to escape.

The application of GDE covered with active and rough Cu nanoparticles in the electrolytic cells results in a total FE (~46%) for ethylene and ethanol with CD of ~200 $mA \cdot cm^{-2}$ at a lower overpotential (< 0.7 V). The high production rates of ethylene and ethanol could be accounted for mainly for the use of alkaline electrolyte to improve kinetics and the inhibition of HER.

Filter-press GDE Cell

As seen in **Figure 2-8b**, a filter-press type electrochemical cell (Micro Flow Cell, Electrocell A/S)[36, 148] has three inlets (catholyte, anolyte, and CO_2) and two outlets (catholyte and anolyte). Catholyte is 0.5 M $NaHCO_3$, which pre-electrolyzed at -2 V under nitrogen bubbling to remove metal impurities. Anolyte (0.5 M NaOH) and catholyte were kept in two separate tanks and recirculated continuously into the cell by a dual peristaltic pump to accumulate liquid products. An ionic transport membrane (Nafionon® 117) divided the cell into two separate anodic and cathodic compartments.

PEM Based GDE Cell

A PEM based GDE cell was modified from conventional PEMFC configuration through inserting an additional buffer layer to circulate liquid phase electrolyte between the ion exchange membrane and Sn GDE,[29] as shown in **Figure 2-8c**. If without this buffer layer, H_2 was the predominant product with a faradaic efficiency of nearly ∼100%. With incorporating of this buffer layer to circulate the catholyte, substantially promoted the formation of formate and CO, while suppressing HER.

A gas diffusion layer (GDL) and a half catalyst-coated membrane (CCM) were hot-pressed together to serve as the anode. The half CCM was made by spraying Pt/C catalysts ink onto one side of a Nafion 212 membrane. The Sn-based cathode was made by spraying Sn catalyst ink onto the GDL. The thickness of the buffer layer was approximately 2.4 mm. The total volume of the electrolyte solution was 10 mL. The liquid products were accumulated in the electrolyte solution during electrolysis. This design demonstrates the feasibility to use current PEMFC hardware for CO_2RR.

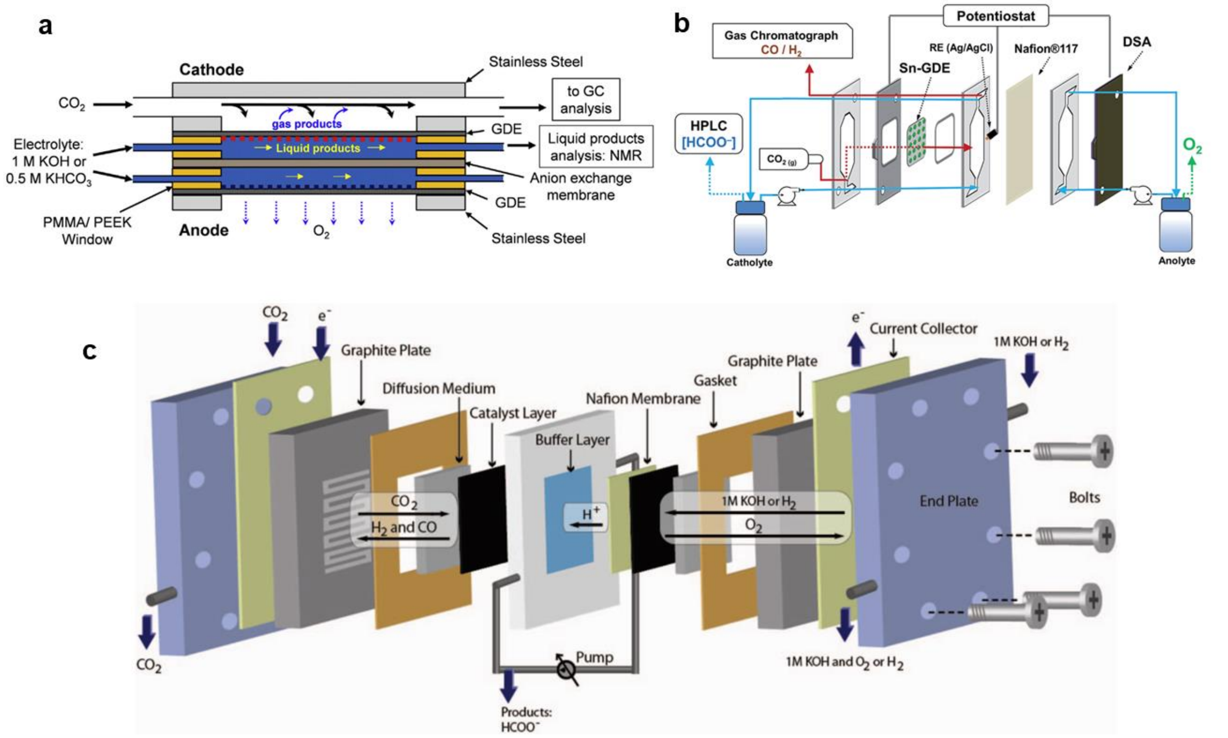

Figure 2-8. Schematic of (a) the electrochemical flow cell,[147] (b) the filter-press type electrochemical cell,[148] and (c) the full electrochemical cell featuring a buffer layer of circulating liquid-phase electrolyte.[29]

2.4. Reaction Mechanism and Pathways

The CO_2RR involves the interactions between the adsorbed CO_2 molecules, intermediates, electrons, and protons. The reaction pathways varied and may be affected by experimental parameters, such as CO_2 pressure, the cathodic potential, electrolyte salts, etc.[22, 149-150] With different proposed reaction mechanisms, or the combinations of different pathways, the CO_2RR leads to different product distributions. Among different catalysts, metallic catalysts show noticeable catalytic activities and selectivity[75] because of the different binding strengths of divergent intermediates and distinctive products. Generally, metal catalysts can be classified into three groups as displayed in **Figure 2-9a**. Group 1 metals produce formate or formic acid as the main product, in which including Sn, Hg, Pb, In, etc. Group 2, e.g. Au, Ag, Zn, Pd, etc, have relatively strong *COOH binding energies to facilitate further reduction. Nevertheless, the obtained *CO intermediate need to be weakly bound to these metal surfaces to desorb readily from the surface and emerges as a predominant CO formation. Furthermore, Cu is the most special one and is the only metal in group 3, which is able to bind and convert *CO intermediate to higher value-added products (such as hydrocarbons and alcohols) through *COH or *CHO intermediates. Additionally, HER as a competitive process in aqueous solutions during CO_2RR. Metals like Pt, Ti, Fe, and Ni have a good performance for HER, so the suppression of HER is important if the materials containing these compositions.

As shown in **Figure 2-9b**, oxide-derived Au supports a mechanism that involves a reversible e^- transfer to CO_2 to form adsorbed $CO_2^{\bullet -}$ followed by a rate-determining H^+ transfer with HCO_3^- serving as the H^+ donor. However, the first oxygen hydrogenation step is still under debate. A. Seifitokaldani et al. found that the hydronium (H_3O^+) intermediate plays a key role in the first oxygen hydrogenation step and lowers the activation energy barrier for CO formation by DFT calculations.[151] When this hydronium influence is removed, the activation energy barrier for oxygen hydrogenation increases significantly, and the barrier for carbon hydrogenation is reduced. Furthermore, J. Gong et al. pointed out moderating coverage of hydroxyl (-OH) on SnO_x deriving a stable Sn branches catalyst for CO_2RR with a 93.1% Faradaic efficiency (FE) of carbonaceous products.[84] Surface hydroxyls acted a crucial role in the activity and stability. To end this debate, in situ spectroscopies are the most powerful tools. Applications of different in situ spectroscopies, such as Infrared, Raman, X-ray absorption, X-ray photoelectron, and mass spectroscopies,[152] enable measurements of the system under real conditions and give us a comprehensive understanding of reaction mechanisms.[84, 152-153]

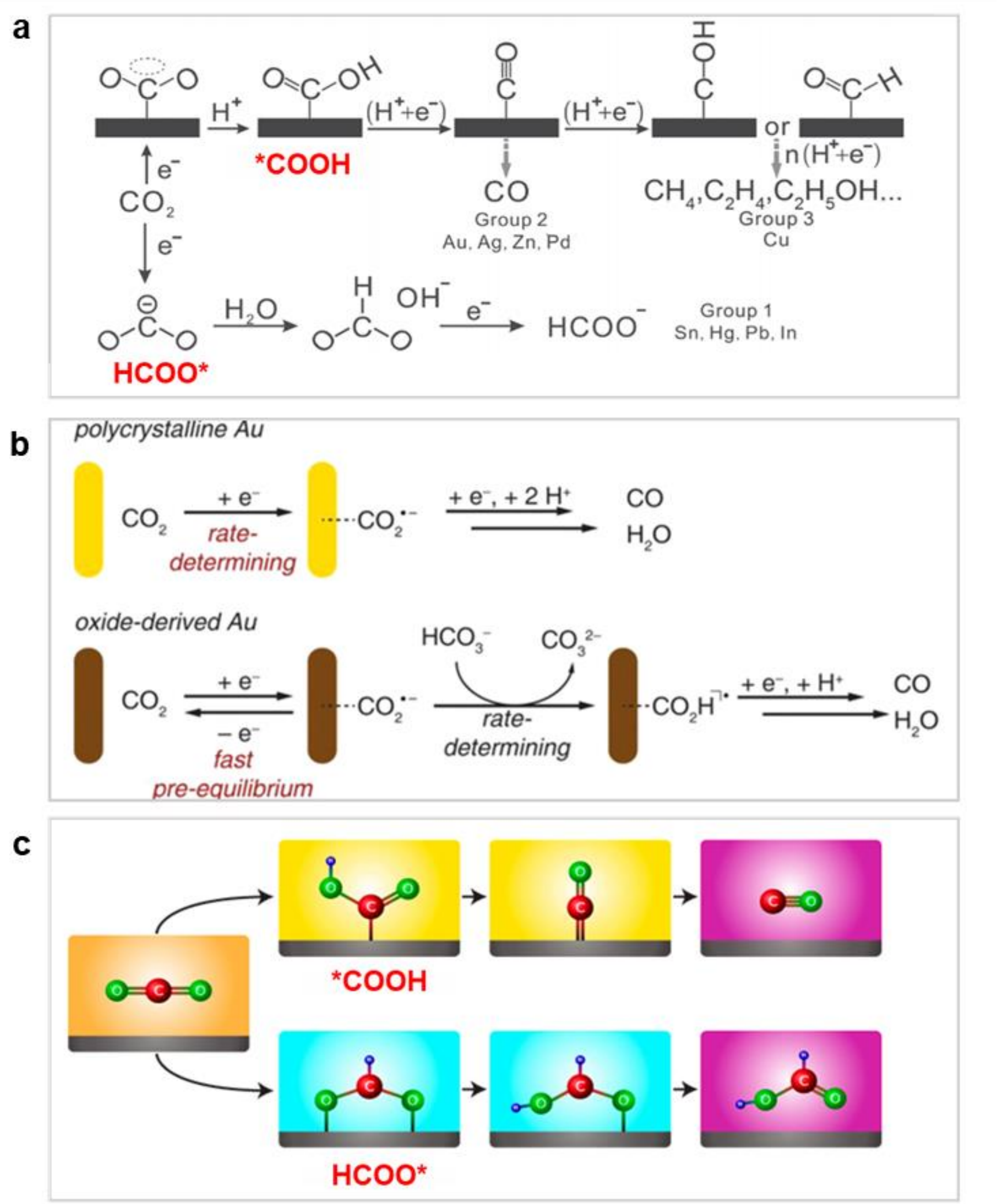

Figure 2-9. Reaction mechanism of (a) CO_2RR on metal electrodes;[92] (b) CO_2RR to CO on Polycrystalline Au and Oxide-Derived Au;[154] (c) competitive reactions of CO and $HCOO^-$ production.[155]

Figure 2-9c revealed that CO_2 may bind to the electrode surface in an initial electrochemical step via the carbon or the oxygens (resulting in single adsorption intermediate, *COOH, or a bidentate HCOO* intermediate, respectively). The second electrochemical step results in the production of CO or $HCOO^-$. HCOO* is suggested to be the key intermediate for the CO_2RR to $HCOO^-$

transformation, and optimal HCOO* binding energy supports its high selectivity for $HCOO^-$. These results suggest that oxygen-bound intermediates are critical to understanding the mechanism of CO_2 reduction to $HCOO^-$ on metal surfaces.[155] Thus, tuning and controlling the binding energies of the key reaction intermediates is critical for final product selectivity and energy efficiency of CO_2RR,[92] which is also the focus of investigations and design principles of present nanostructured materials.

The general literature background of fundamentals and metrics of CO_2RR, current methods of catalysts' synthesis and characterizations, developments of catalytic cells, and reaction mechanism of CO_2RR are reviewed to provide a context for this thesis research. Inspired by the reported findings, the following projects were performed and presented.

Chapter 3. CO_2-to-formate Transformation by Bi-Sn Bimetallic Catalyst

This chapter consists of the following paper that was co-authored by myself, my supervisors, two Ph.D. students (Bohua Ren and Zachary P. Cano), and six collaborators (Dong Un Lee, Fathy M. Hassan, Gaopeng Jiang, Eric Croiset, Zhengyu Bai, and Lin Yang). Reproduced with permission from "Orbital Interaction in Bi-Sn Bimetallic Electrocatalyst for Highly Efficient CO_2 Reduction" ***Adv. Energy Mater***. **2018**, 8, 1802427." Copyright 2018 2018 WILEY-VCH Verlag GmbH & Co. KGaA, DOI: org/10.1002/aenm.201802427. *Featured on Cover*.

Statement of Contributions: I devised the concept, designed all experiment, and prepared the manuscript draft; D. Lee and I performed synthesis and characterizations of materials, and conducted electrochemical measurements; B. Ren carried out DFT calculations and analyses; F. Hassan, G. Jiang, and I performed the analyses and interpretations of experimental results; J. Gostick and I developed the FEM model; E. Croiset reviewed the results and revised the manuscript; Z. Bai, L. Yang, Z. Cano provided a critical review of the manuscript; Z. Chen directed the research. All authors participated in the discussion and commented on the results.

3.1. Introduction

The conversion of carbon dioxide (CO_2) into value-added chemicals by electrochemical CO_2 reduction reactions (CO_2RR) is considered as a promising strategy for recycling CO_2 with sustainable and environmental benefits.[2, 5, 7, 11-12, 33-34] This can be performed efficiently in the future by coupling CO_2 conversion technologies with renewable but intermittent sources of energy such as wind and solar power.[32, 35] However, CO_2RR, in general, is difficult due to CO_2 being thermodynamically stable,[156-157] resulting in very sluggish reaction and huge activation overpotentials during electroreduction. Additionally, the conversion of CO_2 competes against other reactions such as the hydrogen evolution reaction (HER) which usually significantly decreases the formation of reduced carbon products. One interesting product which results from CO_2 conversion is formate, which is a stable nontoxic liquid that has large market potential in various applications including hydrogen carrier systems[14, 66-67] and formic acid fuel cells.[68-69] However, highly active, selective, and stable electrocatalysts are still required to facilitate CO_2RR and overcome large energy barriers and shift reaction pathways toward formate formation.

Based on previously reported studies, most metal-based catalysts such as Au,[6, 154] Ag,[133-135] and Ni[158-159] were shown to demonstrate a low selectivity toward the formation of formate, favoring the conversion of CO_2 to CO, while Cu was demonstrated to produce a variety of hydrocarbons and alcohols at low Faradaic efficiencies.[1, 3, 9, 160-161] Interestingly, Pd,[125-126, 162] Sn,[102, 104, 106, 148, 163] Bi,[72-73, 164-165] In,[70] and Pb,[1] on the other hand, have demonstrated relatively high selectivity for formate production. Pd shows high selectivity with relatively low overpotentials, but it is too expensive for large-scale CO_2 reduction systems. Meanwhile, In and Pb are known to be toxic and not environmentally friendly, which leaves Sn and Bi as good candidates for formate producing catalysts. These metals, being comparatively inexpensive and environmentally benign, are also interesting as electrode materials for large-scale CO_2 reduction systems to be integrated into smart energy-grids.[74, 98] In terms of the catalyst composition, combining more than one element in the form of binary or multi-component catalysts have shown to be an effective approach to tune the selectivity of CO_2RR catalysts.[44, 49-50, 76-78] However, a wide range of Faradaic efficiencies for formate production ($FE_{formate}$) from 40 to 99 % has been reported on various binary Sn-based electrodes. Improved $FE_{formate}$ has been observed on binary Sn-based catalysts where Pd,[76] Ag,[50] Cu,[49], and S[74] were introduced as the secondary element, while the introduction of metals such as Cd and Zn[166] have shown decreased $FE_{formate}$. These results indicate that the formation of formate is sensitive to the electronic structure of the Sn surface which can be modified by introducing other atoms. As such, understanding the synergetic interaction[167] between binary components is of significant importance in designing catalysts that can perform the conversion of CO_2 to formate at high Faradaic efficiencies. In addition, another way to enhance the activity and selectivity of catalysts for CO_2RR is through morphology engineering[168-170] and tuning of oxidation states at the surface of catalysts.[32, 163-164, 171] In general, high surface area catalysts increase the active sites exposure and allow for specific crystal edge and step sites to interact with reactants.[6, 71] The results from the literature suggest that by appropriately combining concepts from the compositional and morphological studies, a formate producing CO_2RR catalyst with high activity and selectivity can be produced.

Herein, I have designed and synthesized a bimetallic Bi-Sn catalyst for the efficient production of formate. The combined effects of Sn and Bi components along with unique morphology control results in high formate partial current density as well as long durability, showing almost exclusively formate production over 100 hours of operation. On this basis of physicochemical, electrochemical, and DFT analyses, these excellent traits of the catalyst are ascribed to four factors: (i) the interface between Sn and Bi is highly favorable for charge transport due to the higher electronegativity of Bi, allowing electron density to easily flow from Sn to Bi. The sub-atomic orbital interaction, therefore, strengthens the interaction at the active site with the HCOO* intermediate, boosting the selectivity for formate over CO and H_2; (ii) the Bi-Sn nanosheet structure is observed to be very robust from electron microscopic analysis, maintaining the highly favorable bimetallic interaction necessary for selective formate production; (iii) the nanosheet structure with enhanced edge sites exposure promotes mass transport of CO_2 and formate ions during the reactions; (iv) the fabrication of CO_2RR electrode is possible without the use of binding material, significantly reducing the electronic resistance. In summary, these advantages lead to the development of a catalyst system that can efficiently convert CO_2 to formate at high current densities for extended periods, which will be demonstrated in the following sections.

3.2. Results and Discussion

3.2.1. Fabrication of Bimetallic Bi-Sn Electrodes

A schematic diagram illustrating the structure of the Bi-Sn bimetallic catalyst deposited on a flexible carbon fabric substrate is shown in **Figure 3-1a**, which is used as a CO_2RR electrode without further modification. As described in the 4.0 Experimental Methods, SnO_2 nanosheets were deposited on a flexible carbon substrate by a facile and scalable hydrothermal reaction technique, followed by the electrodeposition of Bi nanoparticles uniformly onto the surface of SnO_2 nanosheets. High surface area carbon fabric was used as the growth substrate during the hydrothermal reaction, which allowed SnO_2 nanosheets to grow vertically without any addition of polymer binders, such as polytetrafluoroethylene (PTFE) or Nafion, which usually lower the overall electronic conductivity of the electrode. Additionally, this method can be deployed for gas diffusion electrode fabrication for future gas-phase CO_2 electrolyzer applications. Prior to testing for CO_2RR activity, the as-synthesized catalyst was exposed to an in-situ electrochemical reduction conditioning step by applying a constant potential of -1.14 V vs. RHE for 20 min to reduce SnO_2 to Sn nanosheets, similarly to previously reported methods in the literature.[50, 58] Therefore, a portion of the current observed during the in-situ electrochemical reduction is ascribed to the reduction of SnO_2 to Sn (**Figure S3-1**). To prevent re-oxidation of the freshly prepared surface, the electrode was tested immediately in the same electrolyte without exposing it to the open environment, which allowed CO_2RR to occur over the Bi-Sn surface.[50, 75, 101]

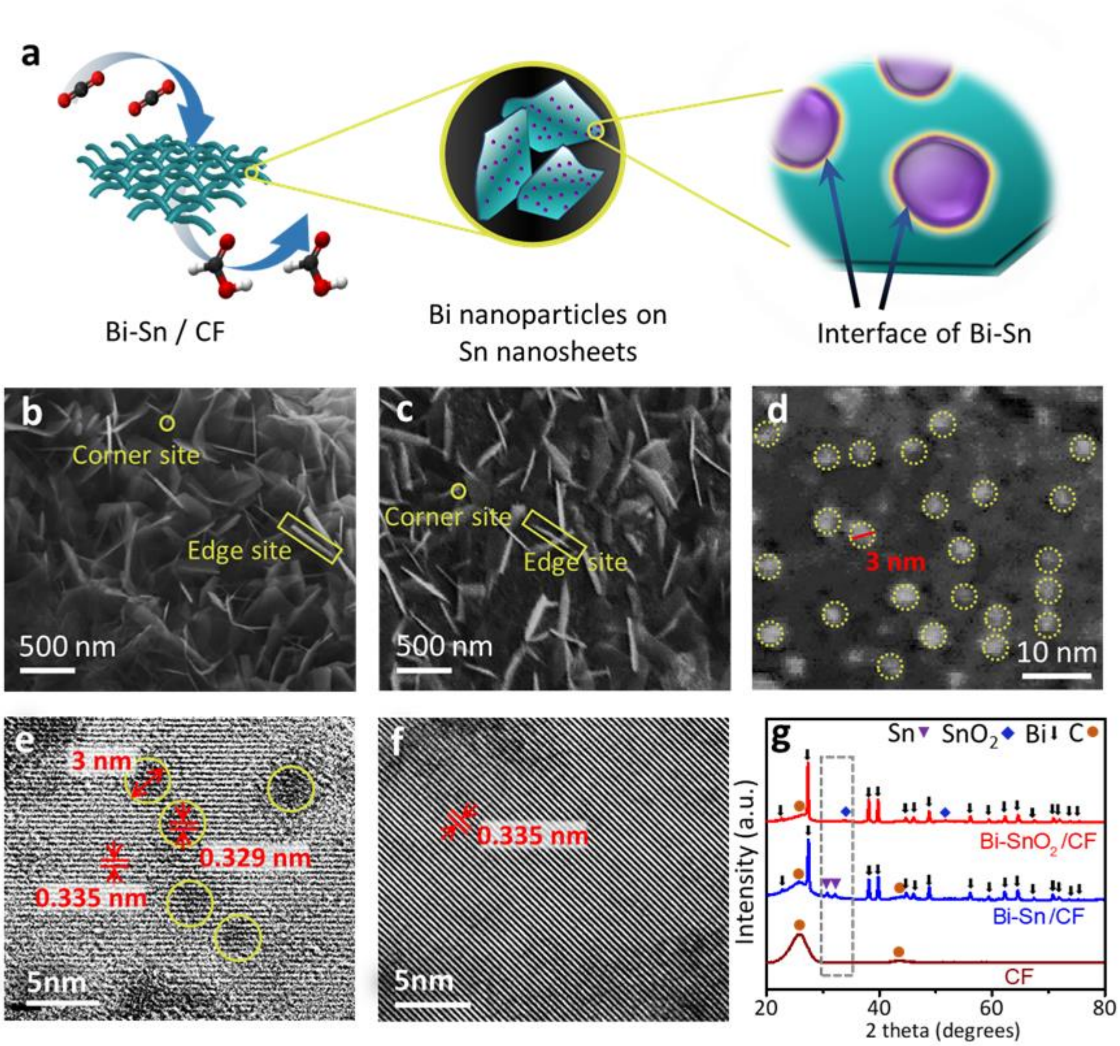

Figure 3-1. (a) A schematic illustration of the Bi-Sn catalyst structure grown on porous carbon fabric substrate, and the active interface formed by Bi nanoparticle deposition on Sn nanosheets. SEM images of Bi-Sn/CF catalyst (b) before, and (c) after the in-situ pre-conditioning reduction step, respectively. (d) STEM image of the surface of a Bi-SnO_2 nanosheet. HRTEM images of (e) Bi-decorated, and (f) Bi-free SnO_2 nanosheet, respectively. (g) XRD patterns of the catalysts: Bi-SnO_2/CF, Bi-Sn/CF, and CF. Sn: JCPDS 04-0673; SnO_2: JCPDS 41-1445; Bi: JCPDS 44-1246; C: JCPDS 41-1487.

As revealed by scanning electron microscopy (SEM), 2D vertically-standing Bi-SnO_2 nanosheets successfully are observed to grow directly on the porous carbon substrate as shown in **Figure 3-1b** and **Figure S3-2a**. This structure is very advantageous for increasing the surface area since unsupported 2D nanostructures tend to agglomerate and lose active surface area. No obvious morphology change is observed after the in-situ electroreduction of Bi-SnO_2 nanosheets as shown in **Figure 3-1c**. The surface of the nanosheets may have re-oxidized during the SEM characterization, but this image is still indicative of no significant morphological change resulting from the in-situ electroreduction. The SEM images of various electrodes fabricated using varying Bi deposition times (SnO_2/CF, Bi(0.1)-SnO_2/CF, Bi(0.5)-SnO_2/CF, Bi-Sn/CF and Bi(3)-SnO_2/CF) show similar vertically standing nanosheet morphology (**Figure S3-2b**, **2c**-**f**, respectively).

As shown by the scanning TEM (STEM) and high-resolution TEM (HRTEM) images in **Figure 3-1d** and **e**, small Bi particles attached to the surface of SnO_2 nanosheets are observed be 3 nm in average diameter and with a *d*-spacing of 0.329 nm that corresponds to the (102) plane of Bi.[71] In comparison, SnO_2 nanosheets show lattice fringes with a *d*-spacing of 0.335 nm which corresponds to the (110) plane of SnO_2 in both Bi-decorated and Bi-free samples (**Figure 3-1e** and **f**, respectively).[106] The elemental constituents of the electrodes are revealed by energy-dispersive X-ray spectroscopy (EDX) as shown in **Figure S3-3**, which clearly indicates the presence of both Bi and Sn. It is important to carefully control the Bi deposition time as the excessive current passed during this step leads to aggregation and formation of relatively large Bi clusters as shown by SEM and TEM images (**Figure S3-2g, 2h,** and **S3-4**).

To further characterize Bi-Sn electrodes, XRD was conducted to study the crystal structure of the Bi-SnO_2/CF electrode, which clearly showed peaks that matched Bi (JCPDS# 44-1246) and SnO_2 (JCPDS# 41-1445) (**Figure 3-1g**). Even though no morphological change was observed before and after the in-situ reduction of the electrodes based on the SEM analysis above, the XRD patterns of Bi-SnO_2/CF and Bi-Sn/CF in **Figure 3-1g** clearly show the disappearance of the SnO_2 peaks and emergence of Sn peaks at 30.6 ^{o} and 32.0 ^{o} which correspond to the (200) and (101) planes

(JCPDS# 04-0673). The same trend was observed with other Bi(x)-SnO_2/CF and oxide-derived Bi-Sn/CF electrodes as shown by their XRD patterns (**Figure S3-5**).

Further composition and valence state study of the Bi(x)-SnO_2/CF electrodes have been conducted by X-ray photoelectron spectroscopy (XPS). The obtained XPS spectra are calibrated via alignment of the C(sp2) peak position in the C 1s spectrum to its reference value of 284 eV. The survey XPS spectrum (**Figure S3-6a**) clearly confirms that the samples consist of the elements of Bi, Sn, O, and C. Moreover, the high-resolution core spectrum of Sn $3d_{5/2}$ and Sn $3d_{3/2}$ (**Figure S3-6b**) show that the two main peaks (486.77/495.18 eV in Bi-SnO_2/CF, and 486.70/495.11 eV in Bi-Sn/CF, respectively) correspond to Sn^{4+} in SnO_2.[76] The transition from SnO_2 to Sn after the in-situ electroreduction is observed by the negative shift in the binding energy of 0.07 eV from Bi-SnO_2/CF to Bi-Sn/CF as shown in **Figure S3-6b**. Despite the electrode having undergone re-oxidation due to the air exposure during sample transport to XPS, the electrode still maintained this shift indicative of the robustness of the in-situ reduction process.

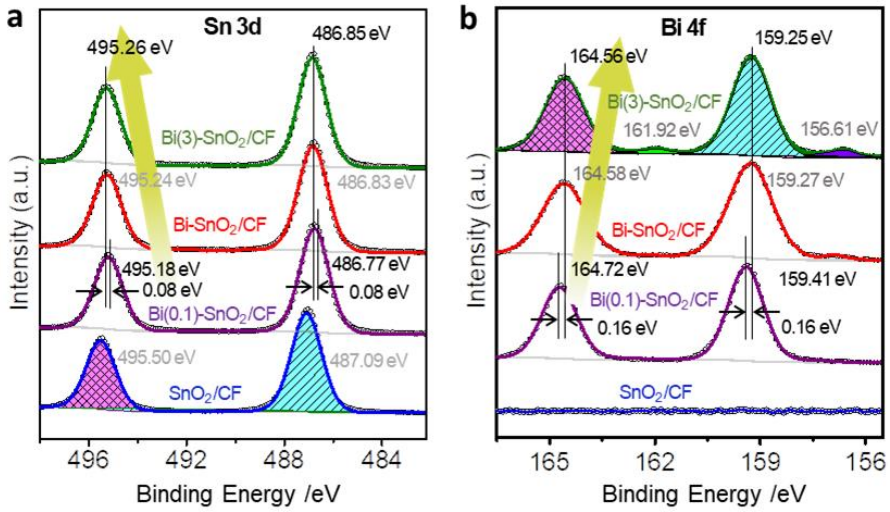

Figure 3-2. (a) Sn 3d and (b) Bi 4f core-level XPS spectrum of Bi(3)-SnO_2/CF, Bi-SnO_2/CF, Bi(0.1)-SnO_2/CF, and SnO_2/CF.

As shown in **Figure S3-6c**, the peak profile of Bi 4f (159.27/164.58 eV and 158.57/163.85 eV for Bi-SnO_2/CF and Bi-Sn/CF, respectively) indicates that Bi^{3+} species dominate as the main component of bismuth oxide.[172] The small peaks at 156.22/161.70 eV are ascribed to $Bi^0$4f on the surface. The XRD patterns only show the metallic Bi phase in both Bi-SnO_2/CF and reduced Bi-Sn/CF samples as it is a bulk probing technique, while the surface sensitivity of XPS allows characterization of the oxidation states of Bi nanoparticles. The binding energies of $Sn3d_{5/2}$ and $Sn3d_{3/2}$ peaks shift to larger energies with increasing amounts of Bi as shown in **Figure 3-2a**. Specifically, Bi(0.1)-SnO_2/CF has the lowest $Sn3d_{5/2}$ and $Sn3d_{3/2}$ binding energies. On the other hand, as the amount of Bi increases, $Bi4f_{7/2}$/ $Bi4f_{5/2}$ peaks shift to lower binding energies. In addition, the Bi(3)-SnO_2/CF has the lowest Bi $4f_{7/2}$/ Bi $4f_{5/2}$ binding energy (**Figure 3-2b**). These results are clear indications of the transfer of electrons from Sn to Bi atoms, which modifies the overall electronic structure of the active sites at the Bi-Sn interfaces. The interaction of Sn and Bi orbitals and how it affects the formation of formate during CO_2RR will be discussed with both experimental and computational results.

3.2.2. Electrochemical CO_2 Reduction Performance

As mentioned above, the oxide-derived Bi(x)-Sn/CF electrodes are tested immediately following the in-situ pre-condition reduction step to prevent surface re-oxidation. The CO_2RR activity of the prepared electrodes (Bi-Sn/CF, Sn/CF, and CF) are measured by linear sweep voltammetry (LSV) (**Figure 3-3a**). Under N_2 bubbling of 0.5 M $KHCO_3$ electrolyte, the increase in the current past -0.7 V is ascribed to the hydrogen evolution reaction (HER), which is the main competing reaction during the CO_2RR. With the CO_2-purged electrolyte, however, a dramatic current increase is observed which indicates that the CO_2RR occurs readily on the Bi-Sn catalyst.[49] A series of constant potential electrolysis (CPE) measurements are performed to investigate the potential dependence of the electrode on $FE_{formate}$ as shown in **Figure 3-3b**. With increasing overpotential, $FE_{formate}$ was found to continuously increase for all electrodes tested, reaching a maximum at -1.14 V vs. RHE, then decreasing slightly after this point. This trend might be due to mass transport limitations of CO_2. Oxide-derived Bi-Sn/CF bimetallic catalyst demonstrated the highest $FE_{formate}$ of 94 ± 2 % at -1.14 V vs. RHE, while $FE_{formate}$ was 78 ± 2% on the Sn/CF electrode at -1.14 V vs. RHE. Although a wide range of $FE_{formate}$ from 40 to 99 % has been reported on various Sn-based electrodes (**Table S3-1**), the Bi-Sn/CF electrode presented in this study, which has the advantages of non-precious metal composition and a practically viable fabrication method, demonstrates both very high FE and current density. These excellent performance metrics are attributed to the unique Sn nanosheet structures which consist of many edges and corner sites that lead to a strong local electric field as depicted in **Figure S3-7**. According to the field-induced reagent concentration (FIRC) theory,[6] high-curvature structures concentrate electric fields which can affect local ion concentrations and in turn lead to a high local concentration of CO_2 close to the active CO_2 reduction reaction surface.[6, 71, 173] The Bi/CF electrode exhibits a $FE_{formate}$ of 78 ± 2% (**Figure S3-8a**), which is slightly lower than the reported values obtained with Bi dendrites,[72] nanoflakes,[71] and nanosheets.[73, 164] This is likely due to the agglomeration of Bi particles into clusters during the electrodeposition in the absence of SnO_2 nanosheets (**Figure S3-5h**), resulting in the loss of high-index planes,[72] corner and edge sites[71] or under-coordinated Bi sites[164] which are responsible for high CO_2RR activity in Bi dendritic and nanoflake structures.

The decreasing $FE_{formate}$ at high overpotentials is indicative of the formation of hydrogen and CO outcompeting the reduction of CO_2 to formate, as shown by the product distribution in **Figure 3-3c**. This competition between the production of formate, hydrogen, and CO is commonly observed and reported in the literature.[75] However, it is important to note that the optimized Bi-Sn catalyst composition and morphology in this study highly favors the production of formate, as Faradaic efficiency toward CO is kept below 10 % and the rest being hydrogen at all potentials tested. No other products aside from CO, H_2, and formate are observed, which simplifies product separation in practical applications because the formate-containing liquid electrolyte can be easily separated from CO and H_2. This allows the electrolyte to be readily refined and used as the hydrogen carrier[14, 16, 66-67] or as the fuel for formic acid fuel cells.[68-69]

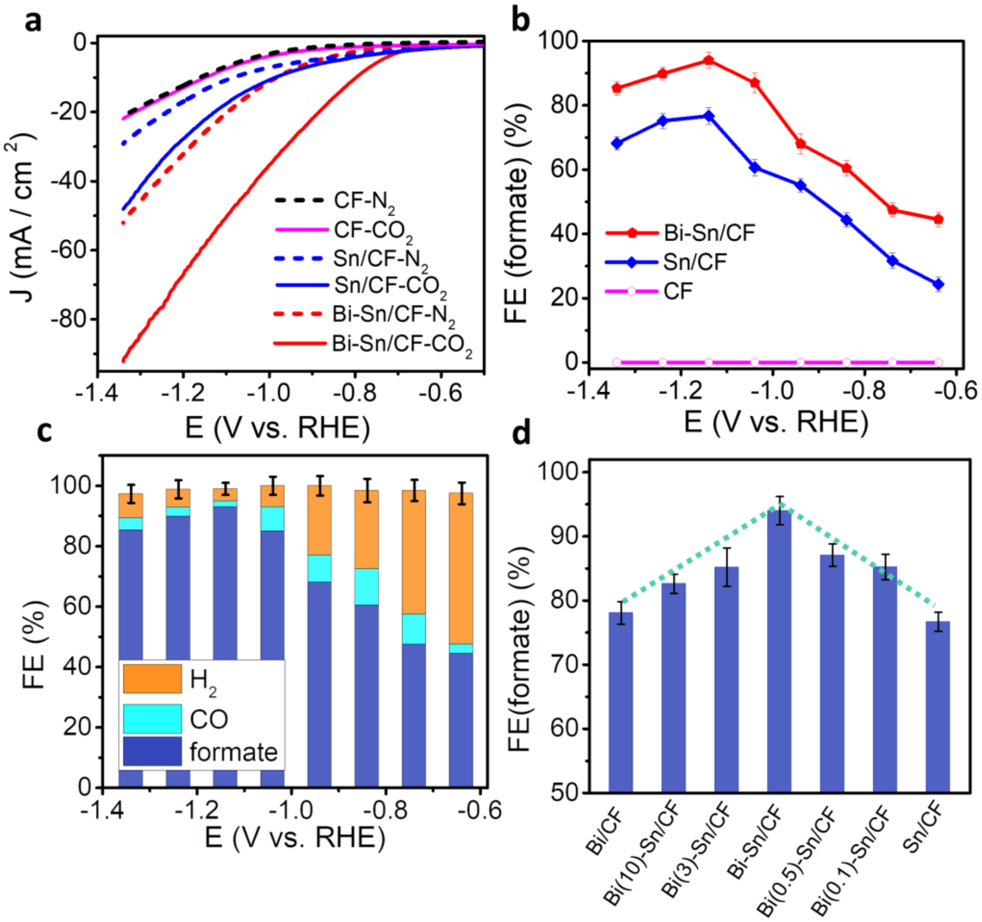

Figure 3-3. (a) CO_2RR activities of the prepared electrodes (Bi-Sn/CF, Sn/CF, and CF) in an N_2- (dotted line) or CO_2-purged (solid line) 0.5 M $KHCO_3$ electrolyte at a scan rate of 20 mV s^{-1}. (b) FE of formate generated on electrodes (Bi-Sn/CF, Sn/CF, and CF) at a series of potentials from -0.64 to -1.34 V. (c) FE of formate, CO and H_2 on oxide-derived Bi-Sn/CF electrodes at a series of potentials from -0.64 to -1.34 V. (d) FE of formate with varying ratios of Bi and Sn at -1.14V vs. RHE. The error bars represent the standard deviations of three independent measurements of the same sample.

The effect of Bi deposition on the selectivity of CO_2RR also was explored by varying the electrodeposition time of Bi on SnO_2 nanosheets, resulting in the different compositions of Bi-Sn bimetallic catalysts. The electrochemical testing reveals the 1:1 ratio of Bi: Sn to demonstrate the highest $FE_{formate}$ as shown in **Figure 3-3d**, with either increasing or decreasing amounts of Bi leading to the reduction of $FE_{formate}$. Structurally, these electrodes are observed to be different as shown in **Figure S3-2** and **S3-4**, with the best performing Bi-Sn electrode displaying a uniform distribution of 3-nm Bi nanoparticles on Sn nanosheets surfaces, greatly increasing the exposure of the active Bi-Sn interfaces. In comparison, electrodes with a Bi: Sn ratio lower than 1 were observed to be absent of Bi nanoparticles (**Figure S3-4b**), while electrodes with a Bi: Sn ratio larger than 1 lead to the formation of relatively larger Bi clusters due to the agglomeration of Bi nanoparticles (**Figure S3-4d**).

Interestingly, all electrodes fabricated and tested still show considerably favorable CO_2RR activity toward formate production resulting in a $FE_{formate}$ of over 75 % (Table S3-1). Regardless, these results obtained from different Bi-Sn compositions indicate that the amounts of each element have a strong influence on the structure of the catalyst which in turn dictates the product selectivity during CO_2RR. Although various Sn-based bimetallic catalysts have been studied as shown in **Table S3-1**, such as Pd/Sn,[76] Ag/Sn,[50] Zn/Sn,[166], and Cu/Sn,[49] the selectivity is varied indefinitely between CO and formate. For instance, the production tendency of CO and formate depends on the thickness of SnO_2 shell in a Cu/SnO_2 core/shell catalyst.[49] Based on this optimized Bi-Sn bimetallic composition and morphology, the electrode fabrication can be readily scaled up to produce highly efficient CO_2 reduction active gas diffusion electrodes for high conversion rate devices such as CO_2 electrolyzers.

One other point to highlight in this study is the use of flexible and porous carbon fabric as a high surface area growth substrate, which directs the uniform growth of Sn nanosheets and increases the exposure of the active site. The porous nature of the electrode significantly promotes the diffusion of the dissolved CO_2 into the active sites and the products out of the electrode by the freely flowing electrolyte.[75, 106, 174] Therefore, the interactions between the catalyst and the surrounding fluid are enhanced. As **Figure S3-8b** shows, the production rate of formate can be as high as 0.74 mmol h^{-1} cm^{-2} for the oxide-derived Bi-Sn/CF electrode at the optimum potential, which is remarkable in comparison to 0.2 mmol h^{-1} cm^{-2} as reported in a previous study of a tin-based CO_2RR catalyst.[98] The easily scalable composite oxide-derived Bi-Sn/CF electrodes can be sandwiched with a hydrophobic gas diffusion layer to compose a gas diffusion electrode, which is a good candidate for industrial CO_2-consuming flow electrolyzers.[18]

3.2.3. Stability of Oxide-derived Bi-Sn/CF Electrode

The durability of the oxide-derived Bi-Sn/CF electrode is demonstrated by conducting CO_2RR at the optimum potential for an extended period of up to 100 h. The resulting current density and FE toward formate are observed to slightly fluctuate due to increasing concentrations of formate in the electrolyte, which is a common phenomenon observed in batch type reactors.[98] In order to eliminate the effect of variation of formate concentration in the electrolyte, the electrolyte was replaced with a fresh electrolyte every 20 hours. The durability testing proceeds by applying a constant potential of -1.14 V vs. RHE, where the highest $FE_{formate}$ is observed, without changing any other cell component. The $FE_{formate}$ is calculated every 20 hours of operation, and the concentration of formate is found to be as high as 180 mM. The oxide-derived Bi-Sn/CF electrode exhibits excellent stability over 100 hours of operation without any obvious degradation in FE or partial current density of formate as shown in **Figure 3-4** and **Figure S3-9**, which is likely attributed to the strong anchoring effect between the active Bi-Sn structure and the carbon fabric substrate which are observed to be unchanged even after long-term durability testing (**Figure 3-4**, inset).

3.2.4. Computational Analysis

Periodic Density Functional Theory (DFT) calculations were conducted to support the experimental results obtained above for high CO_2 reduction activity toward formate production on the Bi-Sn bimetallic catalyst. The computational analysis considers two main pathways for CO and $HCOO^-$ production from the adsorption of bicarbonate (CO_3H^*) species (**Figure S3-10**), which is reported as the primary carbon source for formate production during CO_2 electroreduction in the literature.[76, 154, 175] **Figure S3-10c** shows the binding of CO_3H^* to the electrode surface during the initial electrochemical step to the carbon atom (R1a) and the oxygen atom (R1b) resulting in the formation of the COOH* and HCOO* intermediates, respectively.[50, 65, 155] The second electrochemical step (R2) results in the production of CO (R2a) or HCOOH (R2b).[65]

$$CO_3H^* + H^+ + e^- \rightarrow COOH^* + OH^* \tag{R1a}$$

$$COOH^* + H^+ + e^- \rightarrow CO^* + H_2O^* \tag{R2a}$$

$$CO_3H^* + H^+ + e^- \rightarrow HCOO^* + OH^* \tag{R1b}$$

$$HCOO^* + H^+ + e^- \rightarrow HCOOH^* + {}^* \tag{R2b}$$

As depicted by the energy profiles (**Figure 3-5a** and **b**), the energy differences (ΔE_1) between the adsorption of two competing intermediates (COOH*, HCOO*) on the Sn (101) and Bi-Sn (101) surfaces are 0.55 and 0.81 eV, respectively. The energy differences of corresponding adsorbed products (ΔE_2) are 0.43 and 0.85 eV, respectively. The higher values of ΔE_1 and ΔE_2 on the Bi-Sn (101) surface indicate that the pathway involving the HCOO* intermediate leads to a more favorable formation of formate due to the changes in the electronic structure caused by interfacing with Bi nanoparticles, consistent with the experimental results.

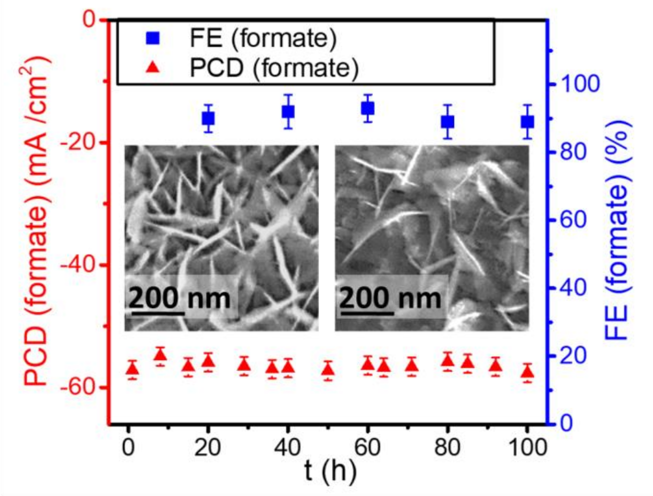

Figure 3-4. Stability of the oxide-derived Bi-Sn/CF electrode demonstrated by partial current density (PCD) and FE toward formate during long-time operation (100 h) at -1.14 V vs. RHE. Inset: SEM images of Bi-SnO_2/CF before (left) and after (right) the stability test.

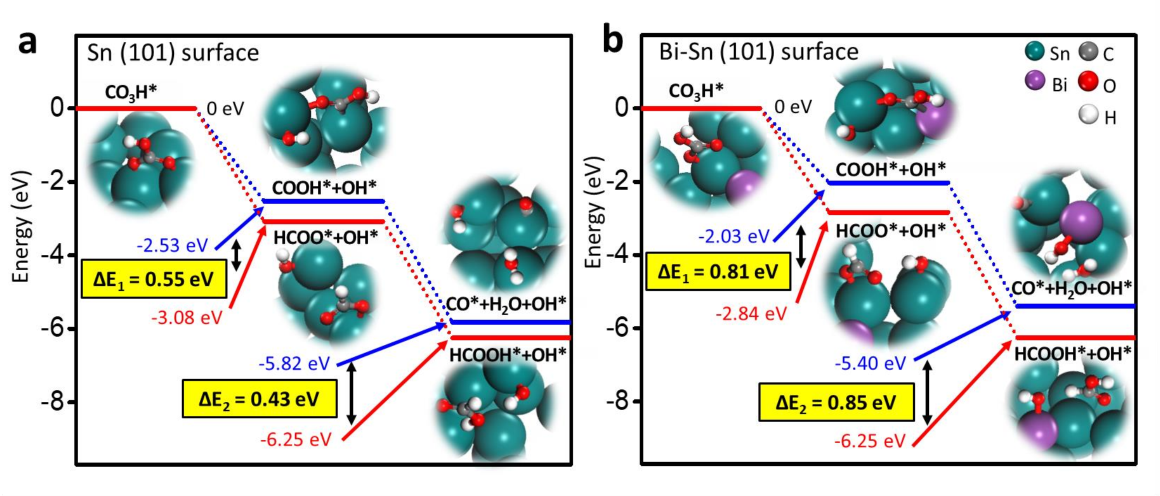

Figure 3-5. Calculated reaction energy profiles for CO_2RR to form CO (top) and HCOOH (bottom) on the (a) Sn (101) surface and (b) Bi-Sn (101) surface. All energies are regarding the energies of CO_3H adsorbed on Sn (101) or Bi-Sn (101) surface.

To better understand the reason for the higher values of ΔE_1 and ΔE_2 on the Bi-Sn (101) surface, the projected density of states (PDOS) of the O atom in adsorbed HCOO* and surface Sn atoms in Sn (101) and Bi-Sn (101) are analyzed by decomposing the electron density and the wave function into the atomic orbital contributions. As shown in **Figure 3-6a**, there are harmonic p-p and p-s overlaps between the O-2p and Sn-5s, Sn-5p states at energy levels from 0 to -10 eV in Sn (101). In contrast, for Bi-Sn (101), there are three new harmonic overlaps (α, β, and γ), showing the strong interaction between the O and Sn atoms for Bi-doped Sn (101) surface.[176] Especially for the α and γ areas, large overlaps between O-2p and Sn-4d are observed, indicating strong O-Sn bonding. The density of states at the Fermi energy level (E_f) roughly determines the availability of electrons for a given reaction.[177] Comparing the PDOS of the p orbital (**Figure 3-6b**) and d orbital (**Figure 3-6c**) of an Sn atom on Sn (101) and Bi-Sn (101) surfaces before HCOO* adsorption, both p and d orbitals of Sn electron states are up-shifted away from the Fermi level after interfacing with Bi deposits. Although Sn is not a transition metal, the d orbital of Sn electron states is still important and needs to be considered for studying the changes in electronic structures.[178] Therefore, the electron density from the more electronegative O atom is readily transferred to the p and d orbitals of the Sn atom, thus boosting the stable adsorption of the HCOO* intermediate on the Bi-Sn (101) surface and improving the selectivity of CO_2RR toward formate.[162, 179-180]

This finding is consistent with and can be used to explain other reported bimetallic component catalysts (**Table S3-1**) which have shown improved formate selectivity when secondary atoms such as Pd[76], Ag[50], Cu[49], and S[74] were incorporated into Sn, which all have a stronger electronegativity[181] than Sn. On the other hand, the formate selectivity was found to decrease with the incorporation of Cd and Zn[166], each of which has a weaker electronegativity than Sn (**Figure S3-11**). A strategic combination of binary components will thus lead to the optimum binding energy on the volcano plot, with the electron density shifting between bimetallic components due to their contrasting electronegativity values being the significant contributor.

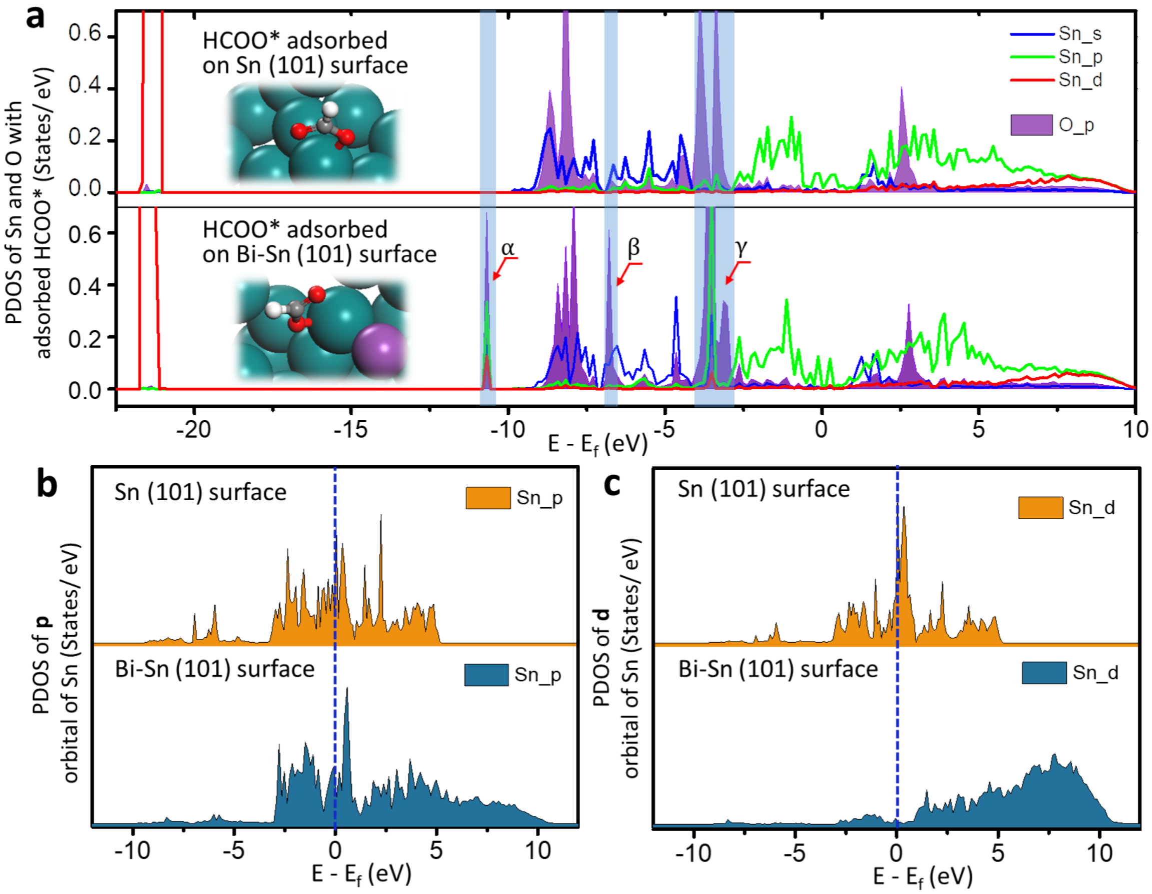

Figure 3-6. (a) Projected density of states (PDOS) of s, p, and d orbital of Sn atom and p orbital of O atom on Sn (101) and Bi-Sn (101) surfaces with adsorbed HCOO*. PDOS of (b) p orbital and (c) d orbital of Sn atom on Sn (101) and Bi-Sn (101) surfaces before HCOO* adsorption.

3.3. Conclusions

In summary, a bimetallic Bi-Sn catalyst was synthesized and investigated for a highly efficient conversion of CO_2 into formate. Due to the orbital interaction of Bi-Sn and Sn-O, the composition and morphology optimized electrode (Bi-Sn/CF) led to 96 % Faradaic efficiency for formate at -1.14 V vs. RHE with a high production rate of 0.74 mmol h^{-1} cm^{-2}. Additionally, the electrode demonstrated excellent durability of 100 hours of continuous operation with no degradation in current density and Faradaic efficiency. Furthermore, DFT simulation showed that Bi nanoparticles that formed an interface with the underlying Sn nanosheet resulted in both the p and d orbitals of Sn electron states to be up-shifted away from the Fermi level. This in turn led to the shifting of the electron density from more electronegative O atoms to the p and d orbitals of Sn atoms, thereby better stabilizing HCOO* intermediates on Bi-Sn(101) than on an undecorated pure Sn(101) surfaces. The present work sheds light on the rational design of catalysts for future CO_2RR studies by presenting a facile synthesis technique for nanostructured bimetallic catalysts and providing sub-atomic insights into electronic structure changes at the bimetallic interfaces.

3.4. Experimental Methods

3.4.1. Experimental Section

3.4.1.1. Direct growth of SnO_2 nanosheets on carbon fabrics (SnO_2/CF).

SnO_2 nanosheets were grown on a conductive high surface area carbon fabric (CF, Fuel Cell Earth). The synthesis of the SnO_2/CF electrode was conducted according to previous work in our lab.[174] Specifically, 0.5646 g of tin(II) chloride dihydrate ($SnCl_2·2H_2O$, Alfa), 0.4508 g of urea (NH_2CONH_2, Sigma-Aldrich) and 0.1122 g of ammonium fluoride (NH_4F, Sigma-Aldrich) were completely dissolved in DDI water (60 mL) under stirring, then hydrochloric acid (HCl, 37%, Sigma-Aldrich) was added drop-wise until the solution turned transparent. One piece of CF (5.0 × 5.0 cm) with the solution was transferred into a 100 ml Teflon-lined autoclave and kept at 180 °C for 10 h. After the hydrothermal process, the obtained CF was rinsed with DDI water and ethanol repeatedly and dried under vacuum at 80 °C overnight.

3.4.1.2. Bismuth decoration on SnO_2/CF (Bi-SnO_2/CF).

The as-grown SnO_2/CF was used as the substrate to electrodeposit Bi, forming Bi-SnO_2/CF. First, an aqueous bismuth solution was prepared by dissolving 0.9700 g of bismuth (III) nitrate pentahydrate ($Bi(NO_3)_3·5H_2O$, Sigma-Aldrich) in 60 mL of DDI water, then hydrochloric acid

(HCl, 37%, Sigma-Aldrich) was added drop-wise to make the solution transparent.[71, 182] One piece of SnO_2/CF (1.0 cm × 1.0 cm) was immersed in the deposition solution as the working electrode, while a saturated calomel electrode (SCE) and a platinum foil were used as reference electrode and counter electrode, respectively. The electrodeposition was conducted by applying -0.1 V vs. SCE until the desired amount (**Table S3-2**) of electron charge was passed to obtain the composite electrodes with different ratios of Sn and Bi. Pure CF also served as a substrate for the direct deposition of Bi as a comparison, which was denoted as Bi/CF. After electrodeposition, Bi(x)-SnO_2/CF and Bi/CF electrodes were cleaned with DDI water and dried in an oven at 80 °C overnight.

3.4.1.3. In-situ electrochemical reduction of Bi-SnO_2/CF (oxide-derived Bi-Sn/CF) electrode.

In-situ electrochemical reduction of the bimetallic electrode was conducted in CO_2-saturated 0.5 M $KHCO_3$ electrolyte at -1.8 V vs. SCE to electrochemically reduce the as-grown SnO_2 during the hydrothermal reaction to Sn. This pre-conditioning step is consistent with the methods mentioned in the literature for tin-based catalysts.[50, 58]

3.4.1.4. Materials Characterization.

The complex oxide-derived Bi-Sn composite electrodes synthesized in this study were characterized by the following techniques. XRD (X-ray diffraction, Rigaku Miniflex 600), and XPS (X-ray Photoelectron Spectrometer, Thermo Scientific K-alpha XPS spectrometer) was used to confirm the crystal structure and elemental composition, respectively. SEM (Scanning electron microscopy, LEO FESEM 1530) and TEM (transmission electron microscopy, JEOL 2010F) was employed to observe the morphology of the electrodes.

3.4.1.5. Electrochemical measurements.

Electrochemical CO_2 reduction was conducted in a gas-tight H-type cell with Nafion 117 membrane to separate the two compartments and prevent re-oxidation of CO_2RR products at the anode (**Figure S3-12**). One platinum wire and an SCE were used as the counter and reference electrodes, respectively. The calibration of the reference electrode was checked against a reversible hydrogen electrode (RHE) and the measured potentials (vs. SCE) were converted to RHE using the formula E(RHE) = E(SCE) + 0.235 V + 0.0591 M × pH. The electrolyte was 0.5 M potassium bicarbonate ($KHCO_3$, ≥ 99.95%, Sigma-Aldrich) saturated with CO_2 (pH = 7.2). Before electrolysis, the electrolyte was purged with CO_2 gas (99.998%, Praxair Gas) for at least 30 min. Each compartment contained 30 mL of electrolyte with a 20-ml headspace. The electrolyte in the cathodic compartment was stirred at a rate of 600 rpm to enhance mass transport of CO_2 and products around the surface of the working electrode. The working electrodes for electrolysis experiments consisted of 0.5 × 1.0 cm^2 oxide-derived Bi(x)-Sn/CF held by a clamp made of platinum. The CO_2 reduction was performed for 1 h at various potentials in the electrolyte. The electrochemical measurements were carried out using a potentiostat (BioLogic VSP300). The current densities reported in this work were normalized to the geometric surface area. The CO_2 electroreduction test was repeated three times, and the results presented are the averaged values. All the experiments were conducted under ambient pressure and at room temperature (23 °C).

CO_2*RR products analysis*: The concentration of reaction products in the liquid electrolyte was detected using a 500 MHz ^{1}H liquid NMR spectrometer (Bruker Advance) with the water suppression method. The standard solution consisted of 4.61 mM N, N-dimethylformamide (≥ 99.9%, Sigma-Aldrich) in D_2O (99.9%, Sigma-Aldrich). N, N-dimethylformamide was used as an internal reference for the chemical shifts. Typically, NMR samples were prepared by mixing 630 uL of the product-containing electrolyte and 70 μL standard solution. Formate calibration curves (**Figure S3-13**) were generated using a stock solution of sodium formate (Sigma-Aldrich). Assuming that two electrons are needed to produce one formate molecule, the Faradaic efficiency (FE) can be calculated as follows: $FE = 2\,F \times n_{formate}/Q = 2F \times n_{formate}/(I\times t)$, where F is the Faraday constant.[6]

Gas products were quantified by gas chromatography (GC, Inficon Micro 3000 GC). The GC has two channels, one equipped with a packed Molecular Sieve column and the other with a packed Plot U column. Each channel was connected to a thermal conductivity detector (TCD). Argon (Praxair Gas, 99.999%) and Helium (Praxair Gas, 99.999%) were used as the carrier gases, respectively. The gases from the outlet of the cathodic compartment were collected by a 50 CC gas-tight syringe (Perfektum), then injected into the GC. Every gas sample was measured three times. The FEs of both CO and H_2 production resulting from the electrolysis were calculated by methods reported in the literature.[29, 76]

3.4.2. DFT Calculation Methods

In order to investigate the origin of the high performance of Bi-Sn bimetallic catalysts, calculations were carried out using periodic Density Functional Theory (DFT) implemented in the Vienna Ab initio Simulation Package (VASP 5.2).[183-184] The projector-augmented wave (PAW) method was applied to solve the ion-electron interactions in a periodic system.[185] The generalized gradient approximation (GGA)[186] with Perdew−Burke−Ernzerhof (PBE)[187] functionals was used to treat the exchange-correlation interactions in the Kohn−Sham equations.[183] Spin-polarized calculations were carried out with an energy cutoff for the plane waves of 400 eV.

The convergence criteria for optimization of the atomic structure were set at 5×10^{-6} eV and a Hellmann-Feynman[188] force of 0.01eV/Å. The Gaussian smearing method (σ=0.1 eV) was used.

A Monkforst-Pack k-point mesh of 2 × 2 × 1 k-points was employed.[189-191] By increasing the cutoff energy to 450 eV and the number of k-points to 4 × 4 ×1, we observed a negligibly small change in adsorption energies (< 0.01eV) of surface species, which indicates that adsorption energy values are well converged with respect to these parameters. As previously reported,[75] CO_2 reduction occurs at a metallic Sn site and the (101) facet of Sn can be detected by HRTEM; therefore, an Sn (101) surface with 4 atomic layers and 2 × 2 unit cells was used as the model system. The interface of the Bi-Sn bimetallic electrode is important for highly selective CO_2RR. In order to simulate the role of Bi on this bimetallic catalyst, a Bi-Sn (101) surface was built by decorating one Bi atom onto the surface of pure Sn (101) surface (**Figure S3-10**). Although there were no explicit alloy peaks observed in the XRD pattern, Bi atoms at the surface of Sn can still be inserted into the underlying lattice to form a bimetallic Bi-Sn interface.[49] A vacuum layer of 15 Å was added to separate neighboring slabs to avoid possible interaction. An 8 × 8 × 1 k-points mesh was used for the density of states (DOS) calculation.

3.5. Supporting Figures and Tables

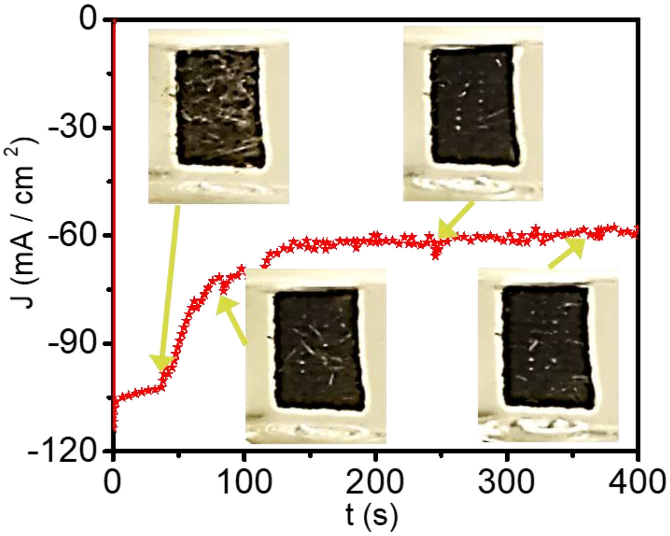

Figure S3-1. Electroreduction of SnO_2 to Sn through in-situ reduction of the electrode. Inset digital images are of the CF surfaces during electroreduction. A drastic decrease in the current is observed in the first 2 minutes during which tin oxide is reduced to tin with significant gas evolution at the electrode, which is most likely hydrogen evolution.[175, 192] When the SnO_2 was reduced to Sn, the hydrogen evolution was suppressed evidenced by fewer bubbles.

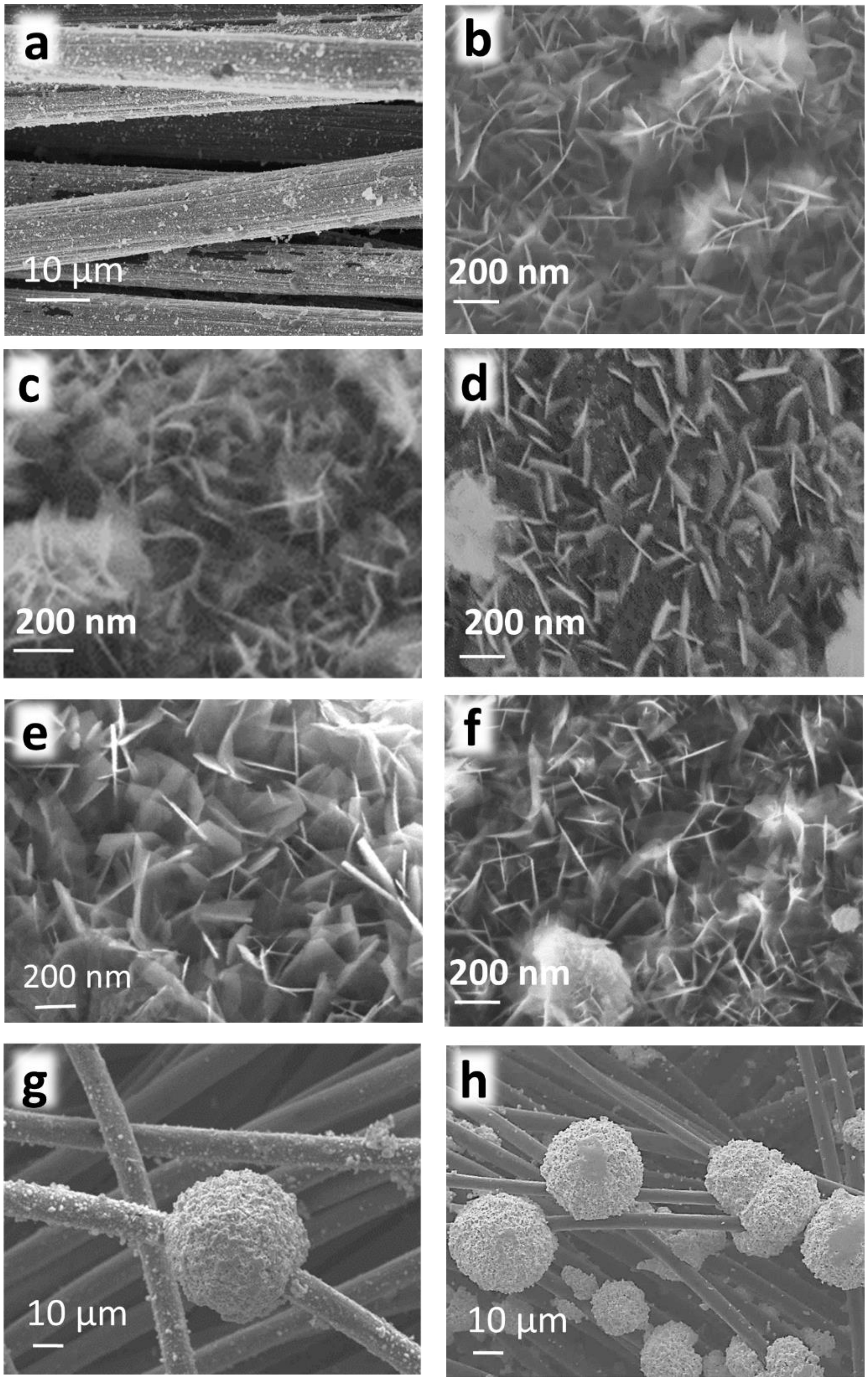

Figure S3-2. SEM images of the 3D electrodes: (a) Bi-SnO_2/CF (b) SnO_2/CF; (c) Bi(0.1)-SnO_2/CF; (d) Bi(0.5)-SnO_2/CF; (e) Bi-SnO_2/CF; (f) Bi(3)-SnO_2/CF; (g) Bi(10)-SnO_2/CF. (h) Bi/CF. The mass ratios of Bi and Sn are calculated as shown in Table S3-2.

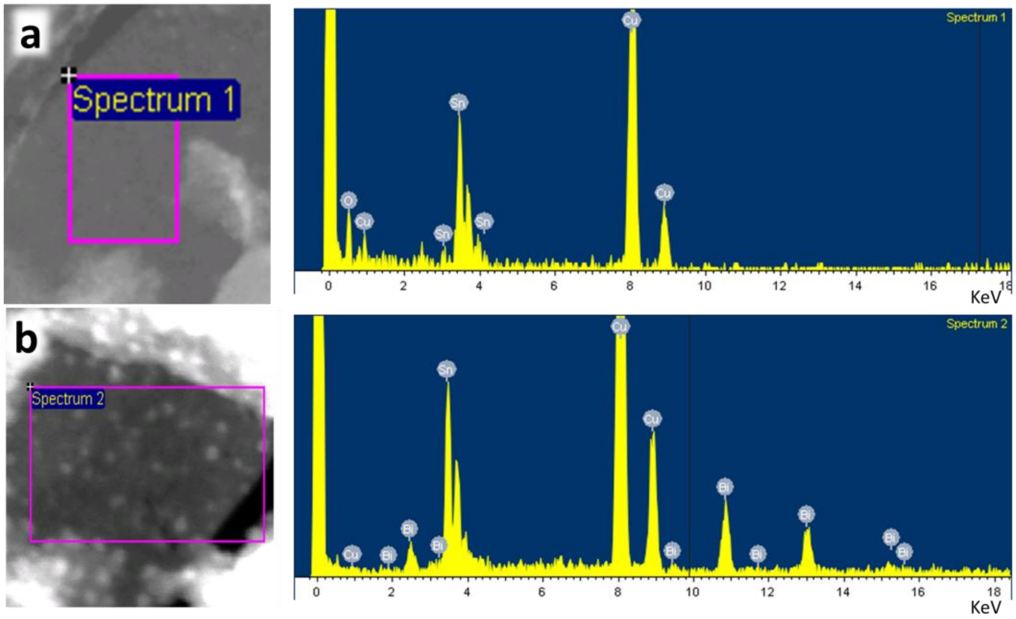

Figure S3-3. STEM images and EDX of the 3D electrodes: (a) SnO_2/CF, (b) Bi-SnO_2. (Copper peaks are from TEM copper grid.)

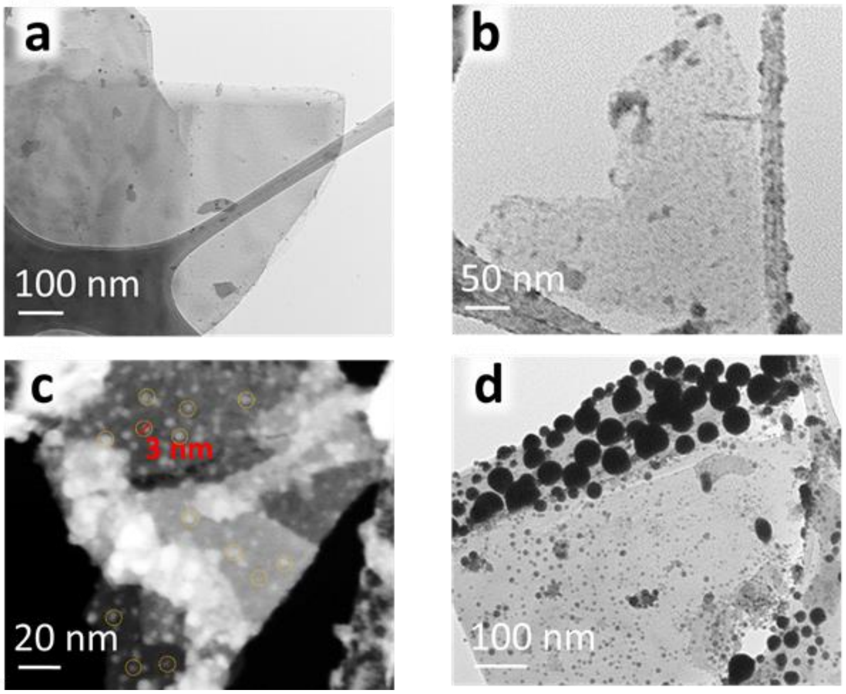

Figure S3-4. HRTEM images of (a) SnO_2 nanosheet; (b) Bi(0.1) -SnO_2 nanosheet; (c) STEM image of Bi -SnO_2 nanosheet; (d) HRTEM image of Bi(3) -SnO_2 nanosheet. The mass ratios of Bi and Sn are calculated as depicted in Table S3-2.

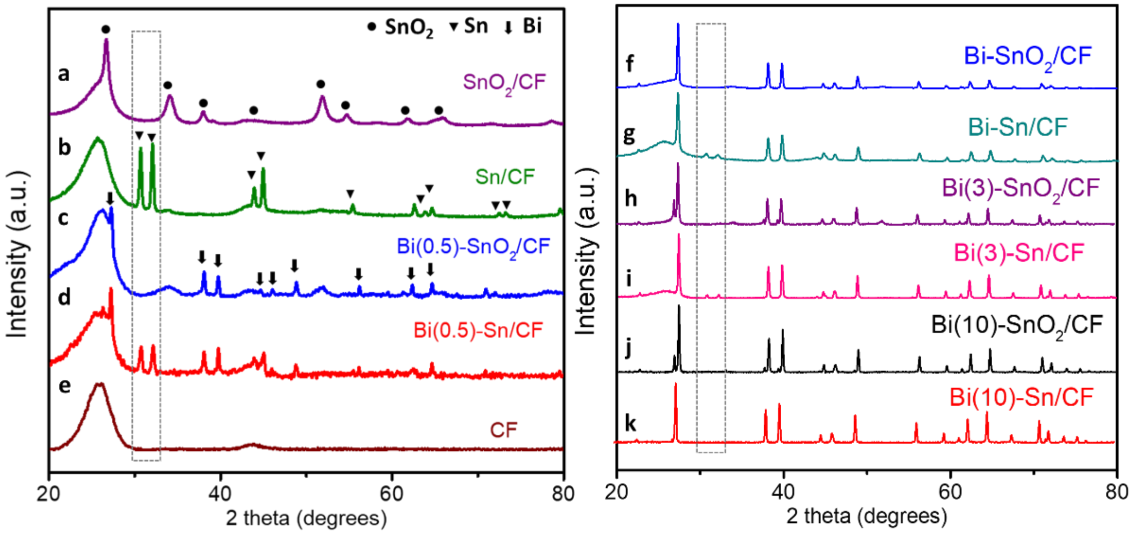

Figure S3-5. XRD patterns of the catalysts. a. SnO_2 on carbon fibers (SnO_2/CF); b. After activation, SnO_2 was reduced to Sn (Sn/CF); c. Bi was deposited on SnO_2/CF (Bi(0.5)- SnO_2/CF); d. Bi(0.5)-Sn/CF; e. bare carbon fiber (CF); f. Bi-SnO_2/CF; g. Bi-Sn/CF; h. Bi(3)-SnO_2/CF; i. Bi(3)-Sn/CF; j. Bi(10)-SnO_2/CF; k. Bi(10)Sn/CF. SnO_2: JCPDS 41-1445; Sn: JCPDS 04-0673; Bi: JCPDS 44-1246.

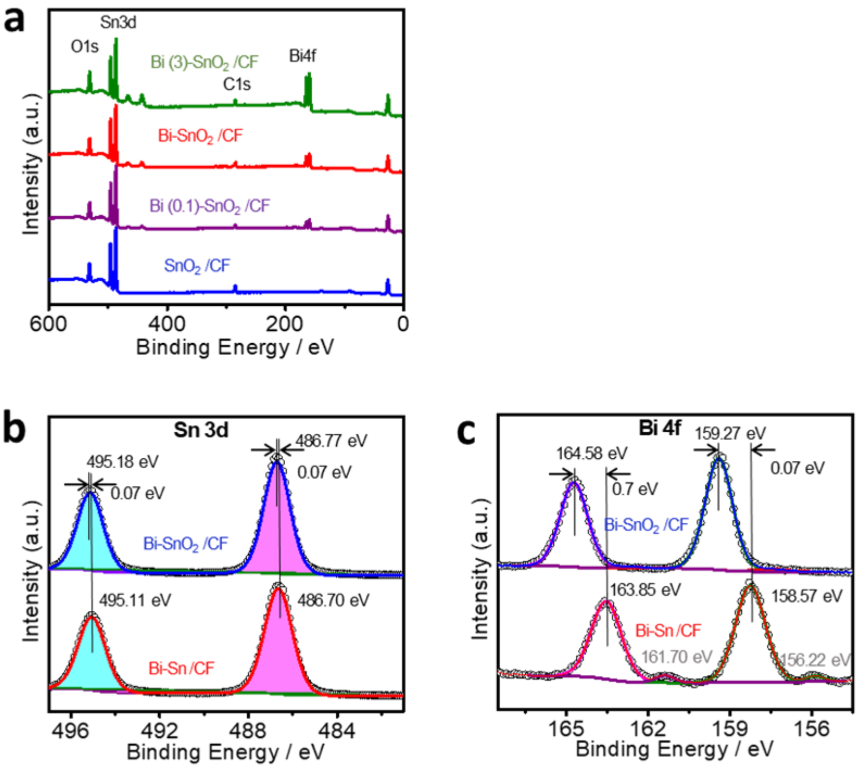

Figure S3-6. (a) Full XPS survey of Bi(x)-SnO_2/CF. (b). Sn 3d and (c) Bi4f core level XPS of Bi-SnO_2/CF (before the in-situ reduction of the electrode) and Bi-Sn/CF (after in-situ reduction of the electrode).

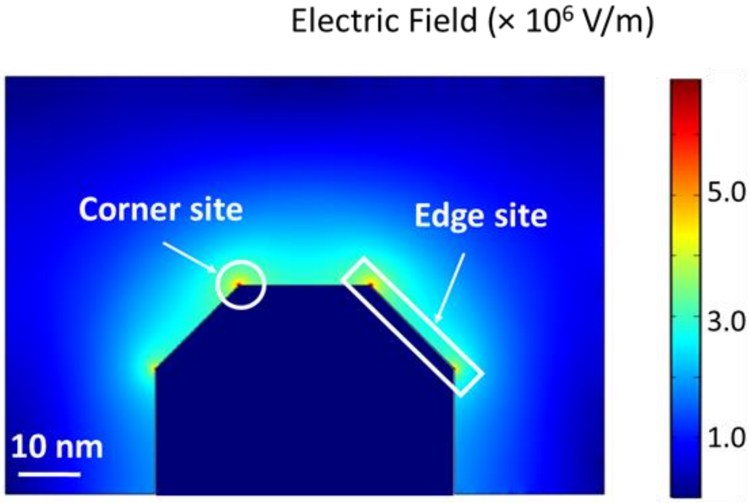

Figure S3-7. Simulated electric field distribution in two-dimensional nanosheets.

The electric field generated near the nanosheets was simulated using the COMSOL Multiphysics finite-element-based solver. The Electric Currents module was used to solve the electric field, as the opposite gradient of the electric potential V: $E = -\nabla V$. The electrolyte conductivity was taken to be 10 S·m^{-1}. [6, 71, 173] 2D models were used to represent nanosheets structures. Extremely fine triangular meshes were used for all simulations.

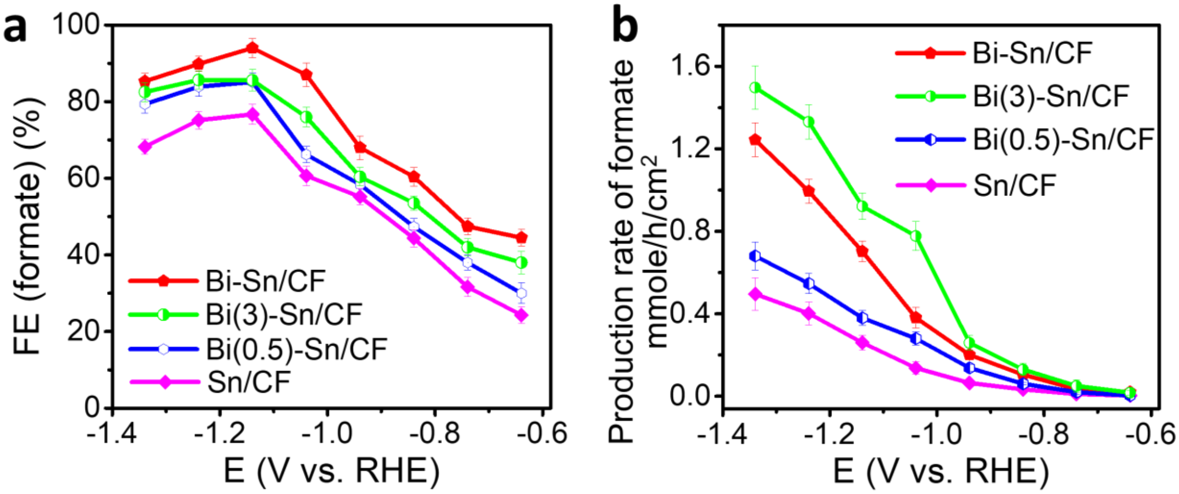

Figure S3-8. (a) FE of formate generated on oxide-derived Bi(x)-Sn/CF electrodes at a series of potentials from -0.64 to -1.34 V. (b) Production rate of formate generated on oxide-derived Bi(x)-Sn/CF electrodes at a series of potentials. The CO_2 reduction was performed for 1 h at various constant potentials from -0.54 to -1.34 V in a CO_2-bubbled 0.5 M $KHCO_3$ electrolyte.

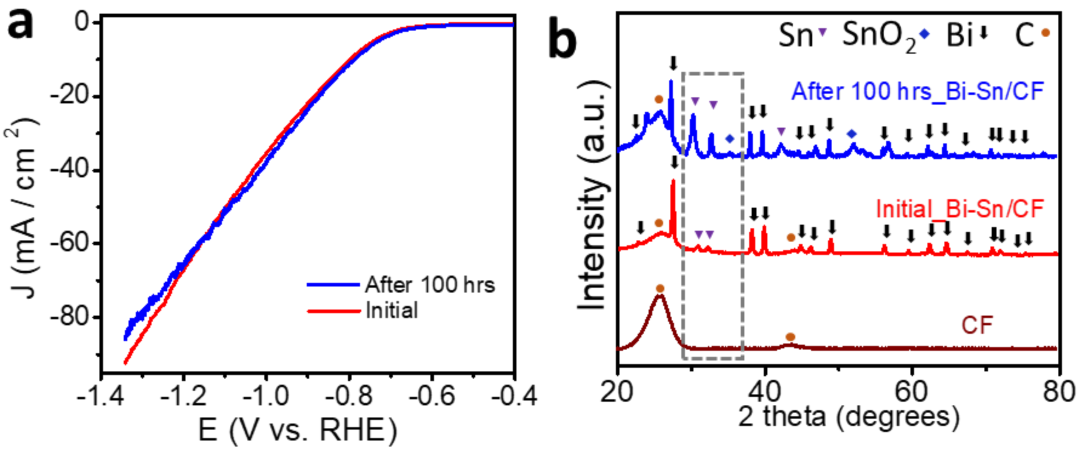

Figure S3-9. (a) CO_2RR activities of the Bi-Sn/CF electrodes before and after the stability test in a 0.5 M $KHCO_3$ electrolyte at a scan rate of 20 mV· s^{-1}. (b) XRD patterns of Bi-SnO_2/CF before and after the stability test.

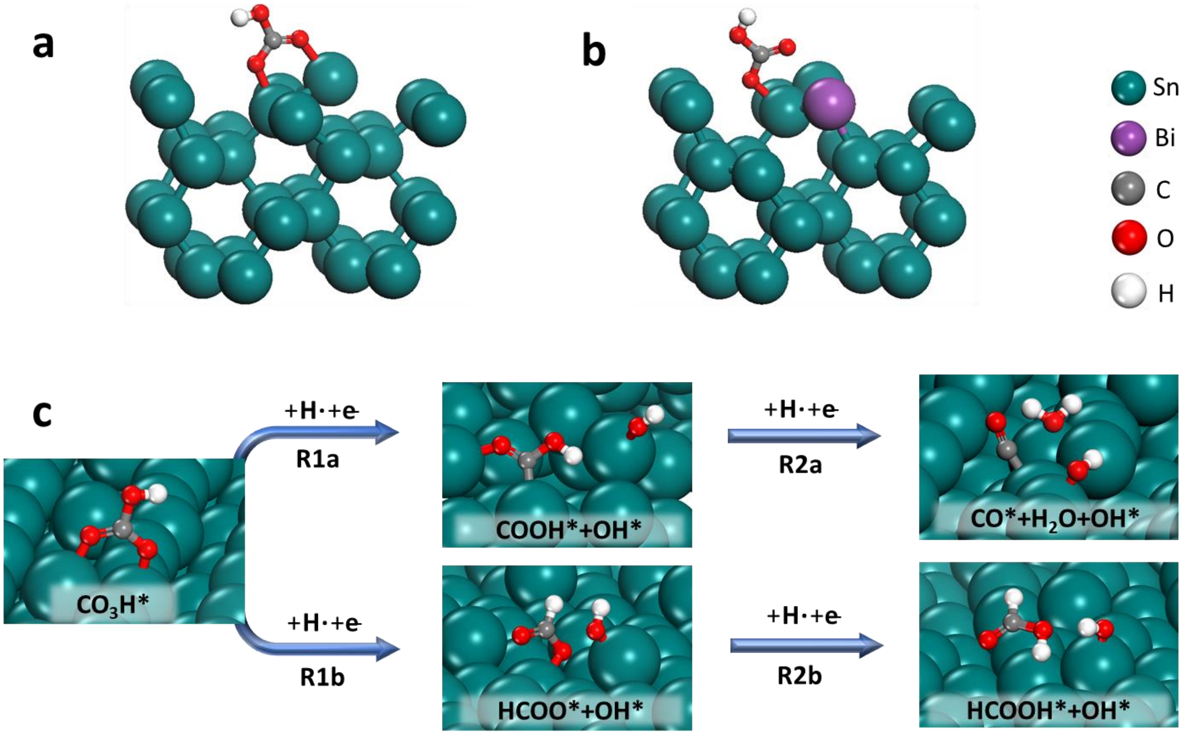

Figure S3-10. (a) Sn (101) surface with 4 layers and 2 × 2 unit cells used as the model system; (b) Bi-Sn (101) surface built by decorating one Bi atom on the surface of pure Sn (101) surface. (c) Simulation considering two pathways for CO and $HCOO^-$ production from CO_3H*.

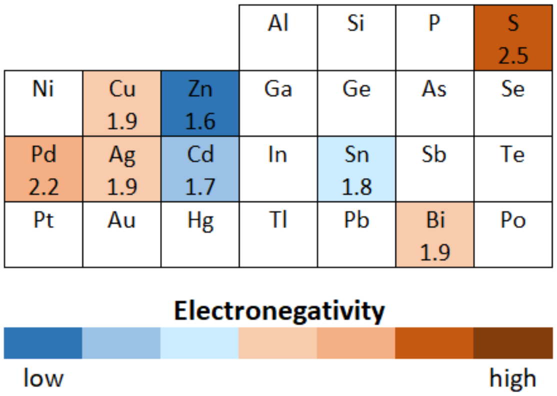

			Al	Si	P	S 2.5
Ni	Cu 1.9	Zn 1.6	Ga	Ge	As	Se
Pd 2.2	Ag 1.9	Cd 1.7	In	Sn 1.8	Sb	Te
Pt	Au	Hg	Tl	Pb	Bi 1.9	Po

Figure S3-11. Electronegativity of selected elements.[181]

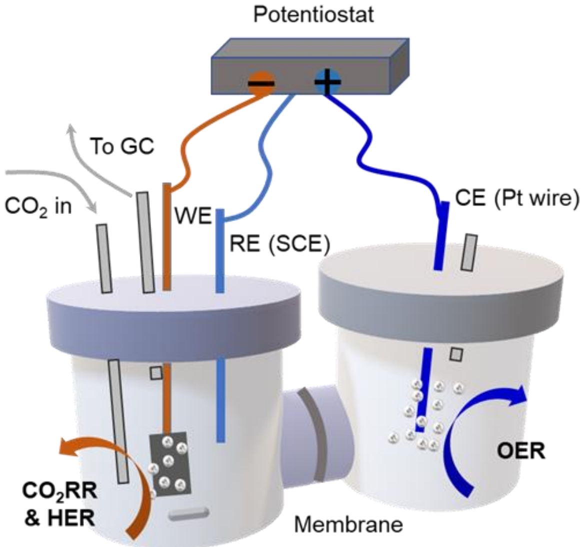

Figure S3-12. Schematic illustration of the electrochemical cell used for CO_2RR.

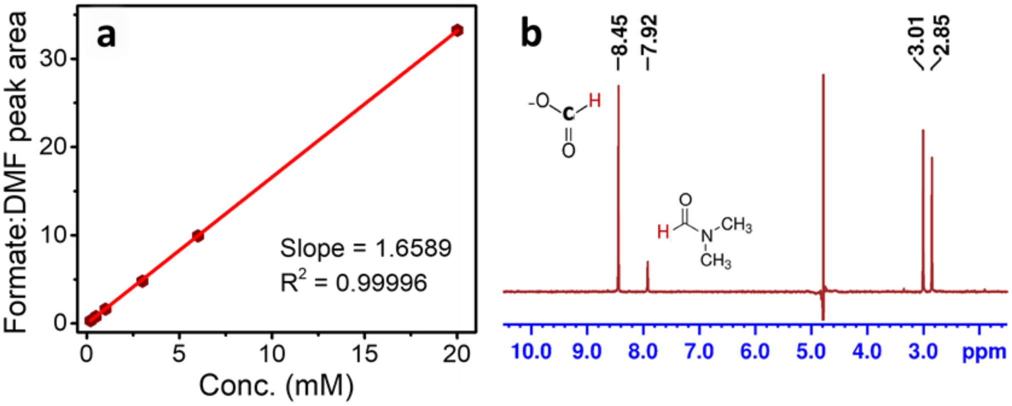

Figure S3-13. (a) A linear relationship between the formate concentration and relative peak area vs. DMF. The linear correlation coefficient is 0.99996. (b) NMR spectrum of 0.5 M $KHCO_3$ electrolyte after 1 h of CO_2RR.

Table S3-1. CO_2RR properties of electrocatalysts for formate production.

	Electrocatalysts	Electrolyte	Potential (V_{RHE})	$FE_{formate}$	Current Density (per geometric surface area)	Durability	Ref.
Sn-based	Bi-Sn / CF	0.5 M $KHCO_3$	-1.14	96%	45 mA cm^{-2}	100 h	This work
	Sn / CF	0.5 M $KHCO_3$	-1.14	80%	23 mA cm^{-2}	-	This work
	Pd-Sn nanoparticles	0.5 M $KHCO_3$	-0.43	99%	30 mA cm^{-2}	5 h	[76]
	Ag_3Sn Core−Shell Structure	0.5 M $NaHCO_3$	-0.9	87%	20 mA cm^{-2}	25 h	[50]
	Ag-Sn/rGO catalyst	0.5 M $NaHCO_3$	-0.94	88%	21 mA cm^{-2}	6 h	[166]
	Cu-Sn/rGO catalyst	0.5 M $NaHCO_3$	-0.99	87%	24 mA cm^{-2}	6 h	[166]
	Cu/SnO_2 Core−Shell Structure	0.5 M $KHCO_3$	-0.9	90%	22 mA cm^{-2}	-	[49]
	Sulfur-Modulated Tin Sites	0.1 M $KHCO_3$	-0.75	93%	55 mA cm^{-2}	40 h	[74]
	$CdSnO_3$	0.5 M $NaHCO_3$	-0.9	50%	6 mA cm^{-2}	-	[166]
	ZnSnO3	0.5 M $NaHCO_3$	-0.9	55%	3 mA cm^{-2}	-	[166]
	Graphene confined Sn quantum sheets	0.1 M $NaHCO_3$	-1.1	93%	25 mA cm^{-2}	50 h	[75]
	SnO_x/graphene	0.1 M $NaHCO_3$	-1.16	94%	10 mA cm^{-2}	-	[58]
	Sn/SnO_x thin film	0.5 M $NaHCO_3$	-0.7	40%	4 mA cm^{-2}	12 h	[32]
	Electroplated Sn/gas diffusion electrode	0.5 M $NaHCO_3$	-1.10	71%	20 mA cm^{-2}	6 h	[112]
	Electrodeposited Sn dendrite	0.1 M $KHCO_3$	-1.36	83%	25 mA cm^{-2}	18 h	[114]
	Sn modifed N-doped carbon nanofber	0.5 M $KHCO_3$	-0.8	62%	9 mA cm^{-2}	24 h	[102]

	Tin monoxide (SnO) nanoparticles	0.5 M $KHCO_3$	-0.86	75%	10 mA cm^{-2}	-	[81]
Bi-based	Bi / CF	0.5 M $KHCO_3$	-1.14	78%	53 mA cm^{-2}	-	This work
	Bi flake	0.1 M $KHCO_3$	-0.6	99%	4 mA cm^{-2}	10 h	[71]
	Bi dendrite	0.5 M $KHCO_3$	-0.74	89%	10 mA cm^{-2}	12 h	[72]
	Sulphide-derived Bi	0.5 M $NaHCO_3$	-0.75	84%	5 mA cm^{-2}	24 h	[165]
	Bi nanosheets	0.5 M $NaHCO_3$	-0.7	90%	13 mA cm^{-2}	5 h	[73]
	Ultrathin Bi nanosheets	0.5 M $NaHCO_3$	-0.9	~100%	15 mA cm^{-2}	10 h	[164]

Table S3-2. Actual compositions of the synthesized Bi(x)-Sn/CF and the amount of electron charge passed.

Calculated composition	Bi/Sn surface ratio (XPS measured composition)	Total Charge Passed/ C
Bi(0.1)-SnO_2/CF	0.1	5
Bi(0.5)-SnO_2/CF	0.13	10
Bi-SnO_2/CF	0.17	20
Bi(3)-SnO_2/CF	0.28	50
Bi(10)-SnO_2/CF	0.45	100

Note: The electrodeposition was conducted by applying -0.1 V until a desired amount of electron charge was passed to obtain the composite electrodes with different ratios of Bi and Sn.

Chapter 4. CO_2-to-CO Transformation by Sn-Ti-O Ternary Catalyst

This chapter consists of the following paper that was co-authored by myself, my supervisors, four Ph.D. students (Bohua Ren, Haozhen Dou, Zhen Zhang, and Yaping Deng), and six collaborators (Moon G. Park, Jie Yang, Zhengyu Bai, Lin Yang, Gianluigi A. Botton, and Yongfeng Hu). Reproduced with permission from "Ternary Sn-Ti-O Electrocatalyst Boosts the Stability and Energy Efficiency of CO_2 Reduction", ***Angew. Chem. Int. Edit.*** **2020**, 59, 12860." Copyright 2020 Wiley-VCH Verlag GmbH & Co. KGaA. DOI: org/10.1002/anie.202004149. *Featured on Cover.*

Statement of Contributions: I devised the idea, synthesized the materials, and carried out the electrochemical measurements; B. Ren conducted DFT simulation and analyses; M. Park and H. Dou contributed to the materials' synthesis and characterization; J. Yang and G. Botton carried out TEM experiments; Z. Bai and Z. Zhang contributed to electrochemical experiments and data analyses; Y. Deng and Y. Hu performed XAFS experiments; J. Gostick and I developed the FEM model; Z. Chen supervised the research work; G. Wen, B. Ren, Z. Bai, and Z. Chen wrote the manuscript. All authors participated in the discussion and commented on the results.

4.1. Introduction

The conversion of CO_2 to valuable chemicals via electrochemical CO_2 reduction reactions (CO_2RR) offers a clean and sustainable approach toward closing the carbon loop.[7, 9, 193] The CO_2RR process also allows for harvesting intermittent renewable energy sources such as wind and solar.[79] Among a variety of derived chemicals, carbon monoxide (CO) and formic acid are of great interest due to their relatively lower activation potentials and their large potential market (CO for synthetic gas and formic acid for hydrogen carrier).[50, 194-195] To seek efficient electrocatalytic materials, many strategies have been explored extensively, including, but not limited to, engineering morphology,[164, 196-197] exploration of the binary-metal hybrid effect,[48-49, 166, 198-199] tuning oxidation states,[81, 200] and synthesizing single-atom catalysts.[158, 201-202] However, there are still technical challenges that hinder the commercial scaling-up of CO_2RR processes, such as limited EE (generally lower than 60%), shorter operating lifetime (generally lower than 100 hours), and difficult separation of end products.

Tin (Sn) and partially oxidized SnO_x based materials are one of the most promising non-precious materials for practical CO_2RR systems,[2, 75] being able to convert CO_2 to both CO and formic acid (**Table S4-1**).[49, 81] Noticeably, oxygen (O) atoms in SnO_x play an important role in the adsorption of intermediates.[82-83] Nevertheless, the energy efficiency (EE) of CO_2RR is typically limited by a low selectivity of the desired product, a large overpotential (> 0.8 V), and a narrow potential window.[80] Additionally, the introduction of O atoms also causes catalysts to become unstable due to the competition between metal oxide reduction and CO_2RR under highly cathodic conditions.[84]

Herein, I proposed to decorate Sn with titanium (Ti) and construct a 3D ordered mesoporous (3DOM) structure to overcome existing limitations of CO_2RR. First, the addition of Ti atoms is revealed to preferably adsorb the oxygen atom in the COOH* intermediate, tuning the selectivity toward CO instead of formate. Second, Ti atoms are further unearthed to stabilize the lattice oxygen atoms in SnO_x and maintain the 3DOM structure, prolonging the catalyst lifetime. Third, the robust 3DOM structure results in a local environment with higher alkalinity, not only suppressing the hydrogen evolution reaction (HER) but also further hindering formate formation. Finally, the decorative Ti atoms and the high local alkaline environment are experimentally proven to reduce CO_2 activation potential and expand the potential window. Therefore, the work offers a new 3DOM ternary Sn-Ti-O electrocatalyst that can efficiently convert CO_2 to CO at high cathodic energetic efficiency (EE_{ca}) for extended periods, advancing Sn-based catalytic materials for scaling-up and practical applications of CO_2RR.

4.2. Results and Discussion

Density functional theory (DFT) analyses were performed to examine the atomic interactions in the Sn-Ti-O metal−oxide interface. SnO_x is reported to have good activity for CO_2RR.[50, 86, 203] While TiO_2 plays an important role to maintain the structure. The samples with lower ratios of Ti (<0.7) cannot construct a stable 3DOM structure and a pure TiO_2 sample is inactive for CO_2RR (Electrochemical Performance section). Consequently, two Models were considered in DFT simulation to consider the effect of Ti on the active SnO_x site. Model I was generated (i.e. SnO_2 with 6 oxygen vacancies, $SnO_{2-\delta}$)[204] owing to the fact that the surface tin oxide layer can be partially reduced under reaction conditions.[50] Model II was built as Model I with three Ti atoms substituting Sn on the surface (i.e. $Sn(Ti)O_{2-\delta}$) in order to investigate the influence of Ti on active $SnO_{2-\delta}$ site. Model II in DFT analyses was used as a representation of the local atomic structure of active sites.[48, 204] Two main pathways for CO and formic acid (HCOOH) production were considered on two models (**Figure S4-1a-c** in the 4.5. Supporting Information).[84, 86, 201]

Table 4-1. Calculated average Bader charge (e) of surface Ti atoms and neighboring Sn and O atoms in Model I and II, respectively.

Atom[a]	Surface Models		Variation (Δ_{II-I})
	Model I: $SnO_{2-\delta}$	Model II: $Sn(Ti)O_{2-\delta}$	
O (av)	-1.063	-1.061	+0.002
Sn (av)	+1.390	+0.843	-0.547
Ti (av)	-	+1.745	-

[a] O (av) and Sn (av) entries indicate the average (av) charges of three oxygen atoms and three Tin atoms, respectively, located at the nearest neighboring sites of Ti.

From Bader charge analysis (**Table 4-1**), we found that the surface Sn atoms near Ti atoms possess a formal charge variation of -0.547 e, while O atoms near Ti atoms retain its valence state (+0.002

e variation). This infers that Ti tends to delocalize charge by releasing it to the Sn atom (**Figure 4-1d**). The projected density of states (PDOS) of the surface Sn and Ti atoms was further analyzed in **Figure 4-1c-e**. The substitution of Ti atoms causes the s, p, and d band centers of surface Sn atoms to downshift by over 2.3 eV (**Table S4-2**).[205] The electron density transfer from Ti to Sn has two important impacts:

(I) In favor of CO production (shortened reaction pathway). The marked downshift of the band centers indicates that the antibonding states are filled with more electrons. The back-donation antibonding states, therefore, decrease (**Figure 4-1e**).[95, 206-207] Specifically, the back-donation from the valence band of Sn to the unoccupied orbital of COOH* is reduced,[95] weakening the Sn-C bond. On the other hand, Ti atoms are depleted of electron density and further possess enhanced O affinity, seeking to bond with the oxygen atom of COOH*.[208] The corresponding effects - the breaking of C-O bond and weakening of Sn-C bond during the adsorption process - both benefit the dissociative adsorption of COOH* intermediate, as illustrated in **Figure 4-1d**. These results additionally reveal the change in the catalytic mechanism associated with Ti substitution. As depicted in **Figure 4-1a**, the intermediate COOH*, which is derived from CO_3H* and deemed as the main intermediate of CO formation, bonds on the $SnO_{2-\delta}$ surface (Model I) through a carbon atom (**Figure 4-1a**). Upon further transfer of H^+ from the electrolyte, COOH* dissociates into CO* and OH* with a reaction energy of -2.96 eV (**Table 4-2**). However, for the Sn-Ti-O system, COOH* dissociative adsorption takes place on the $Sn(Ti)O_{2-\delta}$ surface (Model II), leading to direct CO* formation (**Figure 4-1b**). This transforms CO* formation from a two-step reaction (CO3H* →COOH* → CO*) to a one-step reaction (CO_3H* → CO*), which facilitates CO* production. (**Figure S4-1d** and **e**).

Table 4-2. Calculated reaction energies (ΔE) of Model I and II.

Reactions	Surface Models	
	Model I: $SnO_{2-\delta}$	Model II: $Sn(Ti)O_{2-\delta}$
$COOH^* + OH^* + H^+ + e^- + * \rightarrow CO^* + H_2O^* + OH^*$	-2.96 eV	-3.33 eV[a]
$HCOO^* + OH^* + H^+ + e^- \rightarrow HCOOH^* + OH^*$	-3.59 eV	-2.49 eV

[a] the reaction energy for CO* formation step is calculated by using $E(CO^*+2OH^*)-E(CO_3H^*+H^+)$ due to dissociative adsorption of COOH* for Model II (**Figure S4-1**).

(II) Suppression of HCOOH production (higher reaction energy): For Model I (pure $SnO_{2-\delta}$), HCOO* is adsorbed on the surface by forming Sn-O bond. However, for Model II ($Sn(Ti)O_{2-\delta}$), HCOO* tends to adsorb by forming Ti-O bond instead (**Figure 4-1f**). The Ti atoms introduced in the pure $SnO_{2-\delta}$ system interacts with neighboring Sn atoms. As shown in **Figure 4-1f**, Sn atoms deplete Ti atoms of electron density. Consequently, Ti atoms further possess enhanced O affinity, which indicates that Ti-O bond is stronger than Sn-O bond. This is also supported by the stronger adsorption of HCOO* on Model II. As indicated by the definition of adsorption energy (E_{ads}) in the Supporting Information, a more negative value of E_{ads} means stronger adsorption. As shown in **Table S4-3**, E_{ads} of HCOO* on Model II is -3.11 eV, while E_{ads} is -2.20 eV on Model I. The much higher adsorption strength (more negative) makes HCOO* intermediate overly stabilized, making it more difficult to break the Ti-O bond and produce HCOOH*, as shown in **Figure S4-1b**. In addition, the higher adsorption energy of HCOOH* on Model II, as shown in **Table S4-3**, leads to unfavorable desorption. The above reasons justify the higher reaction energy for HCOOH* production in Model II than Model I, causing suppression of HCOOH* in Model II. Accordingly (**Table S4-4**), the variation in reaction energies indicate that CO formation is more spontaneous and the formation of HCOOH is suppressed for Model II.

As disclosed by DFT calculations, with appropriate construction of ternary Sn-Ti-O catalysts, Ti atoms tend to delocalize charge by releasing it to the Sn atoms. This may explain why selectivity is shifted towards CO rather than formate.

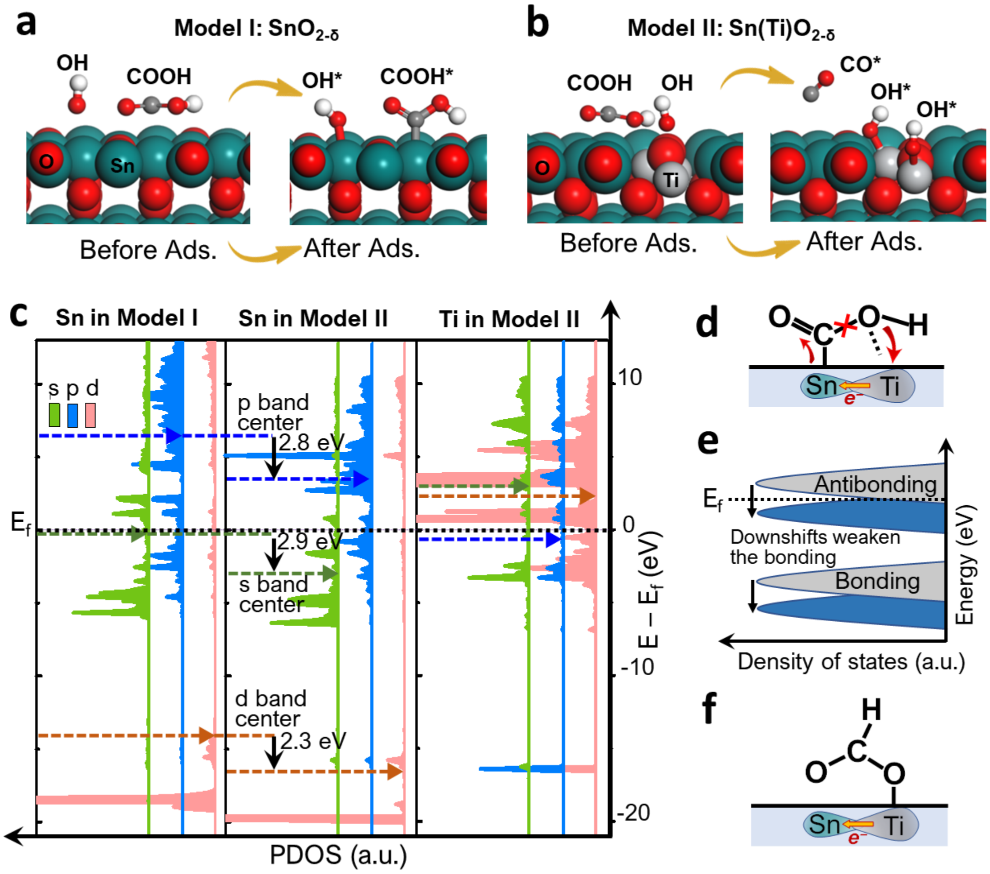

Figure 4-1. DFT simulations. (a) COOH and OH species on the surface of Model I before and after adsorption (Ads.). (b) COOH* dissociative adsorption on Model II. (c) PDOS of s, p, and d orbitals of Sn and Ti atoms on Model I and Model II. Dashed lines indicate the orbital band centers and Fermi energy level. (d) Schematic of COOH* dissociative adsorption on the Sn-Ti surface. (e) Approximate schematic of antibonding and bonding states between the reaction surface and the adsorbate before (gray) and after (blue) Ti substitution. (f) Schematic of HCOO* adsorption on the Sn-Ti surface.

In light of Sn-Ti interactions and previously reported superiority of mesoporous structure,[209-210] we sought to produce 3DOM ternary Sn-Ti-O compounds, which were prepared according to our previous work.[211-212] A series of ternary Sn-Ti-O catalysts with varying surface ratios of Sn-Ti were synthesized and characterized: $Sn_{0.1}Ti_{0.9}O_2$, $Sn_{0.2}Ti_{0.8}O_2$, $Sn_{0.3}Ti_{0.7}O_2$, $Sn_{0.4}Ti_{0.6}O_2$, $Sn_{0.6}Ti_{0.4}O_2$, $Sn_{0.8}Ti_{0.2}O_2$ (**Table S4-5**). Among these, the $Sn_{0.3}Ti_{0.7}O_2$ catalyst had the best selectivity for CO formation as discussed in the later Electrochemical Performance section.

The produced ternary Sn-Ti-O materials were characterized using scanning electron microscopy (SEM) and observed an evident honeycomb porous structure, as shown in **Figure 4-2a** and **Figure S4-2**. The structure exhibited consistent pores with a diameter of approximately 100 nm, (**Figure 4-2b**) providing strong structural support and high surface area with many available sites for catalytic activity. Interestingly, only for certain Sn-Ti-O ratios ($Sn_{0.2}Ti_{0.8}O_2$ and $Sn_{0.3}Ti_{0.7}O_2$, **Figure S4-3** and **S4-4**), there were 5 nm nanoparticles attached to the 3DOM framework (**Scheme 4-1** and **Figure 4-2b** inset).

Figure 4-2c depicts a compositional line scan on the edge of the porous structure of 3DOM $Sn_{0.3}Ti_{0.7}O_2$ material, showing the composition of Sn, Ti, and O elements. As further shown in **Figure 4-2d** and **S4-3**, the chemical compositional maps with Electron Energy Loss Spectroscopy (EELS) were obtained over the region shown within the green box. The results showed a 3DOM framework with adherent nanoparticles composed of SnO_x with dispersed amorphous/ crystallographic (anatase) TiO_2 in $Sn_{0.3}Ti_{0.7}O_2$ material (**Scheme 4-1**). High-resolution TEM (HRTEM) was performed on the 3DOM structure, which showed a d-spacing corresponding to the (110) and (101) planes of SnO_2 and the (211) and (105) planes of anatase TiO_2 and amorphous layer (**Figure 4-2e**). The same conclusions were derived from the compositional line scan, chemical compositional maps, and HRTEM of $Sn_{0.2}Ti_{0.8}O_2$ material which are provided in **Figure S4-4**.

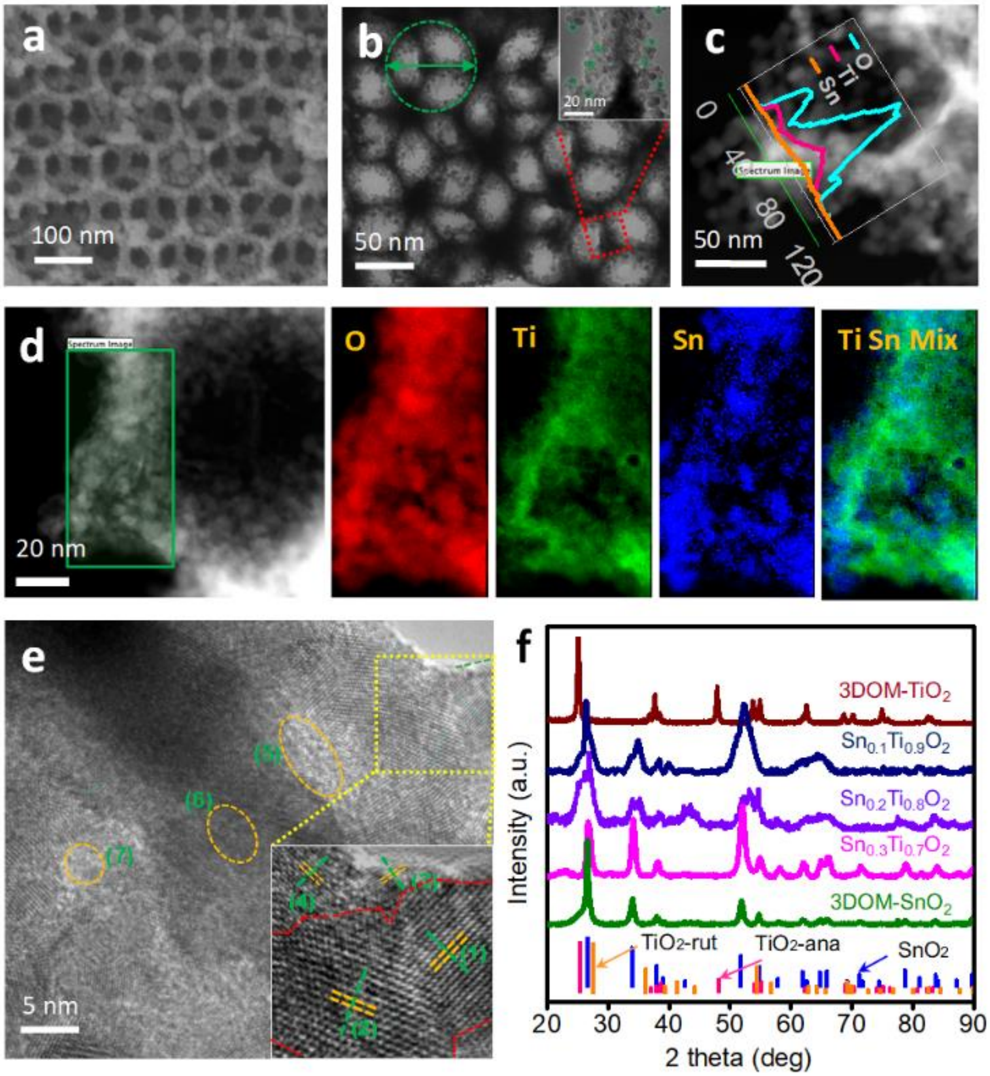

Figure 4-2. Material characterizations. (a) SEM images, (b) TEM images, and (c) Line scan from EELS spectra on the edge of 3DOM-$Sn_{0.3}Ti_{0.7}O_2$ material. (d) Elemental mapping from EELS spectra of O (red), Ti (green) and Sn (blue) atoms. (e) HRTEM image of $Sn_{0.3}Ti_{0.7}O_2$ material. (1) 0.261nm, SnO_2(101); (2) 0.330nm, SnO_2 (110); (3) 0.167nm, anatase TiO_2 (211); (4) 0.170 nm, anatase TiO_2 (105); (5-7) amorphous layer; Red dash line highlights the interface between SnO_x and TiO_2. (f) XRD patterns of 3DOM-TiO_2, $Sn_{0.1}Ti_{0.9}O_2$, $Sn_{0.2}Ti_{0.8}O_2$, $Sn_{0.3}Ti_{0.7}O_2$ and 3DOM-SnO_2 electrodes. SnO_2: JCPDS 41-1445; TiO_2 in anatase phase: JCPDS 21-1272; TiO_2 in rutile phase: JCPDS 78-1510.

Hierarchically ordered and interconnected mesoporous structure of synthesized Sn-Ti-O materials were found to feature a type IV N_2 adsorption-desorption isotherm,[211-212] as shown in **Figure S4-5**. Particularly, $Sn_{0.3}Ti_{0.7}O_2$ material showed Brunauer-Emmet-Teller (BET) specific surface area of 39.9 m^2 g^{-1} and a less broad pore size distribution. This special structure appears to achieve an ideal balance between exposure of active sites (more Sn-Ti-O interface) and appropriate electron density shift to enable Sn-Ti-O ternary synergistic effect and display optimum CO_2RR performance as depicted by electrochemical tests, to be discussed later. The formation of such special structures, with nanoparticles attached to the surface of 3DOM framework, can be ascribed to the selective surface migration, phase separation and oxidation of the metals during calcination.[213]

Due to the nature of sample fabrication (co-precipitation and calcination at 600 ^{o}C), it is possible to thermodynamically observe the formation of Sn-Ti intermetallic as well as mixed-oxide phases as indicated in the phase diagrams (**Figure S4-6 a, b**). The X-ray diffraction (XRD) technique has deep penetration and provides a glimpse of the material compositions. As depicted from XRD patterns (**Figure 4-2f**, **S4-7a**), the special $Sn_{0.3}Ti_{0.7}O_2$ composition displayed a major SnO_2 phase. However, as shown in **Figure 4-2c-e** (Line scan from EELS spectra; Elemental mapping; HRTEM images), there were still coexisting amorphous and anatase TiO_2 phases presumably near the surface of the 3DOM framework. Due to TiO_2 being mainly amorphous and the limited amount of anatase TiO_2, the peaks of SnO_2 dominated and TiO_2 peaks could not be observed in the XRD patterns.

For the higher Sn-Ti ratios ($Sn_{0.8-0.4}Ti_{0.2-0.6}O_2$), XRD patterns still clearly revealed only peaks of $SnO_{2,}$ and the Ti atoms likely existed as poorly crystalline oxides. Although the pure SnO_2 sample formed an extensive 3DOM structure, with low additions of TiO_2, the SnO_2 phase tended to congregate and formed nanoparticles with the influence of Ti additions, thereby interrupting the framework, as shown in **Figure S4-8**. From TEM images (**Figure S4-9**), the 3DOM formation became more stable for $Sn_{0.4}Ti_{0.6}O_{2,}$ suggesting higher additions of TiO_2 eventually stabilize the structure.

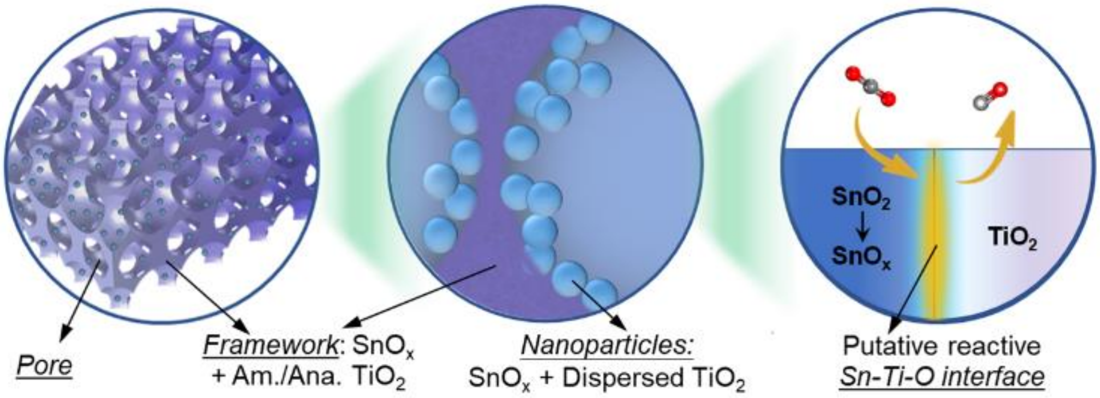

Scheme 4- 1. Schematic of the 3DOM ternary $Sn_{0.3}Ti_{0.7}O_2$ electrocatalyst and local putative reactive Sn-Ti-O interface. (Am. indicates amorphous and Ana. indicates anatase.)

On the other hand, for a lower Sn-Ti ratio ($Sn_{0.2}Ti_{0.8}O_2$, $Sn_{0.1}Ti_{0.9}O_2$), there was evidence of peak broadening and peak shoulder/separation at around 27°, 35°, and 51° in the XRD patterns (**Figure S4-7a**) presumed to correspond to the spinodal decomposition region (**Figure S4-6a**), displaying a more defined coexistence of SnO_2 and anatase TiO_2 phases. In this case, the formation of TiO_2 rich regions caused the shifting and transition of SnO_2 peaks towards TiO_2 anatase. At 100 mol% TiO_2 composition, the phase diagram predicts a rutile phase.[214] Interestingly, our 3DOM structure appeared as anatase, which has higher catalytic activity than the rutile phase.[215] Considering the differences between nano-material and bulk material solidification, the deviation from the phase diagram is understandable. The 3DOM nanostructure presents itself with larger solubility range and formation of anatase rather than rutile due to: (1) the extra energy applied during the sonication procedure, (2) possibility of liquid and solid phase coexistence in small dimensions,[216] and (3) more Ti accommodation due to atomic segregation towards the surface which avoids nucleation of another phase.[214] The special Sn-Ti ratio ($Sn_{0.3}Ti_{0.7}O_2$) is most likely the crucial turning point for spinodal decomposition for the nano-binary materials (**Figure S4-6c**). $Sn_{0.3}Ti_{0.7}O_2$ not only avoided complete spinodal decomposition, presenting mainly the SnO_2 phase with minor amorphous/ anatase TiO_2 phase but also maintained a stable 3DOM structure.

As we previously disclosed,[86] the Sn-based catalysts need to undergo accelerated degradation and activation under -1.13 V vs. RHE before performing CO_2RR.[50] The emergence of Sn peaks was found for the electrodes with Sn-Ti ratios higher than 3:7 after the in-situ activation step (**Figure S4-7**). After the activation step, notably, the SnO_2 peaks were still conserved for $Sn_{0.3}Ti_{0.7}O_2$ electrodes, while there were no remaining strong SnO_2 peaks for the 3DOM SnO_2 electrode after activation. Further, for lower Sn-Ti ratios ($Sn_{0.1}Ti_{0.9}O_2$ and $Sn_{0.2}Ti_{0.8}O_2$), the oxide-to-metal phase exchange (i.e. reduction of SnO_2 to Sn) was not noticeable from XRD analysis. This resistance to phase change is understood to be due to the oxygen atoms being much more stable in Sn-Ti-O ternary structure during CO_2RR.

To explore the complex interactions and the electronic structure between Sn, Ti, and O atoms, the calculated charge density reconfiguration is disclosed in **Figure 4-3a** and shows that the charge density is accumulated around O and Sn atoms, while depleted around Ti atoms.[200, 217-218] To further verify the electron density configuration of Ti in the catalysts, X-ray absorption near-edge spectroscopy (XANES) at the Ti K-edge was performed to illustrate the coordination environments of Ti in different cases. Three characteristic features are denoted A1, A2' and A3 in the pre-edge structure of the Ti K-edge spectra of compounds with high structural symmetry, such as six-coordinated anatase (**Figure 4-3b**).[219-220] For all Sn-Ti-O materials, A1and A3 signals were weak; only a pronounced A2 peak was perceived instead, indicating the existence of less symmetric Ti atoms predominately on the surface of the oxides.[221-222] The low-coordination nature of Ti is also supported by the amorphous structure of TiO_2 as depicted by XRD patterns (i.e. no clear discrete diffraction peaks associated with anatase TiO_2, **Figure S4**-7), HRTEM (**Figure 4-2e**), and extended X-ray absorption fine structure (EXAFS) spectra of Ti K-edge (where lower EXAFS amplitude is observed for Sn-Ti-O samples as shown in **Figure S4-10a, b**). For the Ti atom in

$Sn_{0.1}Ti_{0.9}O_2$, it showed the highest intensity for A2 peak with negligible A1 peak, suggesting its Ti coordination was more similar to four-coordinate TiO_2.[222] On the other hand, the Ti atoms in $Sn_{0.3}Ti_{0.7}O_2$ had the lowest pre-edge peak area with more defined A1, A2, and A3 peaks (inset of **Figure 4-3b**). This indicates that Ti in $Sn_{0.3}Ti_{0.7}O_2$ specifically had a more distorted symmetry,[222] due to the strongest interaction between Ti 3d and Sn/O (2p), and electron density reconfiguration.

Sn-L_3 edge XANES spectra (**Figure S4-10c**) further confirmed Sn atoms in $Sn_{0.3}Ti_{0.7}O_2$ exhibited an oxidation state between the Sn^{2+} and Sn^{4+} state.[74] In summary, the interaction between Sn and Ti atoms exists as an amorphous structure with partial electron density reconfiguration among Sn, Ti, and O according to the XRD (**Figure S4-7**), XPS (**Figure S4-11**) and Ti K-edge and Sn-L_3 edge XANES spectra (**Figure 4-3** and **Figure S4-10c**). Additionally, our simulated XANES spectra[223-226] using DFT Model II (**Figure S4-10d**) is consistent with the experimental measurements, which indicates the DFT surface model is valid to depict the interaction of local Sn-Ti-O interface.

XPS analysis was performed to further prove the oxide states in ternary Sn-Ti-O catalysts (**Figure 4-3c-e** and **Figure S4-11a-c**). Both Ti and Sn in the matrix were present in their oxide states (Sn^{4+} and Ti^{4+}, respectively). **Figures 4-3c** shows the obvious shifts of O 1s with different ratios of Sn-Ti. These shifts resulted from interactions between O, Sn, and Ti atoms. With increasing Sn-Ti ratio, the O 1s and Ti 2p binding energies shifted higher, while all Sn 3d peaks of Sn-Ti-O materials shifted to lower binding energy compared with the 3DOM-SnO_2, with the shift of $Sn_{0.3}Ti_{0.7}O_2$ being the largest. This indicates the strongest interaction between Ti and Sn/O was experienced within $Sn_{0.3}Ti_{0.7}O_2$, as the maximum electron density was accumulated around Sn atoms, and the most depletion of electron density occurred for Ti 2p.[181, 227-230] These shifts are attributed to a partial electron density reconfiguration among Sn, Ti, and O (**Figure S4-11g**), which also corresponds with the Ti K-edge XANES and DFT analyses.

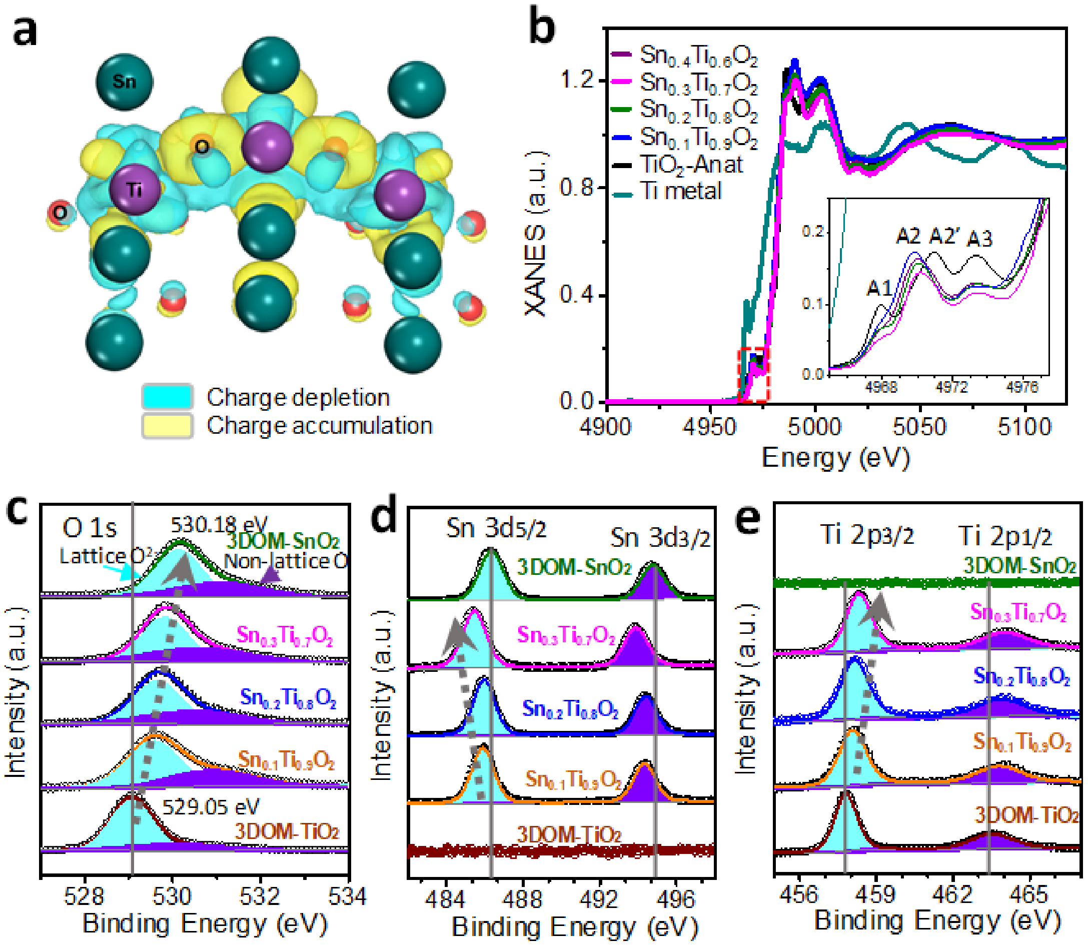

Figure 4-3. Electron density transfer among Sn, Ti, and O atoms. (a) Scheme of calculated charge densities. The yellow and cyan blue isosurfaces correspond to the increase in the number of electrons and the depletion zone, respectively. (b) XANES spectra of Ti K-edge; the red area highlights the near-edge absorption energy. (c) O 1s, (d) Ti 2p and (e) Sn 3d core-level XPS spectra of 3DOM-TiO_2, $Sn_{0.1}Ti_{0.9}O_2$, $Sn_{0.2}Ti_{0.8}O_2$, $Sn_{0.3}Ti_{0.7}O_2$ and 3DOM-SnO_2 materials.

From the comparison of XPS spectra before and after the activation step (**Figure S4-11d-f**), the activation step resulted in a high number of oxygen defect sites (531.0 eV) with a low oxygen coordination[231-232] and the presence of $Sn^{2+/4+}$ (485.9 and 494.4 eV) and Sn^0 (484.0 and 492.5 eV) on the $Sn_{0.3}Ti_{0.7}O_2$ catalyst surface. To further consider the effect caused by metallic Sn atoms, we added a new DFT Sn_5-Sn(Ti)O_2 model (Model III), as shown in **Figure S4-12**, which contains an Sn_5 cluster – the most stable configuration containing 5 Sn atoms[233] – mounted on the Sn(Ti)O_2 surface. Sn_5-Sn(Ti)O_2 model indicated the preferential formation of formate over CO. This outcome contradicts experimental results, and it is concluded that this model configuration is unlikely the active site for CO_2-to-CO reduction. Only by appropriate construction of ternary Sn-Ti-O catalysts ($Sn_{0.3}Ti_{0.7}O_2$), one appears to achieve a balance between exposure of active sites and an appropriate electron density shift. It was demonstrated that Ti atoms tended to delocalize maximum charge by releasing it to the Sn atoms in the compositions of $Sn_{0.3}Ti_{0.7}O_2$, which altered the selectivity between CO and formate. Though the main cause of charge delocalization is electronegativity difference between Sn, Ti, and O, other factors can also play a role, such as a synthesis method, composition, and contact interface.

The CO_2RR activities of ternary Sn-Ti-O electrodes were investigated in an H-type electrochemical cell separated by a Nafion membrane with CO_2-saturated 0.5 M $KHCO_3$ as the electrolyte (methods in Supporting Information).[86] In this work, the potentials reported are all converted into RHE. Linear sweep voltammetry (LSV) was performed firstly in the CO_2-purged and N_2-purged electrolyte (**Figure S4-13a, b**), which showed the catalysts induce higher currents in the CO_2- saturated solution. Then the constant potential electrolysis (CPE) tests for 2 hours and repeated three times; the results presented are the averaged values under a sequence of potentials (**Figure S4-13c**). H_2, CO, and formate were the only products detected by gas chromatography (GC) and 1H- Nuclear Magnetic Resonance (NMR) spectrometer, respectively, and overall Faradaic efficiency (FE) of approximately 100% was achieved (**Table S4-6**, **Figure S4-14**). As depicted in **Figure 4-4a**, $Sn_{0.3}Ti_{0.7}O_2$ electrode showed a noticeable FE(CO), reaching 92% ± 2.5% at a low potential of around -0.54 V vs. RHE (430 mV overpotential). The cathodic energy conversion efficiency is projected to reach 71.5 % (methods in Supporting Information), which surpasses most Sn-based catalysts (**Table S4-1**) and satisfies the basic requirement for electrosynthesis to compete with fossil fuel-derived feedstocks.[79] Meanwhile, the remarkable CO selectivity (above 90%) was maintained over a wide potential window, from -0.54 V to -0.94 V, as highlighted in light blue in **Figure 4-4a**. It is deemed that a wide potential window is essential for scaling the CO_2RR process into practical and grid-scale applications,[95] and will enhance the robustness and stability during inherent potential fluctuations inherent in electrolysis.

Comparing the entire series of produced 3DOM catalysts toward CO formation (**Figure 4-4b**), 3DOM TiO_2 had nearly zero FE(CO), while FE(CO) on the 3DOM-SnO_2 reached a maximum of about 50% at -0.34 V and decreased with more negative potential. From the studied 3DOM ternary Sn-Ti-O catalysts, $Sn_{0.3}Ti_{0.7}O_2$ obtained an optimum selectivity for CO, which is a more desirable product than formate in terms of separation and broader use.[81]

As depicted in **Figure 4-4c**, the optimal current density was achieved by $Sn_{0.3}Ti_{0.7}O_2$ and also demonstrated superiority over reported results (**Table S4-1**). Especially compared with the SnO_2 nanosheets[86] we previously reported, 3DOM-SnO_2 exhibited a slightly lower formate selectivity (65% FE($HCOO^-$) for 3DOM-SnO_2 vs. 77% for SnO_2 nanosheets) and competitively higher CO selectivity (32% FE(CO) for 3DOM-SnO_2 vs. 18% for SnO_2 nanosheets) at its optimum potential of -1.03 V. The observed differences in selectivity is attributed to the high local alkalinity provided by the mesopores, as shown in the **Figure 4-4e**. From the finite element method (FEM) modeling, the local pH value was determined to theoretically reach up to 9.2 in the pores of 3DOM.

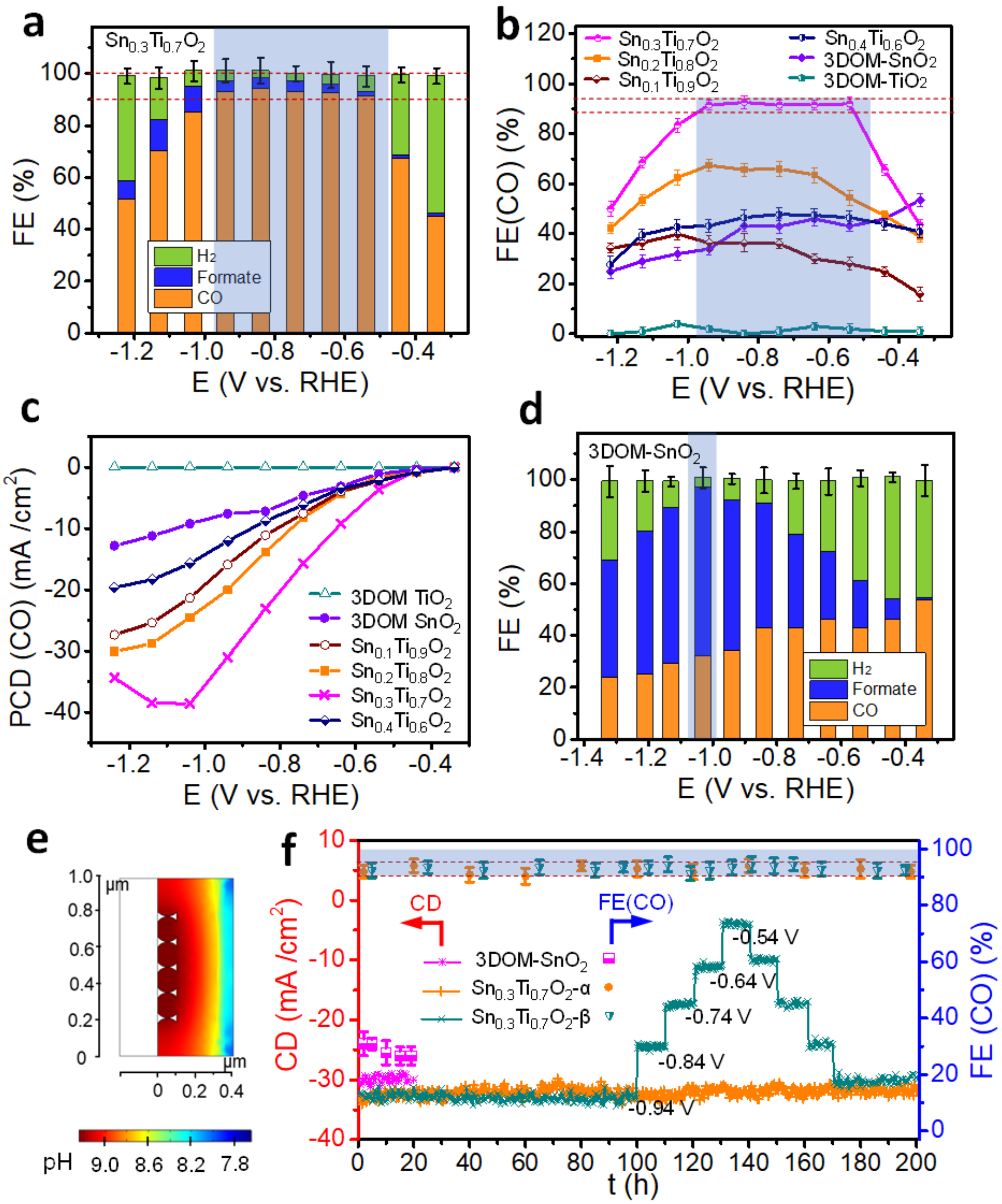

Figure 4-4. CO_2RR performances. (a) FE toward CO, formate, and H_2 on $Sn_{0.3}Ti_{0.7}O_2$ electrode at a series of potentials from −0.34 to −1.21 V. (b) FE and (c) Partial current density (PCD) of CO on 3DOM-TiO_2, $Sn_{0.1}Ti_{0.9}O_2$, $Sn_{0.2}Ti_{0.8}O_2$, $Sn_{0.3}Ti_{0.7}O_2$, $Sn_{0.4}Ti_{0.6}O_2$, and 3DOM-SnO_2 electrodes under different potentials. (d) FE toward CO, formate, and H_2 on the 3DOM-SnO_2 electrode. (e) Calculated pH values in the mesopores via FEM simulations. (f) Stability test for 3DOM-SnO_2 and $Sn_{0.3}Ti_{0.7}O_2$ measuring current density (line plot) and FE (scatter plot). Test α (orange curve) of $Sn_{0.3}Ti_{0.7}O_2$ is continuous electrolysis at -0.94 V, while Test β (green curve) is altering the potentials during electrolysis. The error bars represent the standard deviations of three independent measurements of the same sample.

Our FEM calculation results further validate the ability of our mesoporous structure to increase CO selectivity, by not only suppressing the HER,[234-235] but also hindering formate formation. The bicarbonate electrolyte has low buffer capacity with limited migration rates of ionic species.[236] It results in two consequences: 1) limited hydroxide ions migration rates and increased local alkalinity restrict the availability of protons in the mesopores, which inhibits the HER activity;[1c, 31b, 32] 2) limited formate ions migration rates and increased formate ions concentration in the mesopores (**Figure S4-15**) further hinder formate formation. Additionally, a highly alkaline region is also beneficial for the catalytic activation of CO_2 in the electrolyte.[80, 93] The authors acknowledge that intentionally creating a high alkaline environment with the use of KOH electrolyte in the H-Type cell experiment would directly demonstrate these favorable effects. However, KOH participates in a side reaction that consumes CO_2 and decreases the available CO_2 concentration around the electrodes needed for the reduction reaction.[89] For example, researchers have previously proposed to use alkaline flow cells with a gas diffusion electrode (GDE) operated in a flow-by mode.[88, 237-238] It can provide higher current densities (CD) and energy efficiencies. However, it was also shown to suffer from carbonate salt precipitation in the stagnant pores of the GDE. Moreover, CO_2 is parasitically converted to bicarbonate in the KOH electrolyte. Noticeably, the high local alkalinity in our engineered mesopores remained confined and appeared to be unaffected by the strong stirring turbulence in the experimental setup. It was therefore able to maintain CO_2 availability, which is an impressive feature for CO_2RR.

Although the 3DOM SnO_2 showed improved CO selectivity relative to the nanosheets, 3DOM SnO_2 was not stable and only had stability for around 20 hours. Afterward, the FE(CO) was suddenly reduced and the porous structure collapsed (**Figure S4-16**). Remarkably, the produced optimum $Sn_{0.3}Ti_{0.7}O_2$ electrode had good stability of over 200 hours of continuous electrolysis (orange Curve α in **Figure 4-4f**) without any obvious degradation confirmed by LSV curves and XRD, XANES and EXAFS analyses (**Figure S4-16 e, f,** and **S4-17**). SEM image (**Figure S4-16**) displayed the collapse of the porous morphology, which is likely attributed to further reduction of SnO_x and the removal of oxygen atoms from the crystal lattice, as proven by XPS spectra (**Figure S4-18**). To maintain a constant ionic concentration in the electrolyte during prolonged testing, the electrolyte was replaced with a fresh solution every 20 hours and the recorded time step was set to 30 mins. To demonstrate structural robustness, we altered the potential during the stability test. As the $Sn_{0.3}Ti_{0.7}O_2$-β curve depicts, the selectivity was well maintained under a wide potential window (-0.54 V to -0.94 V). From stability tests, it was evident that the existence of Ti was essential to not only donate electron density and stabilize the lattice oxygen in the ternary Sn-Ti-O materials but also to strengthen the 3DOM structure. The demonstrated electrochemical performance and resistance to variations in potentials can broaden the utilization of catalysts and is essential for a practical CO_2RR system.

4.3. Conclusions

In summary, 3DOM ternary Sn-Ti-O catalysts were successfully produced, representing a simple but highly effective artificial material for CO_2RR. DFT calculations combined with different physical and chemical characterizations revealed the nature of the electron density reconfiguration among Sn, Ti, and O atoms. A balance between exposure of active sites and the degree of electron density shift was imperative for achieving a highly efficient 3DOM catalyst. In particular, it was inferred that the crucial electron density transfer from Ti to Sn enabled the dissociative adsorption of COOH*, directly producing CO with cathodic energy efficiency over 71.5%. The existence of Ti not only effectively creates an electron bank that contributes to the activation of catalytic reactions, but it also plays an important role in strengthening the 3DOM structure in order to maintain a high EE_{ca} for over 200 hours within a wide potential window. Insights gained through these quantitative analyses of electron density configuration can be further exploited as promising design principles for high-performance catalysts, making the electrochemical process more sustainable for practical applications.

4.4. Experimental Methods

4.4.1. Computational Methods

4.4.1.1. DFT Computation.

Periodic density functional theory (DFT) calculations including structure relaxations, single-point energies, and electronic structures were performed using Vienna Ab Initio Simulation Package (VASP 5.4.4).[183] The electron exchange-correlation potential was described by the Perdew-Burke-Ernzerhof (PBE) functional of generalized gradient approximation (GGA).[187] In order to make comparable DFT models (i.e. similar lattice parameters and space group) showing the interaction in Sn-Ti-O interface: 1. pure $TiO_{2-\delta}$ and Sn-doped $TiO_{2-\delta}$; 2. pure $SnO_{2-\delta}$ and Ti-doped $SnO_{2-\delta}$. Since pure $TiO_{2-\delta}$ catalysts are inactive, we adopted the latter configurations in the DFT calculations. The (110) facet of SnO_2 identified by XRD patterns and HRTEM characterization[75, 86] was built with 2 × 2 supercell and 6 atomic layers ($Sn_{24}O_{48}$). Model I (i.e. SnO_2) was generated with 6 oxygen vacancies ($SnO_{2-\delta}$)[204] owing to the fact that the surface tin oxide layer can be partially reduced to Sn^{2+} oxide at reaction conditions.[50, 86] Model II was built as Model I with three Ti atoms substituting Sn on the surface (i.e. $Sn(Ti)O_{2-\delta}$) in order to investigate the role of Ti.

A vacuum layer of 20 Å was added to separate neighboring slabs to avoid possible interaction. Monkhorst-Pack k-points of 2×2×1 mesh was utilized for a sampling of the Brillouin zone for structural relaxation. An 8 × 8 × 8 k-points mesh was used for the density of states calculation. The electronic self-consistency loop was converged within 1×10^{-4} eV using a residual minimization method direct inversion in the iterative subspace (RMM-DIIS) algorithm. Spinpolarization calculations with an energy cut off for the plane waves of 400 eV and a Hellmann-Feynman[239] force of 0.02 eV/Å was adopted as the convergence criterion for optimization of the full structure. By increasing the cut-off energy to 450 eV and the k-points to 4×4×1, we observed a negligible change in adsorption energies (<0.01 eV), which indicates that energetic values have asymptotically converged to the parameters used in this study. DFT+U method was implemented to correct the on-site Coulomb interactions for the localized Ti3d electrons. The value of U was chosen to be 4.0 eV because it can generate a similar electronic structure that was experimentally observed.[240] U = 0 eV was used for Sn4d electrons as it has no contribution near the Fermi level.[241]

The reaction energy ΔE is defined as follows:[190-191]

$$\Delta E = E_{(FS)} - E_{(IS)} \tag{4-1}$$

where $E_{(IS)}$ and $E_{(FS)}$ represent the zero-point energy (ZPE)-correction energies of the initial state (IS) and final states (FS), respectively. Negative values of ΔE represent exothermic reactions.

The adsorption energy E_{ads} of surface species is defined as follows:[190-191]:

$$E_{ads} = E_{absorbates/slab} - E_{slab} - E_{adsorbates} \tag{4-2}$$

where $E_{absorbates/slab}$, $E_{adsorbates,}$ and E_{slab} represent the total energy (eV) of surface slabs with adsorbates, the energy of free adsorbates, and the energy of bare surface slabs, respectively.

The computational analysis considers two main pathways for CO and $HCOO^-$ production from the adsorption of bicarbonate (CO_3H^*) species.[86] The H_2CO_3 forms via hydrogen bonds, followed by a rapid balance (R1) between CO_2 and H_2CO_3.[84, 175]

$$CO_2 + H_2O \rightleftarrows CO_3H^- + H^+ \tag{R1}$$

$$CO_3H^* + * + H^+ + e^- \rightarrow COOH^* + OH^* \tag{R2a}$$

$$CO_3H^* + {}^* + H^+ + e^- \rightarrow HCOO^* + OH^* \tag{R2b}$$

$$COOH^* + {}^* + H^+ + e^- \rightarrow CO^* + H_2O^* \tag{R3a}$$

$$HCOO^* + H^+ + e^- \rightarrow HCOOH^* \tag{R3b}$$

4.4.1.2. FEM simulations.

Finite element method (FEM) simulations were performed using the COMSOL Multiphysics software package. *Secondary Current Distribution* and *Transport of Diluted Species* modules were used to establish comprehensive chemistry–mass transport model of the 3DOM structure.[235, 242]

4.4.2. Experimental Section

4.4.2.1. Synthetic Procedures

The 3DOM $Sn_xTi_{1-x}O_2$ was synthesized by using a sacrificial polymer template method. Firstly, polystyrene (PS) beads were prepared by an emulsifier-free emulsion polymerization in which polyvinylpyrrolidone (PVP), styrene, and potassium persulfate ($K_2S_2O_8$) were employed as dispersion agent, monomer, and initiator, respectively. The details for the polymerization were reported in our previous study.[211-212] Once the polymerization was finished, the PS colloidal solution was centrifuged at a low rotation speed for 12 h and dried at 60 °C to acquire a close-packed PS beads template. Meanwhile, in terms of a preparation of metal precursor solution, tin chloride ($SnCl_2$), titanium (IV) butoxide, hydrochloric acid (HCl), and ethanol were utilized. In detail, $SnCl_2$ and titanium (IV) butoxide were firstly dissolved in ethanol followed by the addition of a certain amount of HCl, where the molar ratio of the solution was kept at 2 M (mole of metals/volume of solvent). Different molar ratios between the metal precursors were tried. The amount of HCl was increased as the volume of titanium precursor was raised since HCl is required to dissolve titanium hydroxide formed in ethanol solution in order to obtain a clear metal precursor solution. The prepared metal precursor solutions with various ratios were infiltrated into the voids of the close-packed PS beads template by soaking the template into the precursor solution for 4h. Then, the metal precursor-soaked PS beads templates were collected by a vacuum filtration that removes excess precursor solution, followed by a drying process in ambient conditions overnight. After the metal precursor soaked PS beads template was completely dried, it was heated to 600 °C in an airstream with a ramping rate of 1 °C min^{-1} and soaked for 3 h to burn and eliminate the polystyrene beads leaving meso-/macro-pores while the metal precursors were solidified building a robust metal oxide skeletal framework. Five samples demonstrated a clear and uniform 3DOM structure, where the resultant samples were named using surface atoms ratios: 3DOM-SnO_2, $Sn_{0.3}Ti_{0.7}O_2$, $Sn_{0.2}Ti_{0.8}O_2$, $Sn_{0.1}Ti_{0.9}O_2$, and 3DOM-TiO_2. With a higher Sn-Ti ratio, such as $Sn_{0.4}Ti_{0.6}O_2$, $Sn_{0.6}Ti_{0.4}O_2$, and $Sn_{0.8}Ti_{0.2}O_2$, it was hard to form a stable 3DOM structure (**Figure S4-8**), although there were randomly distributed porous frameworks. The formation of a range of unique structures can be described by the selective surface migration, phase separation and oxidation of the metals during calcination.[213]

4.4.2.2. Characterization

The 3DOM $Sn_xTi_{1-x}O_2$ were characterized by the following techniques: XRD (X-ray diffraction, Rigaku Miniflex 600) and XPS (X-ray Photoelectron Spectrometer, Thermo Scientific K-alpha XPS spectrometer) was used to confirm the crystal structure and elemental composition, respectively. XRD patterns were obtained with $Sn_xTi_{1-x}O_2$ electrodes (catalysts on the carbon papers). SEM (Scanning electron microscopy, LEO FESEM 1530) and TEM (transmission electron microscopy, JEOL 2010F) was employed to observe the morphology of the electrodes. HRTEM analysis was performed using an aberration-correction FEI Titan 80-300 (FEI Company, The Nether-lands) transmission electron microscope equipped with a Gatan Quantum energy filter (Gatan Inc., USA) and a high-brightness electron source. Imaging was carried out using a high-angle annular dark-field (HAADF) detector, with compositional mapping obtained using electron energy loss spectroscopy (EELS). X-ray absorption near-edge spectroscopy (XANES) of Ti K-edge and Sn L_3-edge and extended X-ray absorption fine structure (EXAFS) of Ti K-edge measurements were performed at Canadian Light Source Inc, Canada, using the Soft X-ray Microcharacterization Beamline (SXRMB). Reference compounds, such as titanium powder, titanium oxides, tin oxides (II), and tin oxides (IV) in the anatase phase were measured in total electron and transmission modes for comparison and energy calibration. All XANES and EXAFS data were processed using the Athena program (http://bruceravel.github.io/demeter/documents/Athena/index.html). The FDMNES (Finite Difference Method Near Edge Structure)[223-226] was used to simulate the Ti XANES spectra using Model II ($Sn(Ti)O_{2-\delta}$) in DFT models in order to compare with the XANES measurements, and further to verify the DFT models.

4.4.2.3. Electrochemical Measurement

CO_2RR was conducted according to the previous work.[86] In a typically prepared procedure of the working electrode, 3 ml of the homogeneous ink, which was prepared by dispersing 5 mg sample and 80 μl Nafion solution (5 wt%) in 1 ml water-ethanol solution with a volume ratio of 1:1, was loaded onto Sigracet 29 BC carbon paper of 1.0 × 0.5 cm. CO_2RR experiments were carried out in a CO_2-saturated 0.5 M $KHCO_3$ solution (30 ml). The $KHCO_3$ electrolyte was purged with CO_2 for 30 min prior to the measurement. The CO_2RR was performed for 2 hrs at various potentials in the electrolyte. The electrochemical measurements were carried out using a Gamry potentiostat. The current densities reported in this work were normalized to the geometric surface area. Three independent measurements were performed, and the results presented are the averaged values (**Table S4-4**). All the experiments were conducted under ambient pressure and at room temperature (23°C).

4.4.2.4. Products Analysis

The concentration of reaction products in the liquid electrolyte was detected using a 500 MHz ^{1}H liquid NMR spectrometer (Bruker Advance) with the water suppression method.[86] Gas products were quantified by on-line gas chromatography (GC, SRI 8610C). The GC is equipped with a packed Molecular Sieve column and a Helium ionization detector (HID). Helium (Praxair Gas, 99.999%) was used as the carrier gas.

4.5. Supporting Tables and Figures

Table S4-1. CO_2RR performance of Sn-based electrocatalysts.

Cell type/ Product	Catalyst	Electrolyte	Cathode Potential (V_{RHE})	Faradaic efficiency (%)	Cathodic energy efficiency (%)	Current Density (mA cm^{-2})	Stability (h)	Ref.
H- cell/ Formate	Bi-Sn / CF	0.5 M $KHCO_3$	-1.14	96	51	45	100	86
	Graphene confined Sn quantum sheets	0.1 M $NaHCO_3$	-1.1	93	50	25	50	75
	Ag_3Sn Core−Shell Structure	0.5 M $NaHCO_3$	-0.9	87	51	20	25	50
	Sn-OH-5.9 branches	0.1M KCl	-0.94	82	48	15	60	84
	Single-atom $Sn^{\delta+}$ on N-doped graphene	0.25 M $KHCO_3$	-0.9	75	44	18	200	200
	Pd-Sn nanoparticles[194]	0.5 M $KHCO_3$	-0.43	99	75	30	5	194
	Cu/SnO_2 Core−Shell Structure	0.5 M $KHCO_3$	-0.9	85	50	22	-	49
	Sulfur-Modulated Tin Sites	0.1 M $KHCO_3$	-0.75	93	59	55	40	74
	SnO_x/graphene	0.1 M $NaHCO_3$	-1.16	94	50	10	-	58
	Electroplated Sn/gas diffusion electrode	0.5 M $NaHCO_3$	-1.10	71	38	20	6	148
	Electrodeposited Sn dendrite	0.1 M $KHCO_3$	-1.36	83	40	25	18	98
	Sn modified N-doped carbon nanofiber	0.5 M $KHCO_3$	-0.8	62	38	9	24	102
	Tin monoxide (SnO) nanoparticles	0.5 M $KHCO_3$	-0.86	75	45	10	-	81
Flow cell/ Formate	Sn-based gas diffusion electrode	0.5 M KCl	4.0 (Cell voltage)	84	32 (Full cell EE)	163	-	243

	Sn 3D electrode	0.5 M $KHCO_3$ + 2 M KCl	3.1 (Cell voltage)	83	33 (Full cell EE)	133	-	[244]
H- cell/ Carbon monoxide	Sn-Ti-O	0.5 M $KHCO_3$	-0.54	94.5	71.5	3.91	200	This Work
	Sn-Ti-O	0.5 M $KHCO_3$	-0.94	94.5	58.3	33	200	This Work
	Cu/SnO_2 Core−Shell Structure	0.5 M $KHCO_3$	-0.7	93	64	4.6	-	[49]
	Sn/SnO_2	0.5 M $NaHCO_3$	-0.7	58	40	3	5	[32]
	$CdSnO_3$	0.5 M $NaHCO_3$	-0.9	20%	12	6	-	[166]
	$ZnSnO_3$	0.5 M $NaHCO_3$	-0.9	18%	11	4	-	[166]

Table S4-2. Calculated Band center of the Sn atom on Model I and II.

Band center of Sn atom	Surface Models		Variation (I-II)
	Model I: $SnO_{2-\delta}$	Model II: $Sn(Ti)O_{2-\delta}$	
s	-0.17	-3.05	-2.88
p	+6.27	+3.51	-2.76
d	-14.2	-16.46	-2.29
R (Sn) = 139 ± 4 pm; R (Ti) = 160 ± 8 pm;			

Table S4-3. The adsorption energies of HCOO* and HCOOH* on Model I and Model II.

Intermediate Species	Adsorption energy/eV	
	Model I: $SnO_{2-\delta}$	Model II: $Sn(Ti)O_{2-\delta}$
HCOO*	-2.20	-3.11
HCOOH*	-0.15	-1.65

Table S4-4. Summary of electron density transfer effects on Model II.

Product species	Effect of e⁻ density transfer	Result
HCOOH	Stronger Ti-O bond formation → Overly stabilized intermediates	High reaction energy → HCOOH product not favored
CO	Weakening Sn-C bond →Fewer reaction steps	Low reaction energy → CO product favored

Table S4-5. The compositions of the synthesized ternary Sn-Ti-O materials obtained from XPS.

Sample	Sn: Ti ratios	
	XPS measured	Targeted
3DOM SnO_2	1:0	1:0
$Sn_{0.8}Ti_{0.2}O_2$	0.82:0.18	0.85:0.15
$Sn_{0.6}Ti_{0.4}O_2$	0.64:0.36	0.60:0.30
$Sn_{0.4}Ti_{0.6}O_2$	0.42:0.58	0.55:0.45
$Sn_{0.3}Ti_{0.7}O_2$	0.28:0.72	0.40:0.60
$Sn_{0.2}Ti_{0.8}O_2$	0.21:0.79	0.25:0.75
$Sn_{0.1}Ti_{0.9}O_2$	0.12:0.88	0.10:0.90
3DOM TiO_2	0:1	0:1

Note: It is important to note that catalytic reactions occur on the surface of the materials, and therefore penetration capabilities of various characterization techniques must be considered. XPS technique can detect surface properties to a depth of approximately 5 nm, so the composition information from the XPS spectrum was used as the basis for naming the samples. It is important to note that the difference between targeted ratios and XPS measured ratios might due to the depth limitation of XPS techniques and the shell of discrete and dispersed TiO_2.

Additionally, DFT calculations are based on models with dimensions less than 1 nm and the composition information in the depth of 1 nm and 5 nm might not be the same. Therefore, the ratio derived from XPS results cannot be directly used to compare with DFT models.

DFT simulations were intended to firstly give local electronic reconfiguration information regarding Sn-Ti-O systems. We wanted to understand the effect of Ti addition on the atomic surface and observe changes in the Sn-Ti-O interaction. We synthesized a series of ternary Sn-Ti-O catalysts with varying surface ratios of Sn-Ti to confirm and expand the predictions from DFT. From the characterization of catalysts, it was found that a structural evolution accompanied the electronic reconfiguration modeled by DFT. From our results, there was a certain composition that had optimum electrochemical reduction performance due to a combination of structural and electronic properties. From this perspective, we believe that the calculations are still valid as a guide for materials synthesis.

Table S4-6. CO$_2$RR performance of ternary Sn-Ti-O electrodes in CO$_2$ saturated 0.5 M KHCO$_3$ aqueous solution.

3DOM SnO$_2$

Potential (V vs. SCE)	Potential (V vs. RHE) with iR Correction	FE(CO) (% ± 2.5%)	FE(HCOOH) (% ± 2.0%)	FE(H$_2$) (% ± 2.5%)	Current Density (mA cm^{-2})
-1.0	-0.34	54	1	45	0.2
-1.1	-0.44	46	8	47	0.9
-1.2	-0.54	43	18	40	2.5
-1.3	-0.64	46	26	27	6.9
-1.4	-0.74	43	36	20	10.8
-1.5	-0.84	43	48	9	16.8
-1.6	-0.94	34	58	8	22.4
-1.7	-1.03	32	65	4	28.9
-1.8	-1.13	29	60	10	38.8
-1.9	-1.21	25	55	19	51.3
-2.0	-1.32	24	45	30	63.8

Sn$_{0.4}$Ti$_{0.6}$O$_2$

Potential (V vs. SCE)	Potential (V vs. RHE) with iR Correction	FE(CO) (% ± 2.5%)	FE(HCOOH) (% ± 2.0%)	FE(H$_2$) (% ± 2.5%)	Current Density (mA cm^{-2})
-1.0	-0.34	41	6	49	0.2
-1.1	-0.44	44	13	42	1.9
-1.2	-0.54	47	20	30	4.7
-1.3	-0.64	47	27	21	7.3
-1.4	-0.74	48	35	17	12.9
-1.5	-0.84	47	41	8	18.9
-1.6	-0.94	43	46	9	28.0
-1.7	-1.03	43	43	10	36.8
-1.8	-1.13	40	39	21	46.4
-1.9	-1.21	28	33	38	70.9

Sn$_{0.3}$Ti$_{0.7}$O$_2$

Potential (V vs. SCE)	Potential (V vs. RHE) with iR Correction	FE(CO) (% ± 2.5%)	FE(HCOOH) (% ± 2.0%)	FE(H_2) (% ± 2.5%)	Current Density (mA cm^{-2})
-1.0	-0.34	44	1	53	0.2
-1.1	-0.44	66	2	31	0.7
-1.2	-0.54	92	2	6	3.9
-1.3	-0.64	91	3	4	10.0
-1.4	-0.74	92	4	3	16.9
-1.5	-0.84	93	4	3	24.6
-1.6	-0.94	92	4	4	33.3
-1.7	-1.03	84	10	6	45.5
-1.8	-1.13	69	12	16	55.0
-1.9	-1.21	50	7	40	66.7

$Sn_{0.2}Ti_{0.8}O_2$

Potential (V vs. SCE)	Potential (V vs. RHE) with iR Correction	FE(CO) (% ± 2.5%)	FE(HCOOH) (% ± 2.0%)	FE(H_2) (% ± 2.5%)	Current Density (mA cm^{-2})
-1.0	-0.34	39	3	58	0.1
-1.1	-0.44	47	2	51	1.9
-1.2	-0.54	54	5	41	2.6
-1.3	-0.64	64	8	29	6.8
-1.4	-0.74	66	8	26	12.5
-1.5	-0.84	66	13	21	21.1
-1.6	-0.94	67	16	16	29.8
-1.7	-1.03	62	24	13	39.3
-1.8	-1.13	53	19	27	53.9
-1.9	-1.21	42	10	48	71.2

$Sn_{0.1}Ti_{0.9}O_2$

Potential (V vs. SCE)	Potential (V vs. RHE) with iR Correction	FE(CO) (% ± 2.5%)	FE(HCOOH) (% ± 2.0%)	FE(H_2) (% ± 2.5%)	Current Density (mA cm^{-2})
-1.0	-0.34	16	0	84	0.1
-1.1	-0.44	25	1	74	0.2

-1.2	-0.54	28	2	70	3.2
-1.3	-0.64	30	3	67	8.1
-1.4	-0.74	36	4	60	13.2
-1.5	-0.84	36	5	59	21.0
-1.6	-0.94	36	8	56	30.5
-1.7	-1.03	40	10	50	43.8
-1.8	-1.13	36	6	58	53.6
-1.9	-1.21	34	5	61	69.8
3DOM TiO_2					
Potential (V vs. SCE)	Potential (V vs. RHE) with iR Correction	FE(CO) (% ± 1.5%)	FE(HCOOH) (% ± 1%)	FE(H2) (% ± 2.5%)	Current Density (mA cm^{-2})
-1.0	-0.34	1	0	60	0.1
-1.1	-0.44	1	0	96	1.4
-1.2	-0.54	2	0	97	2.0
-1.3	-0.64	3	0	98	5.0
-1.4	-0.74	1	0	96	9.2
-1.5	-0.84	0	0	95	15.5
-1.6	-0.94	2	2	90	21.8
-1.7	-1.03	4	3	93	28.1
-1.8	-1.13	1	1	95	33.5
-1.9	-1.21	0	0	95	41.8

NOTE: The CO_2RR test was repeated three times and the results presented are the averaged values.

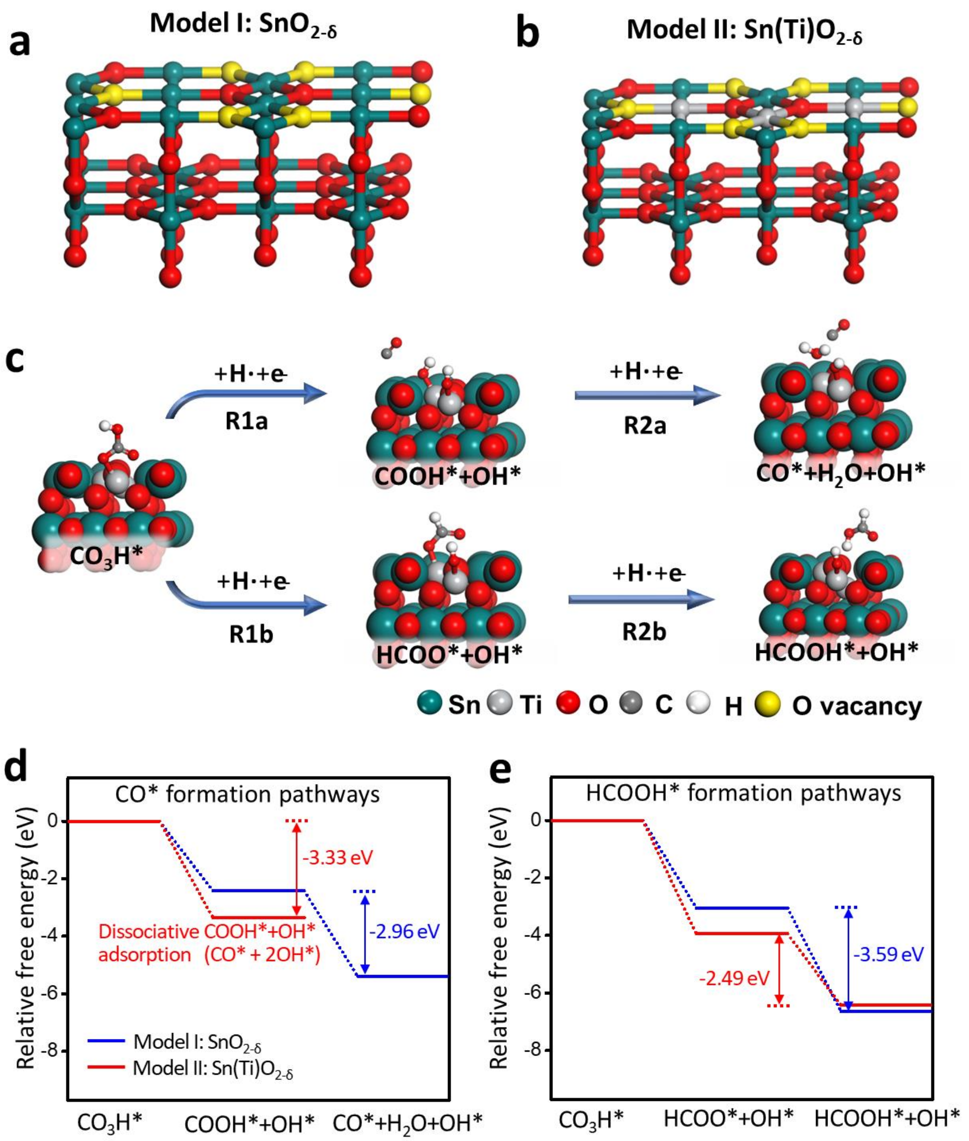

Figure S4-1. (a) Model I: SnO_2 with 6 oxygen vacancies ($SnO_{2-\delta}$) owing to the fact that the surface tin oxide layer can be partially reduced at reaction conditions (-0.8 V vs. RHE).[50, 86] (b) Model II: 1/8 Ti substitution of Sn on a surface based on Model I ($Sn(Ti)O_{2-\delta}$). (c) Simulation considering two pathways for CO and HCOOH production from CO_3H^*.[86, 175, 245] Calculated relative free energy profiles for CO_2RR to form (d) CO* and (e) HCOOH* on the Model I and II. All energies are with reference to the energies of CO_3H adsorbed on Sn (101) or Bi-Sn (101) surface.

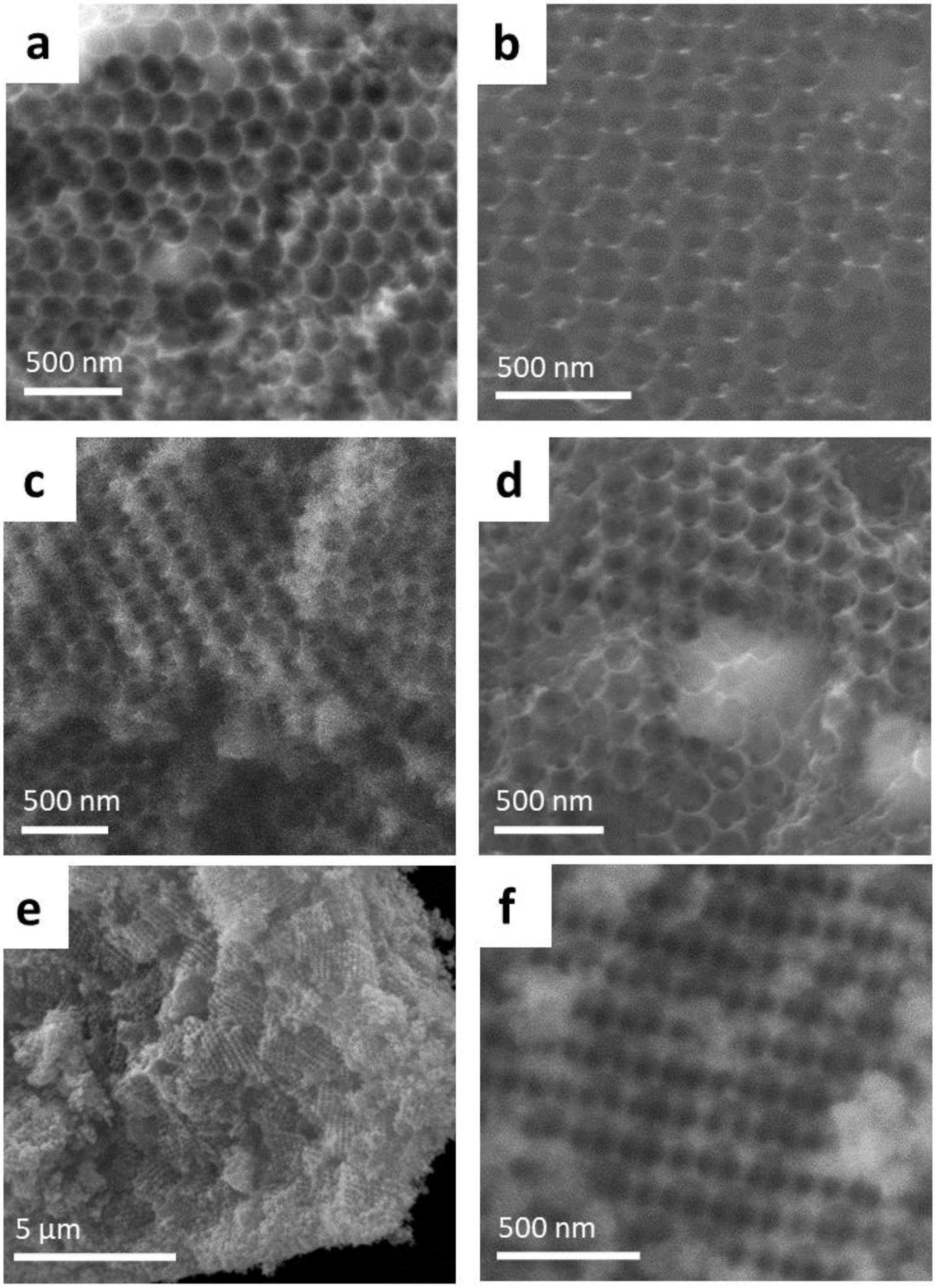

Figure S4-2. SEM images of (a) 3DOM TiO_2; (b) $Sn_{0.1}Ti_{0.9}O_2$; (c) $Sn_{0.2}Ti_{0.8}O_2$; (d, e) $Sn_{0.3}Ti_{0.7}O_2$; (f) 3DOM SnO_2.

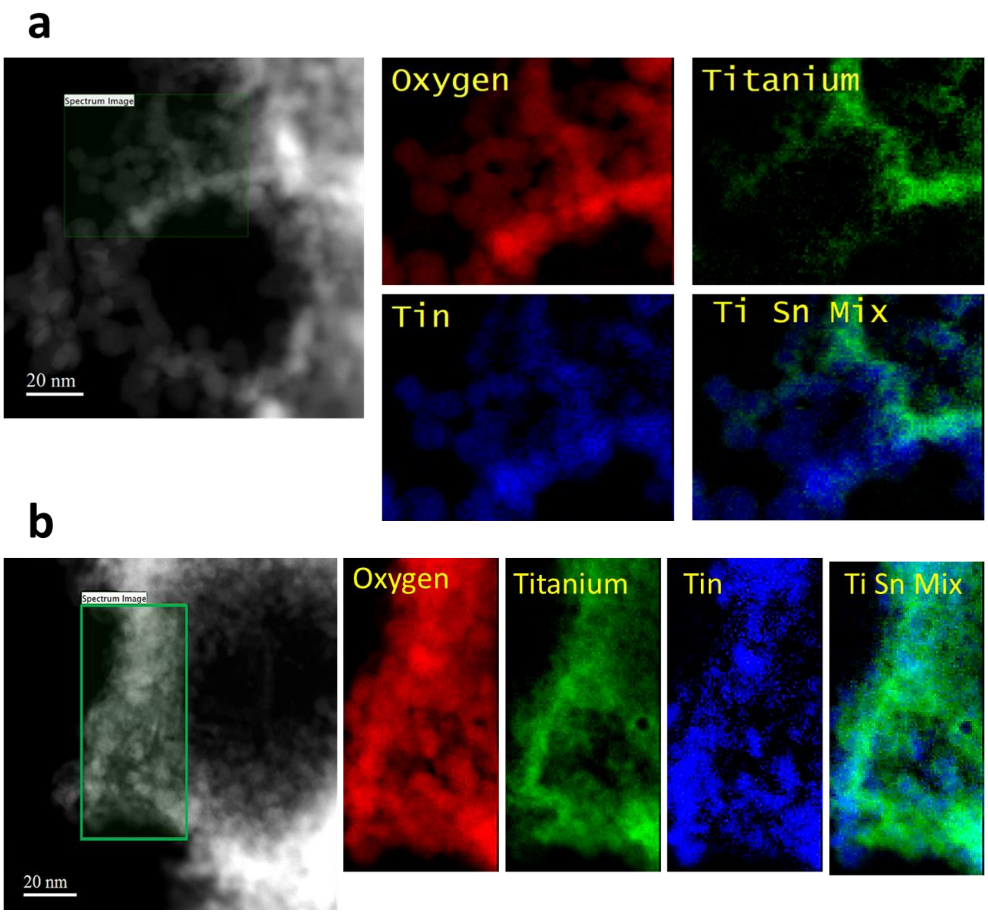

Figure S4-3. (a, b) Elemental mapping from EELS spectra of O, Ti, and Sn atoms of $Sn_{0.3}Ti_{0.7}O_2$ material within different areas.

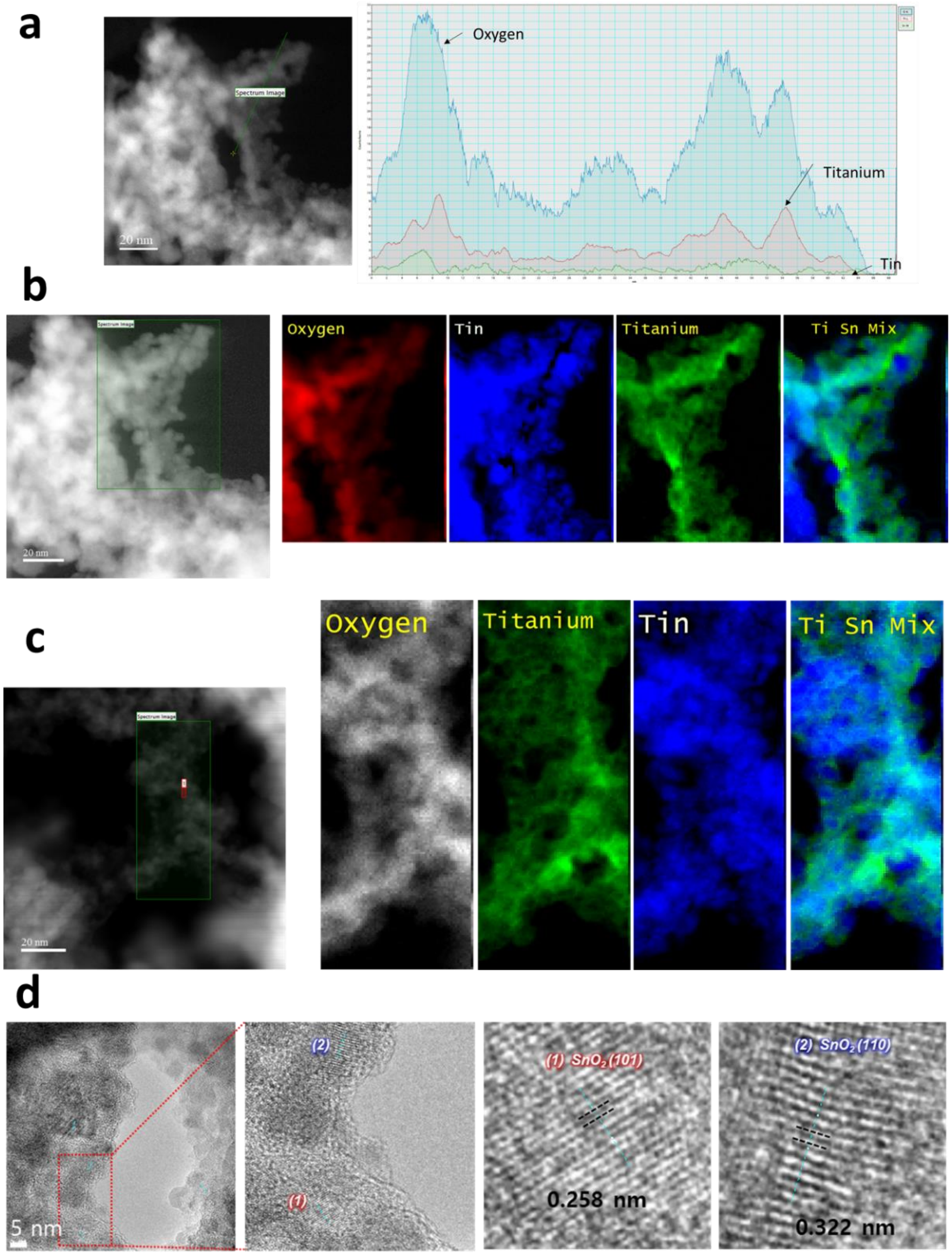

Figure S4-4. (a) Line scan from EELS spectra on the edge, (b, c) elemental mapping from EELS spectra of O, Ti and Sn atoms within different areas, and (d) HRTEM of $Sn_{0.2}Ti_{0.8}O_2$ material.

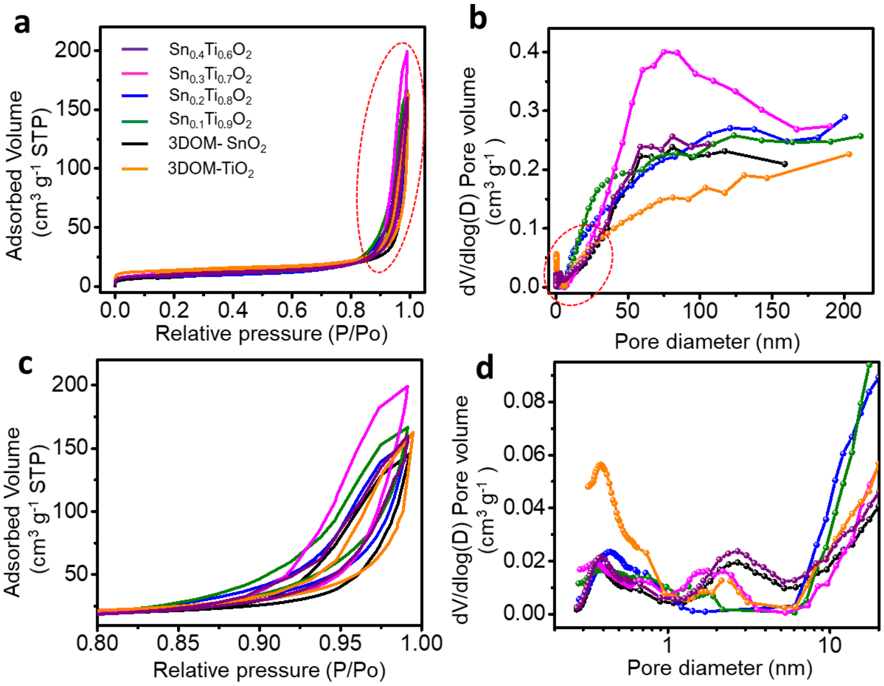

Figure S4-5. (a) N_2 adsorption-desorption isotherms, and (b) pore size distribution of the synthesized materials. (c) and (d) is the corresponding red region highlighted in (a) and (b), respectively.

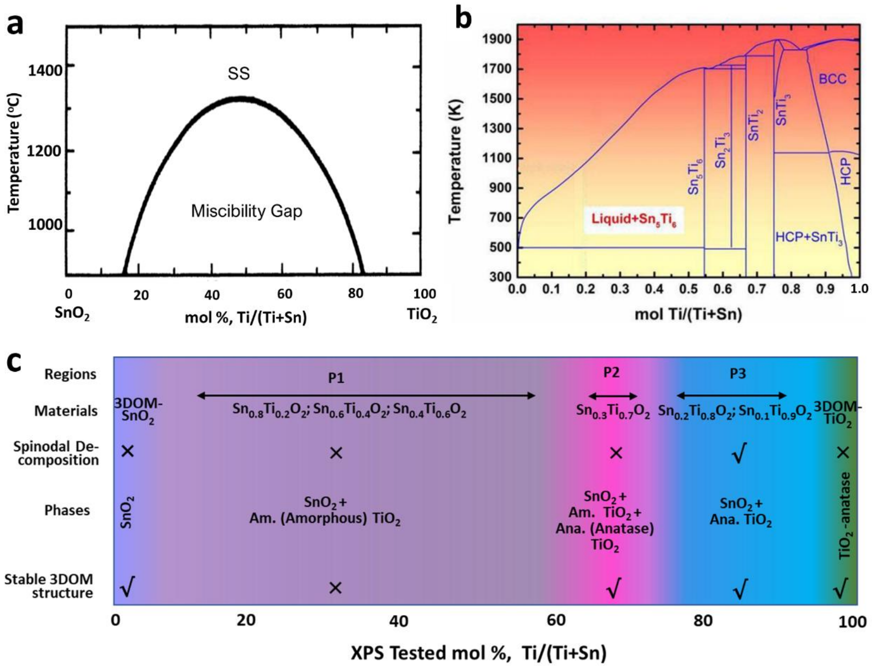

Figure S4-6. (a) The phase diagram of SnO_2-TiO_2 system[246] and Sn-Ti system[247]. Under the miscibility gap, the sample undergoes spinodal decomposition and consists of both SnO_2 and TiO_2 phases. (c) The properties of synthesized materials. The special $Sn_{0.3}Ti_{0.7}O_2$ material not only avoided complete spinodal decomposition, presenting mainly the SnO_2 phase with minor amorphous/ anatase TiO_2 phase but also maintained a stable 3DOM structure.

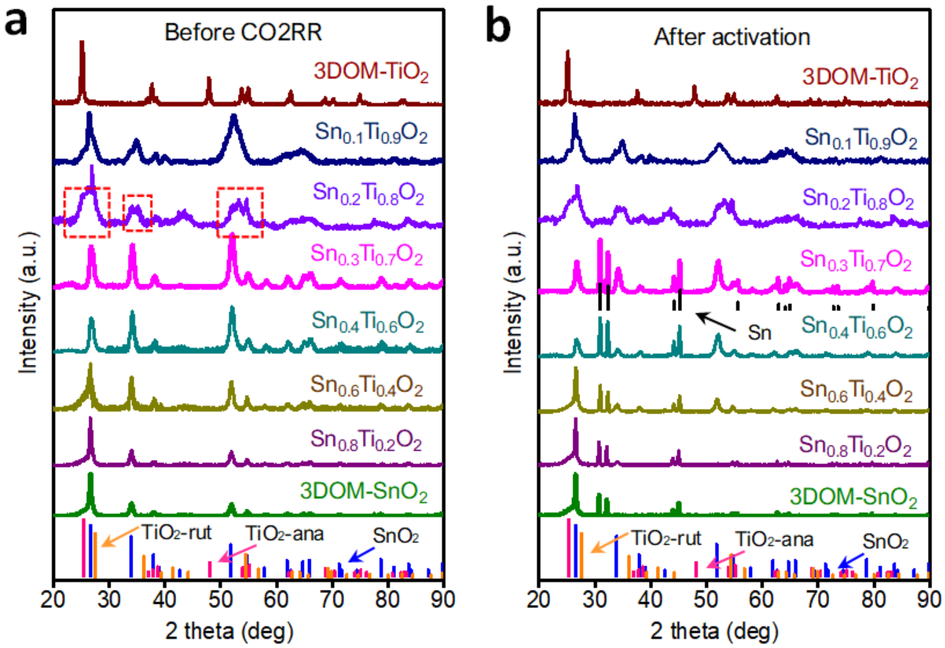

Figure S4-7. XRD patterns of the ternary Sn-Ti-O catalysts (a) before and (b) after the in-situ activation step. SnO_2: JCPDS 41-1445; TiO_2 in anatase phase: JCPDS 21-1272; TiO_2 in rutile phase: JCPDS 78-1510. Sn: JCPDS 04-0673. Boxed regions highlight major peak differences between different compositions.

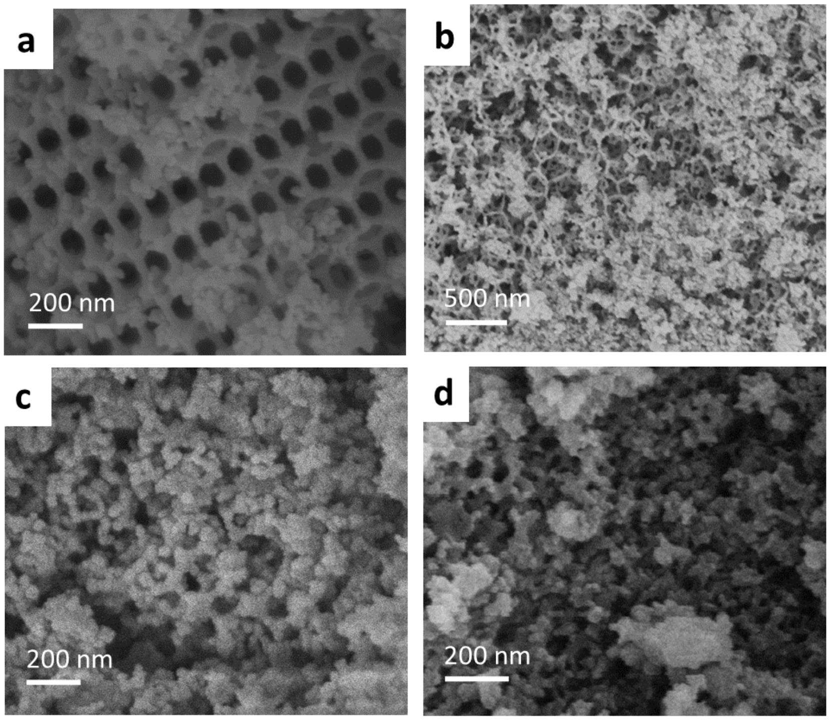

Figure S4-8. SEM images of (a) 3DOM SnO_2; (b) $Sn_{0.4}Ti_{0.6}O_2$; (c) $Sn_{0.6}Ti_{0.4}O_2$; (d) $Sn_{0.8}Ti_{0.2}O_2$.

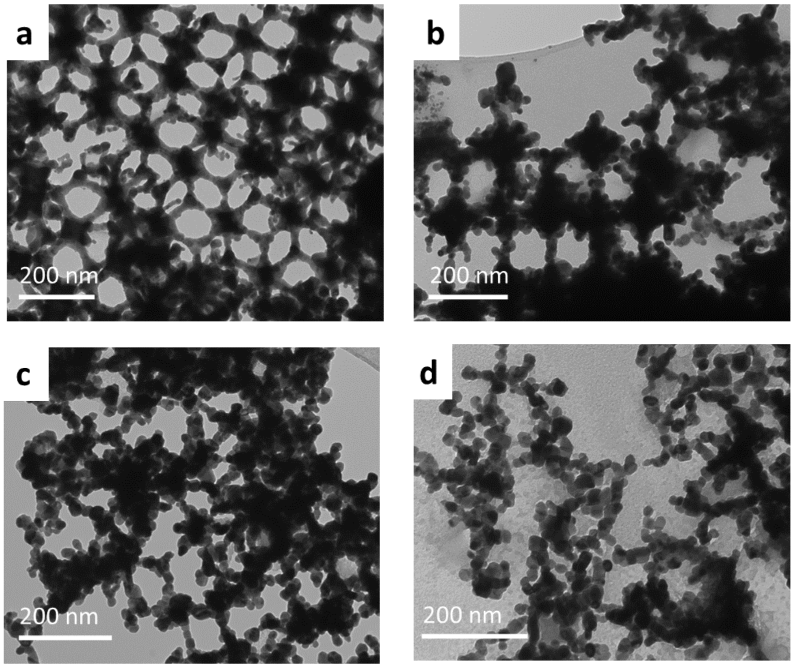

Figure S4-9. TEM images of (a) 3DOM SnO_2; (b) $Sn_{0.4}Ti_{0.6}O_2$; (c) $Sn_{0.6}Ti_{0.4}O_2$; (d) $Sn_{0.8}Ti_{0.2}O_2$.

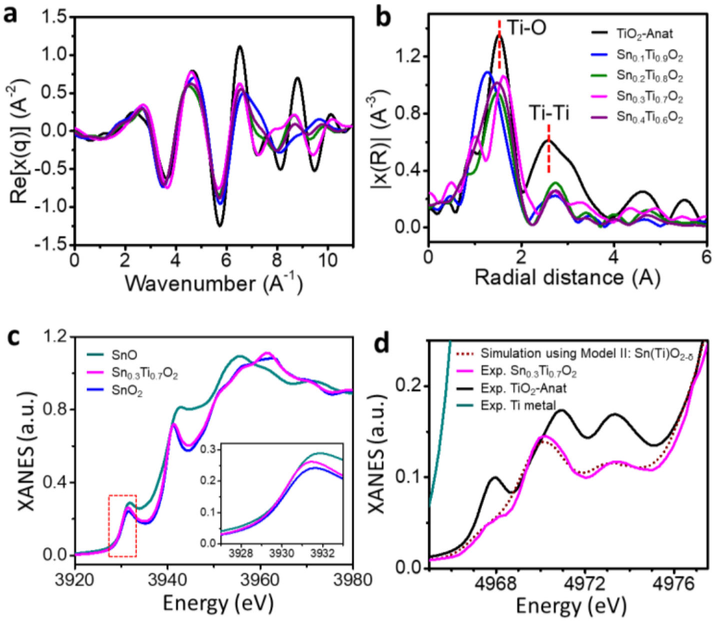

Figure S4-10. (a) Ti K-edge extended X-ray absorption fine structure (EXAFS) spectra for samples anatase TiO_2 and various ternary Sn-Ti-O materials. (b) the corresponding Fourier Transforms (FTs). (c) Sn L_3-edge XANES spectra of $Sn_{0.3}Ti_{0.7}O_2$ and two reference materials (SnO and SnO_2). Inset shows higher magnification of the pre-edge. (d) Comparison of Ti K-edge XANES spectra between FDMNES simulation from DFT Model II ($Sn(Ti)O_{2-\delta}$) and experimental measurements.

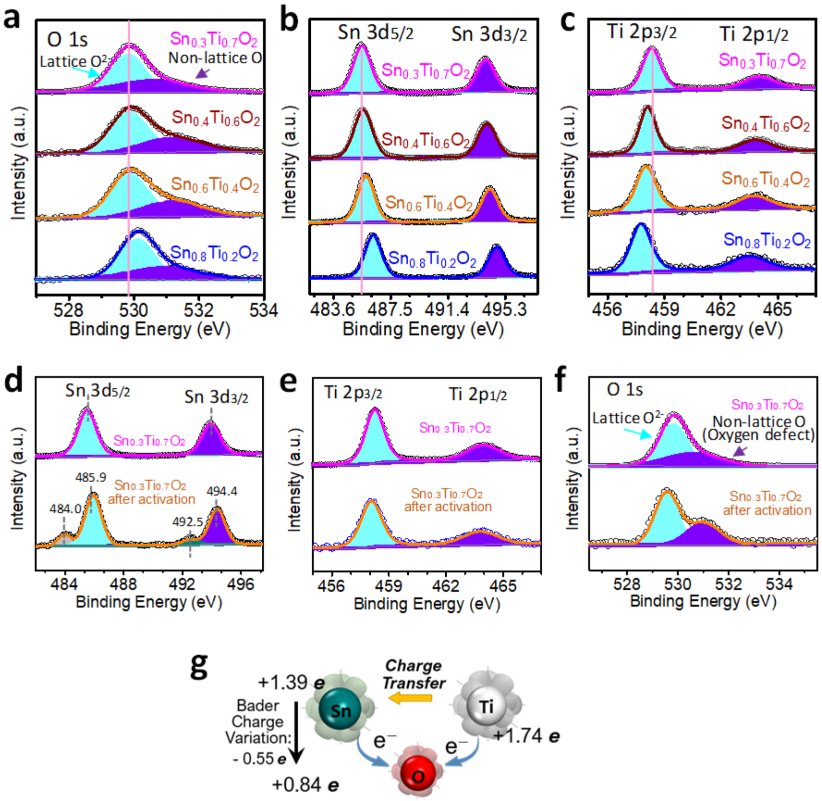

Figure S4-11. (a) O 1s, (b) Ti 2p, and (c) Sn 3d core-level XPS spectra of $Sn_{0.3}Ti_{0.7}O_2$, $Sn_{0.4}Ti_{0.6}O_2$, $Sn_{0.6}Ti_{0.4}O_2$, and $Sn_{0.8}Ti_{0.2}O_2$ materials. (d) Sn 3d, (e) Ti 2p, and (f) O 1s core-level XPS spectra of $Sn_{0.3}Ti_{0.7}O_2$ catalyst before and after the activation step. (g) Schematic of Bader charge transfer among Sn, Ti, and O atoms.

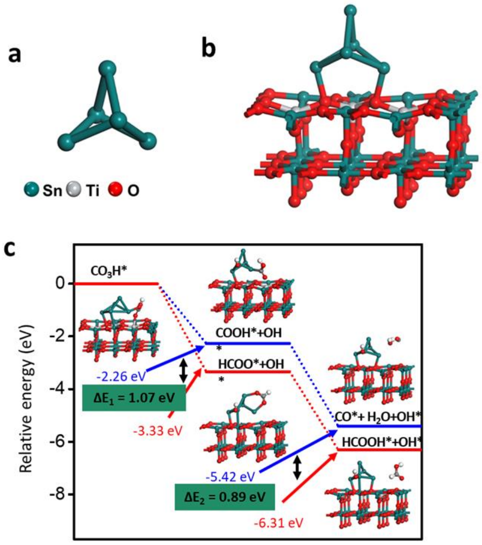

Figure S4-12. (a) The most stable Sn_5 cluster. (b) Model III: Sn_5-Sn(Ti)O_2 model with Sn_5 cluster mounted on the Sn(Ti)O_2 surface. (c) Calculated reaction energy profiles for CO_2RR to form CO (top) and HCOOH (bottom) on Model III. All energies are with reference to the energies of CO_3H adsorbed on the surface.

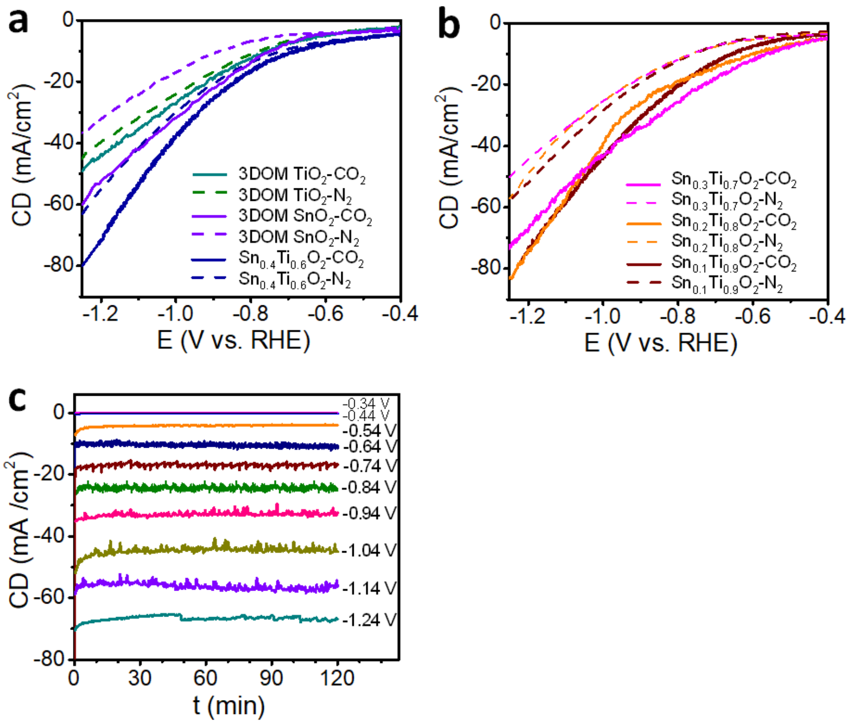

Figure S4-13. CO_2RR activities (linear sweep voltammetry, LSV curves) in a CO_2-purged (solid line) and N_2- purged (dotted line) 0.5 M $KHCO_3$ electrolyte at a scan rate of 20 mV s^{-1} of the prepared electrodes: (a) 3DOM-TiO_2, 3DOM-SnO_2, and $Sn_{0.4}Ti_{0.6}O_2$; and (b) $Sn_{0.3}Ti_{0.7}O_2$, $Sn_{0.2}Ti_{0.8}O_2$, and $Sn_{0.1}Ti_{0.9}O_2$. (c) Constant potential electrolysis (CPE) tests performed for 2 hours at a series of potentials from −0.34 to −1.24 V.

Note: The average current density (CD) at -0.34 V is 0.2 mA /cm^2, while the average CD at -0.44 V is 0.7 mA /cm^2. The curves of -0.34 V and -0.44 V appear to overlap with each other.

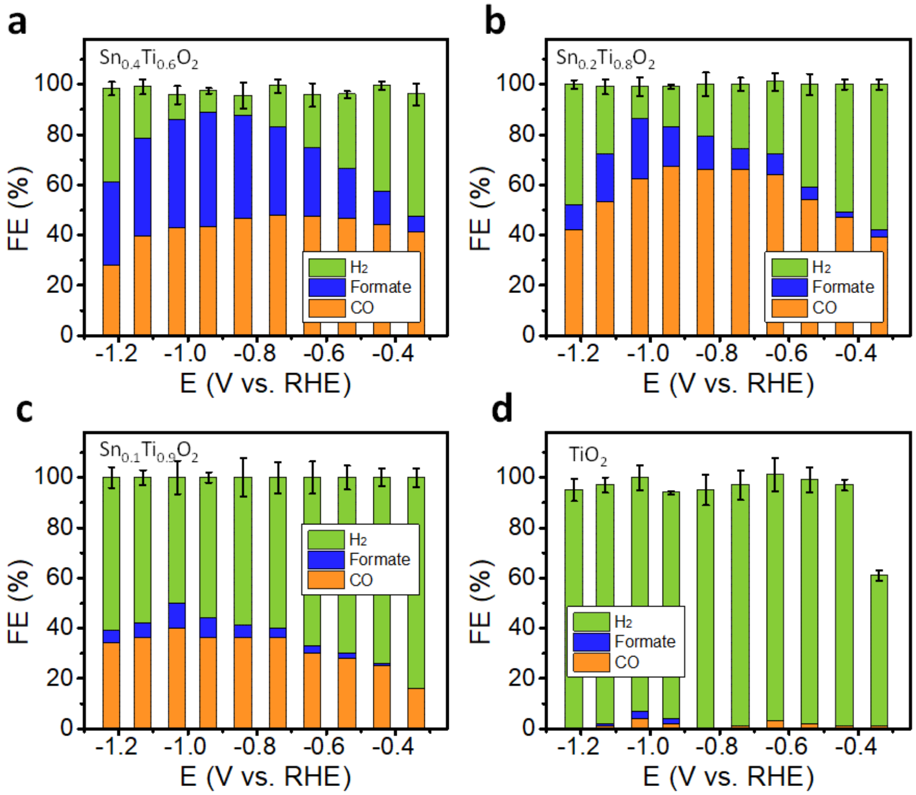

Figure S4-14. FE toward CO, formate, and H_2 on (a) $Sn_{0.4}Ti_{0.6}O_2$, (b) $Sn_{0.2}Ti_{0.8}O_2$, (c) $Sn_{0.1}Ti_{0.9}O_2$, (d) TiO_2 electrodes at a series of potentials from −0.34 to −1.21 V.

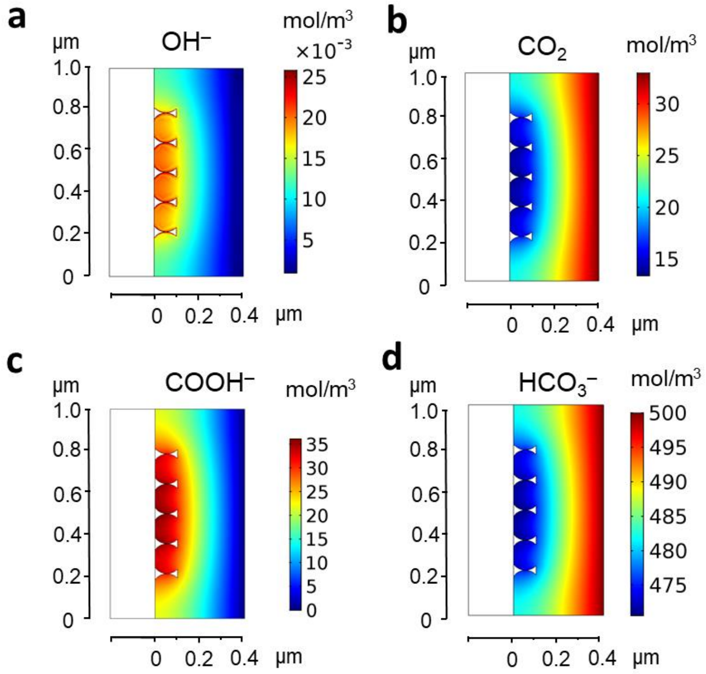

Figure S4-15. Calculated concentration profiles in the mesopores via FEM simulations.

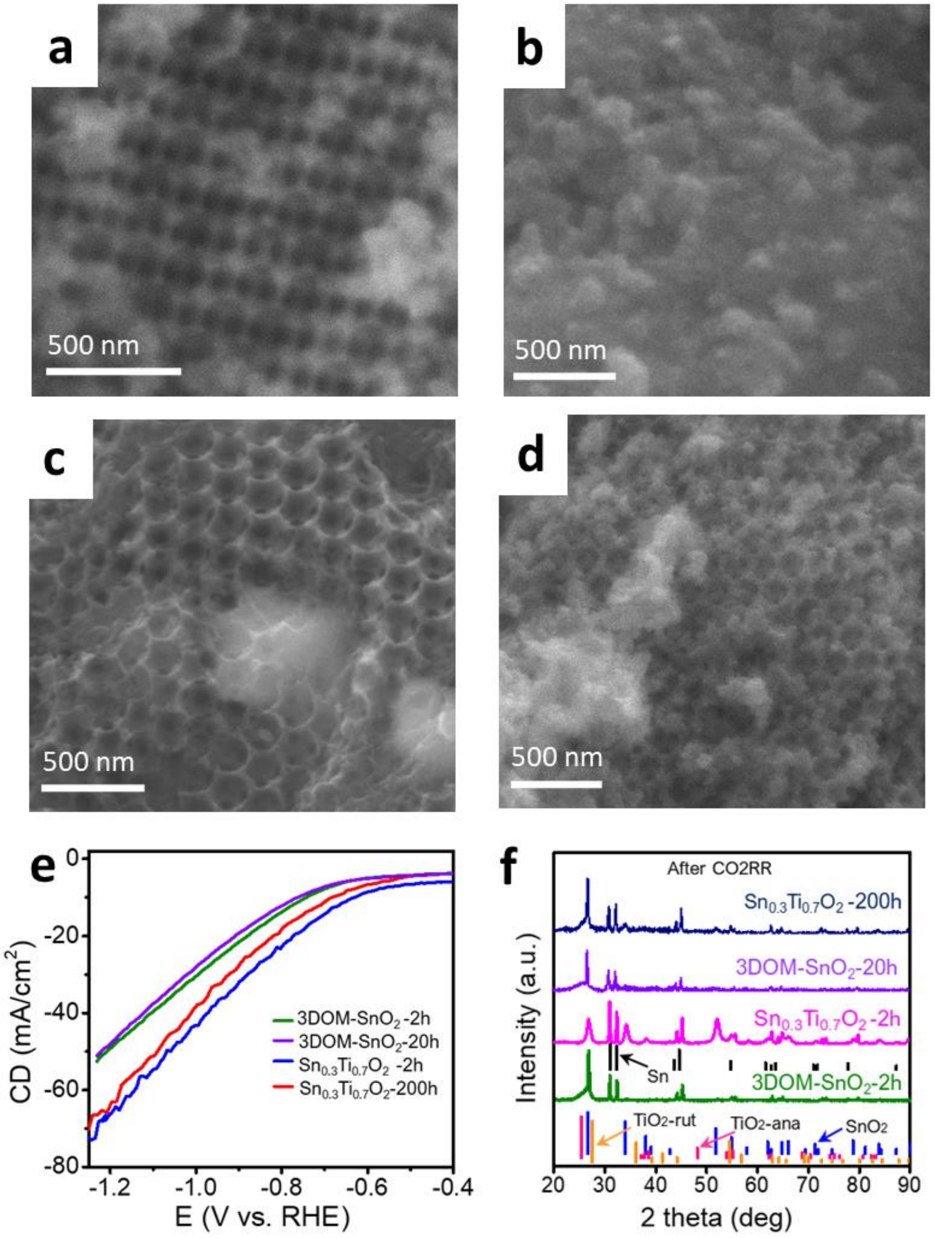

Figure S4-16. SEM images of 3DOM SnO_2 (a) before and (b) after stability test. SEM images of $Sn_{0.3}Ti_{0.7}O_2$ (c) before and (d) after stability test (Test α). (e) LSV curves before and after stability test. (f) XRD patterns of $Sn_{0.3}Ti_{0.7}O_2$ and 3DOM SnO_2 electrodes after the CO_2RR stability test. 3DOM SnO_2 displayed stability for only 20h, whereas $Sn_{0.3}Ti_{0.7}O_2$ was stable for 200h.

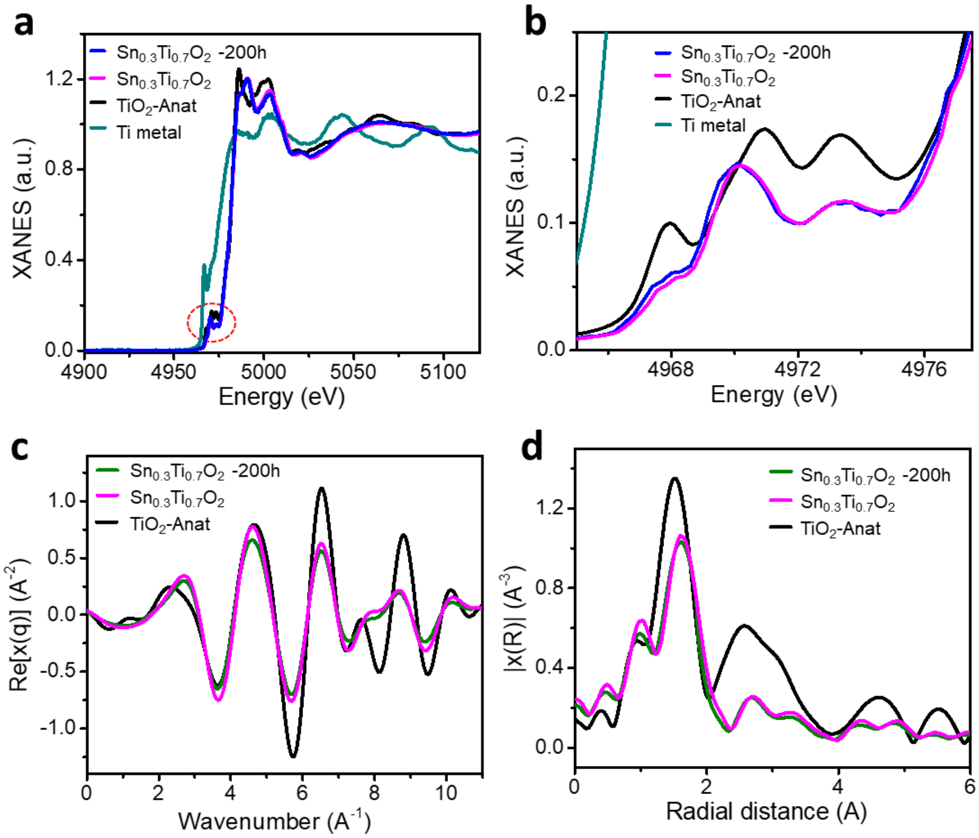

Figure S4-17. (a) XANES spectra of Ti, especially the $Sn_{0.3}Ti_{0.7}O_2$ electrodes before and after stability test (Test α). (b) The highlights of the selected red region in (a). (c) Ti K-edge EXAFS spectra and (d) the corresponding Fourier Transforms (FTs) for samples anatase TiO_2 and especially the $Sn_{0.3}Ti_{0.7}O_2$ electrodes before and after stability test (Test α).

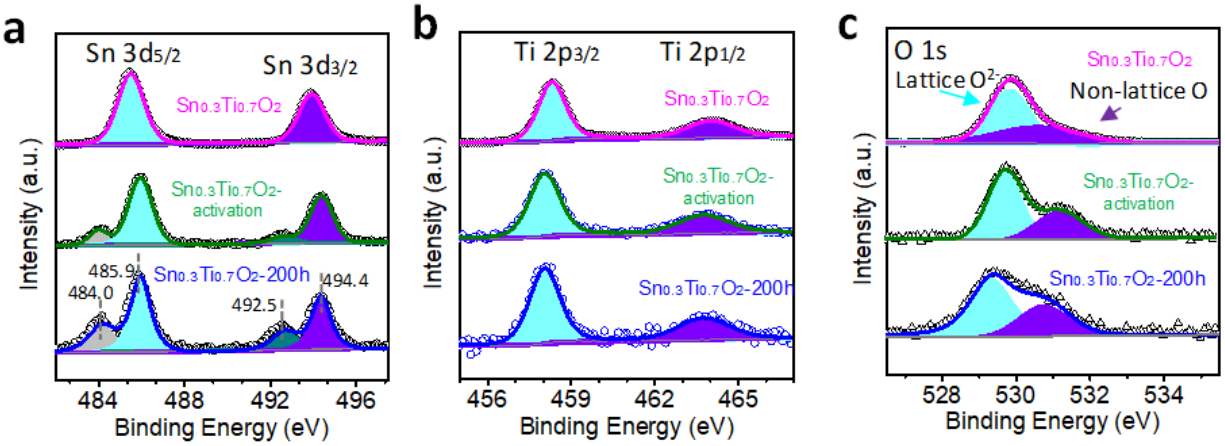

Figure S4-18. (a) Sn 3d, (b) Ti 2p, and (c) O 1s core-level XPS spectra of $Sn_{0.3}Ti_{0.7}O_2$ before and after the activation steps and stability tests (Test α), respectively.

Chapter 5. Continuous CO_2 Conversion by Aqueous Flow-through Cell

This chapter is a part of a manuscript that is co-authored by myself, my supervisors, and other collaborators.

Statement of Contributions: I devised the idea, assembled the cells, performed electrochemical experiments, and conducted FEM simulations. J. Gostick and Z. Chen supervised the work.

5.1. Introduction

Electrochemical carbon dioxide reduction reaction (CO_2RR) presents an opportunity to sequester CO_2 while synthesizing valuable chemicals and storing intermittent renewable energy.[9, 53, 62, 88, 237] Among a range of carbon-based products, the formation of CO is arguably one of the easier reactions since fewer electrons and protons are needed than for other carbon products.[62] Yet, after almost two decades of research, achieving practical reaction rates to make the process economical, e.g. partial current density for CO (J_{CO}) > 200 $mA \cdot cm^{-2}$ at low cell overpotentials ($\eta_{cell} < 1$ V), remains challenging. Recent developments in heterogeneous catalysis for CO_2RR are bringing this possibility closer to reality, so it is becoming imperative to develop improved designs for large-scale electrochemical cells.

Most of the aforementioned developments in heterogeneous catalyst have been done using batch-type (e.g., “H-cell”) electrolysis experiments.[6-7, 86, 91] This benchtop setup has a thick hydrodynamic boundary layer (BL), the limited size of electrodes, long transport distance for ionic species, and severely limited mass transport across the electrolyte when the current density over 100 $mA \cdot cm^{-2}$.[6, 86] The latter issue is a fundamental challenge in all CO_2RR technologies due to a relatively low solubility of CO_2 in aqueous solutions (~33 mM at 298 K and 1 atm pressure) causing mass transport limitations when using dissolved CO_2 as the reactant.[248]

There are several ways to design an electrochemical cell that avoids these limitations. In the recent review,[88] they identified two more categories beyond planar electrodes in aqueous electrolyte, which include a gas diffusion electrode (GDE) with vapor-feed and aqueous electrolyte, and a GDE with vapor-feed and polymer electrolyte. The GDE cell with vapor-feed and partially flooded aqueous electrolyte were extensively used in many research papers.[9, 62, 88, 147] The reaction occurs at the gas-liquid-solid interfaces, also known as the triple-phase boundary (TPB), where gaseous reactants, electrons, and ions meet. Although this GDE arrangement provides higher current density (CD), they further suffer from carbonate salt precipitation in the stagnant pores of the GDE, moreover in 1.0 M or 3.0 M KOH electrolyte CO_2 is parasitically converted to bicarbonate.[9, 80]

To remedy the latter problem, neutral electrolytes such as Na_2SO_4 or $KHCO_3$, [7, 89, 245] can replace highly alkaline electrolytes. Nonetheless, the systems with neutral electrolyte still demonstrate lower than desired energy efficiency (EE) due to high ohmic resistance and overpotentials in the GDE cells. Another major drawback of the TPB approach is the long-term instability of the partially flooded electrode with electrolyte, eventually leaching through the GDE and into the gas flow channels. To remedy this Higgins et al.[88] proposed the third category, an adaptation of the modern PEM fuel cell, with an ionomer-infused catalyst layer in place of the TPB. Although this has proven to be much more durable in the PEM fuel field, the limitations of diffusive mass transfer are still present. So, despite strong advances in materials investigations at the laboratory scale, suitable cells for CO_2RR are still called for.

Here, a “Zero-gap” aqueous flow-through cell was engineered for efficient continuous CO_2RR process. In this design, the electrode is fully wetting and an electrolyte solution bearing dissolved CO_2 is pumped through the pore-space, referred to as an aqueous flow-through (AFT) cell. In order to better understand the trade-offs inherent in the AFT cell design introduced above, a one-dimensional (1D) diffusion/transport model with considering bubble break-off and growth, as well as 2D reaction/diffusion models with different BL thicknesses were built to quantify the boundary layer (BL) thicknesses and the species distribution around the electrode surface, respectively.

AFT cell has the following advantages: (I) Flow through enhances mass transport, resulting in the boundary layer (BL) thickness reduced to less than 2 µm. While the BL thicknesses are around 10 µm and 30 to 120 µm for the GDE cell and the H-cell, respectively;[87, 91 91] (II) Zero-gap means the wetted porous electrode is pressed and in physical contact with the membrane separator, reducing the ion transport length; (III) Flow electrolyte with carbon sources in the form of dissolved CO_2 and HCO_3^- eliminates the degradation related to electrolyte flooding and carbonate precipitation and removes the troublesome TPB component. (IV) The AFT cell developed in this work contributed to cost-competitive CO_2-to-CO transformation with Ag nanoparticles on carbon fibers (Ag NP/CF) electrodes, which exhibited J_{CO} around 300 mA·cm^{-2} at cell overpotential, η_{cell}, around 1.4 V. While using synthesized 3DOM $Sn_{0.3}Ti_{0.7}O_2$ electrode, AFT cell achieved production rate toward CO over 4.0 mL/min/cm^2 and partial current density for CO (J_{CO}) exceeding 300 mA·cm^{-2} at the cell overpotential around 1.2 V. J_{CO} is ten times higher than the H-cell with the same FE_{CO} (> 90%).

5.2. Results and Discussion

H-cell is composed of planar electrodes immersed in an aqueous electrolyte saturated with CO_2 and reactions take place at the electrode/electrolyte interfaces (**Figure 5-1a**). The oxygen evolution reaction (OER) occurs at the opposite anode side, with the ionic species transferring between that anolyte and catholyte compartments separated by an ion-exchange membrane between two potentially different electrolytes. As shown in **Figure 5-1b**, the CO_2 saturated electrolyte flow by the electrodes in both the PEM based cells. The electron passes over the electrodes through the clamps at the end of the channel ribs. While the flow-by GDE cell typically composed by six parts in the cathode sides (**Figure 5-1c**): (1) Flow channel; (2) Current collector; (3) Gas diffusion layer (GDL); (4) Catalyst layer (catalysts were usually adhered or deposited onto GDL); (5) Electrolyte; (6) Ion exchange membrane. The as a gas stream flows past a porous electrode, and CO_2 diffuses to the TBP, where it dissolves and reacts at the nearby catalyst sites. In this setup, all the mass transport occurs mostly by diffusion, and there is an additional concentration loss due to the partition of CO_2 into the liquid electrolyte.

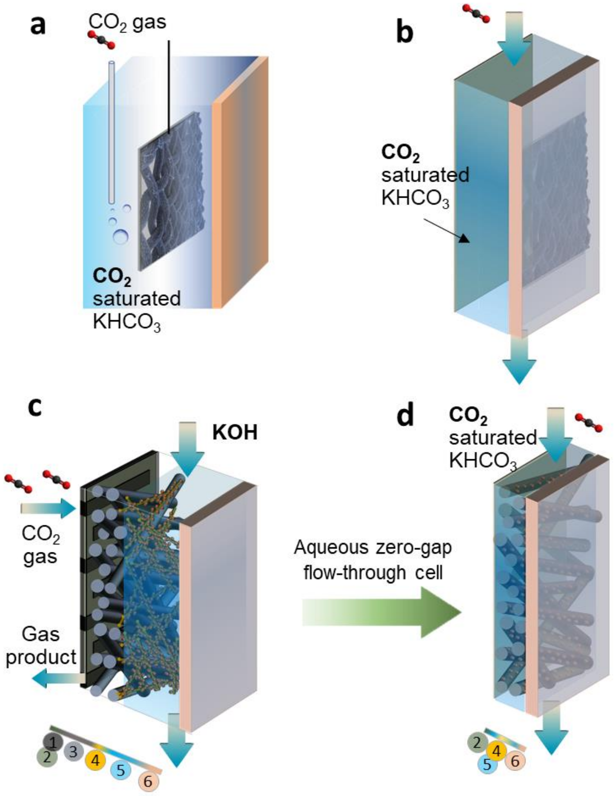

Figure 5-1. Schematic of (a) H-cell, (b) PEM based flow-by cell, (c) GDE based flow-by cell, and (d) proposed aqueous flow-through cell (AFT cell). The meaning of number in c and d: (1) Flow channel; (2) Current collector; (3) Gas diffusion layer; (4) Catalyst layer; (5) Electrolyte; (6) Ion exchange membrane.

Regrading the AFT cell (**Figure 5-1d**), the catalysts were attached to the carbon fibers (CF) and distributed throughout the whole CF substrate instead of spray-coating the catalyst ink onto a specific surface GDL. Additionally, the porous structure and mechanical strength of CF could contribute to the long-time stability under high current densities.[249-250] The aqueous electrolyte flow through the CF subtract, the dissolved CO_2 and HCO_3^-, which acted as the carbon source, accompanied by proton crossed through the thin BL and reached the electrode/electrolyte interfaces. The CF also has high electronic conductivity to provide sufficient electrons. Thus, the AFT cell decoupled CO_2, ion, and electron transport and circumvents the need for triple-phase boundaries by delivering dissolved CO_2 directly the solid catalysts.

The experimental results clearly showed the superiority of AFT cell. As the LSV curves shown (**Figure 5-2a**), the AFT cell had a higher current density (e.g. -340 $mA\cdot cm^{-2}$ at 2.8 V from **Table S5-1**) and a lower the onset cell potential (1.6 V) compared with GDE cell (e.g. -110 $mA\cdot cm^{-2}$ at 2.8 V, while onset cell potential is 2.0 V from **Table S5-2**). From **Figure 5-2b**, the FE_{CO} is also a little higher for AFT cells, although with the same materials as the cathode. This might be attributed to the rapid mass transport and abundant CO_2 supply. FE for formate in both AFT cell and GDE cells were less than 5% (**Table S5-1**, **S5-2**), so they were not shown in **Figure 5-2b.**

While the most plausible reaction pathway is usually identified from the quantum-chemical calculation of the lowest free-energy pathway, this approach sometimes can be misleading when coverages of adsorbed species determined for alternative mechanism differ significantly,[234] since elementary reaction rates depend on the product of the rate coefficient and the coverage of species involved in the reactions.[141, 251-253] Moreover, cathode polarization and local species distributions can influence the kinetics of CO_2RR. Given the architectures of the flow by and flow through setups, the BL thicknesses were the major difference as shown in **Figure 5-3a**. To further prove the maximum rate of CO_2 consumption over the cathode increases inversely with the BL thickness, as assumed for a diffusion-limited process,[87, 91] multiscale simulations (**Figure 5-3b**) were performed. A 1D diffusion/transport model with considering bubble break-off and growth was solved to quantify the BL thickness, and through COMSOL where a 2D reaction/diffusion model was built to unmask the species distribution in the BL.

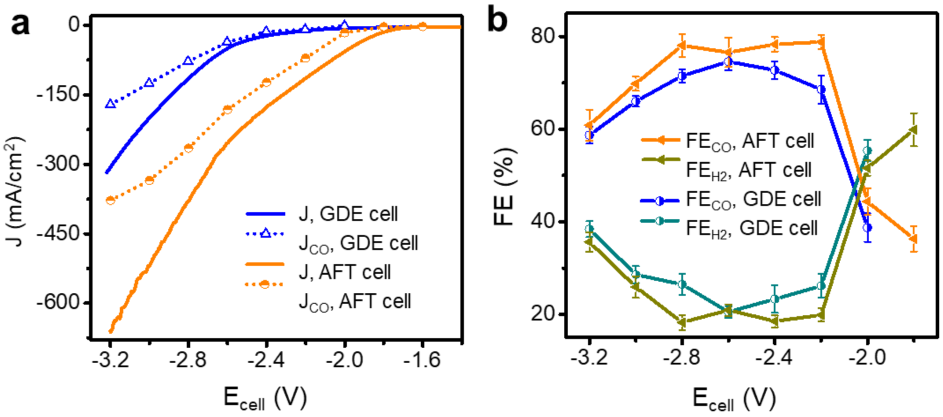

Figure 5-2. (a) LSV curves and partial current density of CO (J_{CO}) for GDE cell and AFT cell, respectively. (b) FE of CO and H_2 under different cell voltages.

From the 1D diffusion/transport model (**Figure 5-3c**), we can find the BL thickness for H-cell is highly correlated with current density. This is caused by the thick BL and limited mass transport. With a higher current density, more CO and H_2 bubbles were released,[87] which is further lowers the BL thickness and promoted the transports to some degree. Nevertheless, the current density of such systems is limited significantly by poor mass transport to the cathode due to the low diffusivity and solubility of CO_2 in water and the thickness of the mass-transfer BL near the electrode that is typically 60 to 160 µm.[91]

As can be observed in **Figure 5-3d**, the Ag NP/CF shows an outstanding J_{co} compared with state-of-the-art catalysts tested in different types of flow cells, especially at larger cell potentials. The production rate of CO at E_{cell} = 3.2V is quite high (e.g. 5.3 mL/min/cm^2 in **Table S5-1**). The performance of Ag NP in [4] was tested under high alkaline (1.0 M KOH) flow cells.[254] In this kind of cell, strongly acidic or alkaline electrolytes, with high ionic conductivities (such as 1 M H_2SO_4 or 1 M KOH) and unity transference numbers for protons or hydroxide ions, are used to minimize the resistive losses and concentration overpotentials in the system.[255] Although they provide higher current densities (CD) and energy efficiencies (EE), they suffer from carbonate salt precipitation in the stagnant pores of the GDE, moreover, in KOH electrolyte, CO_2 is parasitically converted to bicarbonate.[9, 80] Meanwhile, contacting with strongly acidic or alkaline electrolytes presents significant challenges to the stability of some prospective catalysts and expensive nanomaterials, which limit the potential system scalability.[255]

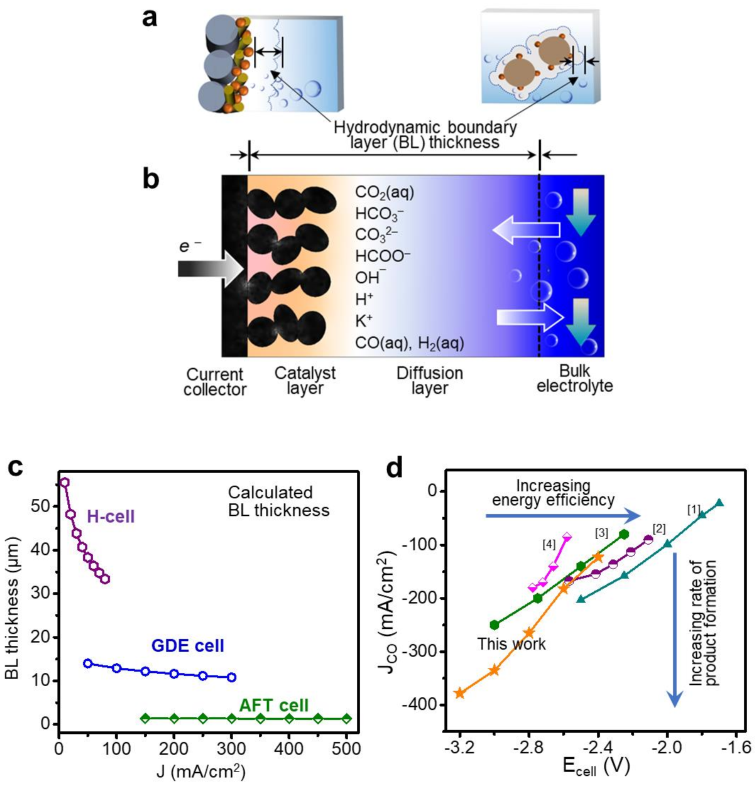

Figure 5-3. (a) Comparison of hydrodynamic boundary layer (BL) thickness between flow-by and flow-through setups, respectively. (b) Schematic of 2D reaction/diffusion model. (d) Calculated BL thickness of H-cell, GDE cell, and AFT cell through the 1D diffusion/transport model. (d) J_{CO} as a function of E_{cell} for state-of-the-art catalysts in CO_2-to-CO flow cell. [1] MWNT/PyPBI/Au, P. Kenis et al. ACS Energy Lett., 2018.[80] [2] Molecular catalyst, CoPc; C. Berlinguette et al. Science, 2019.[62] [3] Ag NP, 1.0M KOH, P. Kenis et al. Phys. Chem. Chem. Phys., 2016.[254] [4] Ni single atoms, H. Wang et al., Energy Environ. Sci, 2018.[61]

As reported GDE cells gave higher current densities and some research ascribed this high CD to the crucial role of gas-phase CO_2 instead of dissolved CO_2. Nonetheless, at 298 K and 1 atm pressure, the gas-phase concentration of CO_2 is 42 mM, which is only 30% higher than that of dissolved CO_2 (33 mM).[256] The critical role of GDE might not be caused by gas-phase CO_2, which cannot account for the order of magnitude increase in current density observed experimentally. Additionally, recent experimental and theoretical work has demonstrated the importance of water and hydrated cations on the elementary processes involved in CO_2RR.[89, 257] Thus, A. Weber et al.[256] pointed out that although CO_2 is supplied to the GDE from the gas phase, the reactant at the catalyst site is still dissolved CO_2. Besides the importance of dissolved CO_2, the HCO_3^- ion in the electrolyte also contributes and involves CO_2RR due to rapid dissolution and equilibration reactions, which is also reported as the primary carbon source for formate production during CO_2 electroreduction in the literature.[64, 76, 154, 175] Therefore, it's calling for a re-thinking of carbon sources in CO_2RR, which is highly susceptible to concentration polarization, wherein Faradaic processes induce concentration gradients near the electrode surface.[91]

The local environment near the catalyst layer, which is a function of the operating conditions, affects cell performance. This conjecture is corroborated by our 2D reaction/diffusion models, in which both CO_2 and HCO_3^- contributed to the CO_2RR. **Figure 5-4a** and **b** show the concentration of dissolved CO_2 and HCO_3^- in the electrolyte as functions of BL thickness and consumed as the carbon source. Noticeably, AFT cell has the highest CO_2 concentration at the surface of the electrodes due to enhanced mass transfer from the convective flow through the electrode. On the other hand, HCO_3^- concentration is the lowest. This further leads to increased pH values because of coupled buffer reactions (SI). Additionally, a relatively high alkaline region (pH around 9) is also beneficial for the catalytic activation of CO_2 in the electrolyte.[80, 93] Based on the crucial role of HCO_3^- and rapid dissolution and equilibration reactions, in the future pure gas-phase CO_2 stream for the subsequent electrolysis reaction might not be required. The carbonate electrolyte can be easily used to concentrated atmospheric CO_2 at a lower concentration.[10]

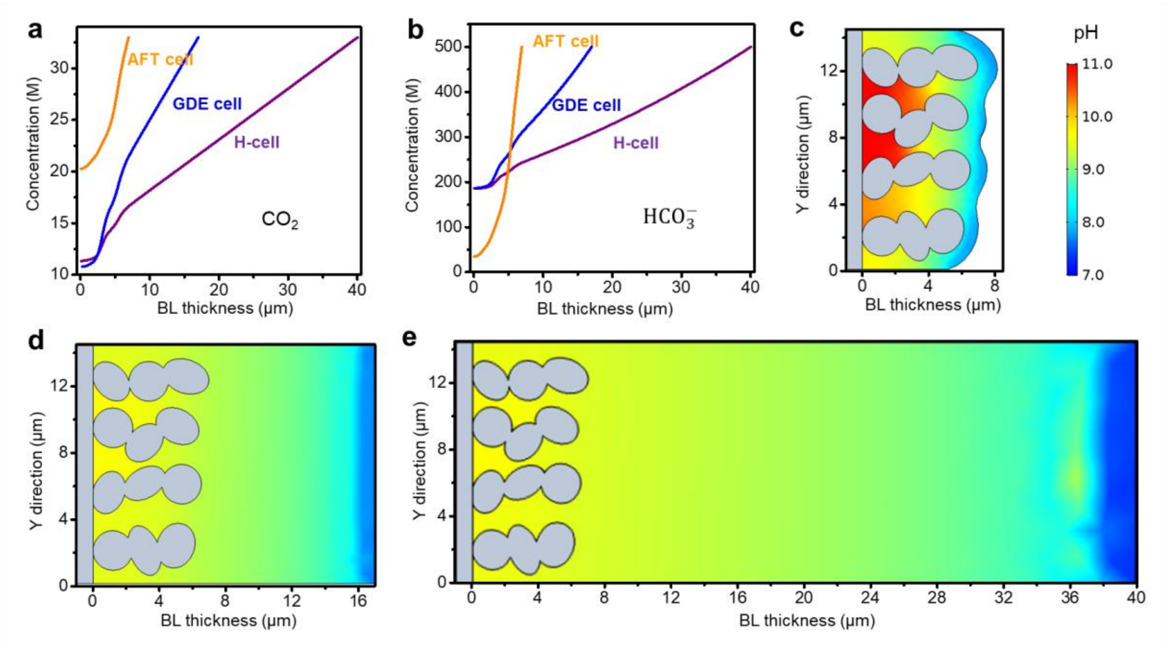

Figure 5-4. Calculated (a) dissolved CO_2 and HCO_3^- concentration linear distribution in AFT cell, GDE cell, and H-cell at the same overpotential. Calculated dissolved CO_2 concentration domain distribution in (c) AFT cell, (d) GDE cell, and (e) H-cell. (d, e) have the same legend in (c). Simulated results are derived from the 2D reaction/diffusion model.

We also prepared cathodes based on the high-performance 3DOM Sn-Ti-O ternary materials reported in **Chapter 4** and tested in the AFT cell. The performance comparison of Sn-Ti-O electrodes between AFT cell and H-cell is shown in **Figure 5-5**. AFT cell achieved production rate toward CO around 7.0 mL/min/cm^2, which is ten times higher than the H-cell under the conditions of almost the same FE. The FE_{CO} kept over 90% at E_{cell} from -2.4V to -2.8V, while the J_{CO} increased from -150 mA/cm^2 to -300 mA/cm^2. Notwithstanding, FE_{CO} dropped from >90 to ~80% when J_{CO} was increased from -300 mA/cm^2 to -475 mA/cm^2. This drop-in selectivity might be due to a suppression of proton concentration at higher current densities[62] or resulted from mass transport limitations of CO_2.[86]

Due to the tight assembly of AFT cell, it’s difficult to add a reference electrode so **Figure 5-5a** & **c** are shown as a function of cell voltages, while it is potentials vs. RHE for the H-cell. P. Kenis et al.[80] showed strict theoretical onset potentials for flow cells and made a comparison table of cell voltages and potentials vs. RHE, in which it showed the difference between these two was about 1.45 V at lower potentials, while 1.80V at higher potentials. Thus, the E_{cell} at -2.8V was around -1.0 V vs. RHE in the AFT cell.

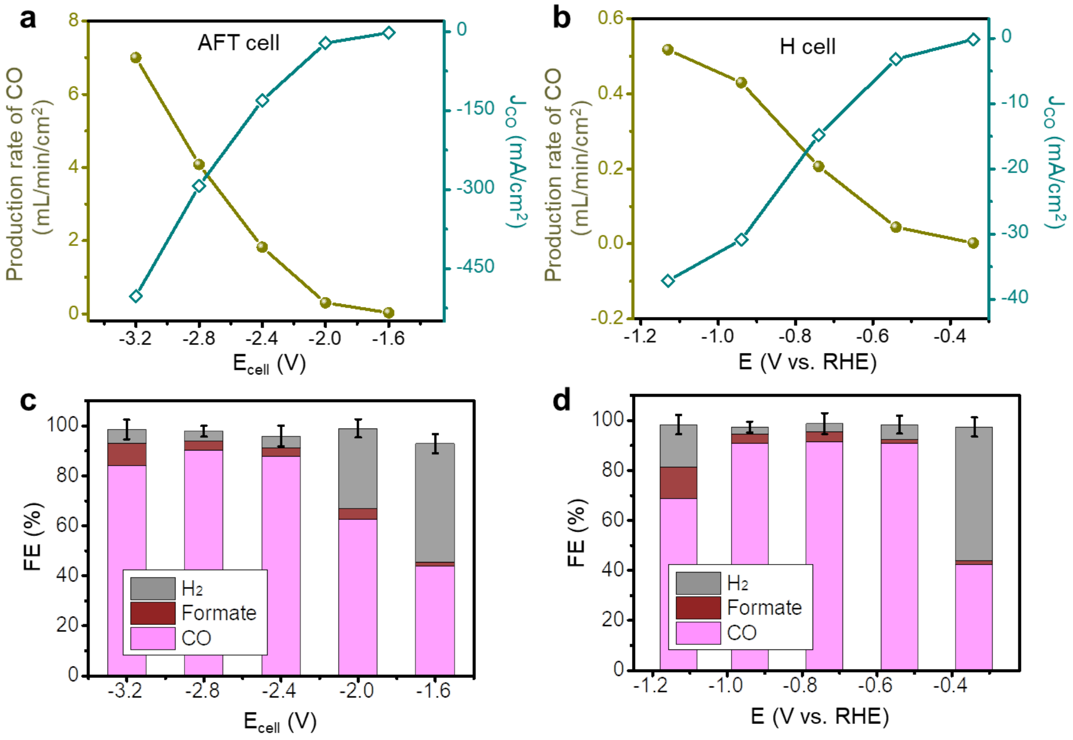

Figure 5-5. Production rate and partial current density of CO generated on Sn-Ti-O electrode in (a) AFT cell and (b) H-cell at a series of potentials. FE toward CO, formate, and H_2 on Sn-Ti-O electrode in (c) AFT cell and (d) H-cell at a series of potentials.

The main drawback of this flow-through approach is the higher pumping costs of forcing liquid electrolyte through the electrode, but this would likely be a small fraction of the operating cost of a CO_2RR system which would be dominated by the electrolysis power. This problem can be largely circumvented by using an interdigitated flow field by creating relatively short flow paths. Ultimately, there is an optimization to be performed to balance the enhanced performance with the increased pumping costs.

5.3. Conclusions

In summary, despite the remaining process engineering challenges, AFT cell showed remarkably improved activities for continuous CO_2RR, offering the opportunity to lower the high cell potentials required to drive CO_2RR at meaningful rates of production. A 10-fold BL thickness decrease from flow-by to flow-through is an important contributor to the 10-fold increase in catalyst activity. Computational transport models also described the dependence of species concentration distributions on BL, which are in good agreement with and elucidate the hypothesis of BL effect on the cells' performance. With both CO_2 and $\mathrm{HCO_3^-}$ acted as the carbon sources, AFT cell technology provides an alternative approach to adsorb atmospheric CO_2 into carbonate electrolyte for CO_2RR without using pure gas-phase CO_2 stream in practical applications. This concept sheds light on the engineering of electrodes and electrolytic cells for electrochemistry processes and energy storage systems.

5.4. Experimental Methods

5.4.1. Flow Cell Experiments

Ag NP/CF has fabricated through drop-casting the nanoparticles ink onto the commercial carbon fabric (CF, Fuel Cell Earth) at a loading of 4 $mg \cdot cm^{-2}$. The NP ink was prepared by dispersing 20 mg of Ag NPs (< 100 nm particle size, Sigma-Aldrich) and 80 μl Nafion solution (5 wt%) in 1 ml water-ethanol solution with a volume ratio of 1:1 and sonicated for 1 hour prior to drop-casting.

The Sn-Ti-O electrode was prepared through the same procedure by the reported materials in Chapter 4.

The AFT cell (**Figure 5-6**) consists of emerged as-synthesized Ag NP/CF cathode, a commercial Pt/C-CF anode, and Nafion 117 membrane to separate the two compartments and prevent re-oxidation of CO/ formate at the anode. The geometric active surface area of both anode and cathode are 1 cm^2 (inset of **Figure 5-6a**). The catalyst electrodes, Nafion 117 membrane, and Pt/C-CF anode was positioned and compressed together using PTFE spacers such that a liquid electrolyte could be introduced into the cathode and anode chambers, respectively. The catholyte (200ml) was 0.5 M $KHCO_3$ with continuous CO_2 bubbling, and it is circulated using a peristaltic pump. The anolyte (200ml) was also CO_2 saturated 0.5 M $KHCO_3$ and it is circulated to using a peristaltic pump. Gas products are collected from the top of the catholyte chamber for further analyses as discussed in Chapter 4. Liquid products are quantified through the NMR spectrum after the reactions.

The CO_2RR was performed for 20 minutes at various potentials in the electrolyte. The electrochemical measurements were carried out using a potentiostat (BioLogic VSP300). The current densities reported in this work were normalized to the geometric surface area. The CO_2RR test was repeated two times, and the results presented are the averaged values. All the experiments were conducted under ambient pressure and at room temperature (23 °C). The onset cell potential was defined as the potential at which the geometry current density was around 4 $mA\cdot cm^{-2}$ higher than the initially stabilized current density.

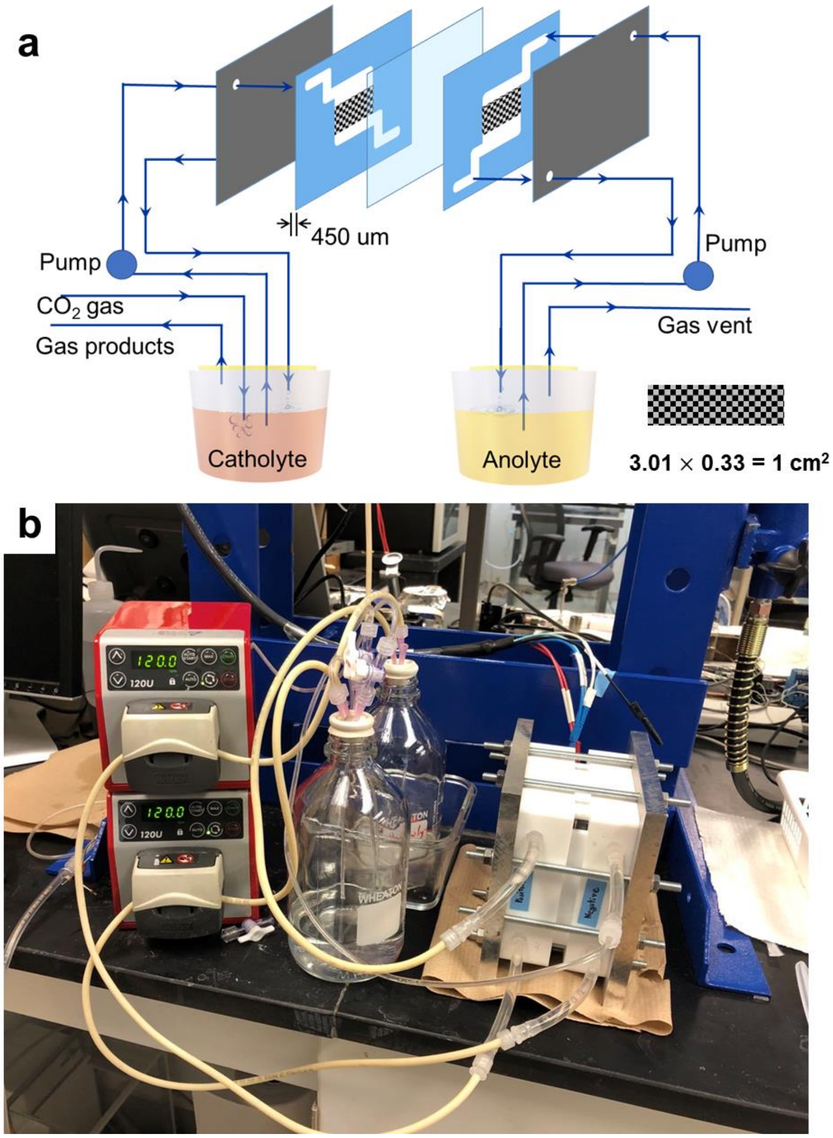

Figure 5-6. (a) Process flow diagram of the AFT cell setup. The separated electrolyte chambers decouple the cell sizes and electrolyte capacities. (b) AFT cell testing station.

As a comparison, a GDE cell (**Figure 5-7**) modified from a Proton exchange membrane (PEM) fuel cell was used for CO_2RR tested, which has two additional buffer layers for the electrolyte flowing by the catalyst Layer. **Figure 5-7d** from reported results[29] give us a schematic of buffer layers. Both Ag NP/CF cathode and Pt/C-CF anode are circular with a diameter of 2 cm. Pure CO_2 gas flow by the gas diffusion layer at the flow rate of 20 sccm. The rest of the procedures are the same at the AFT cell.

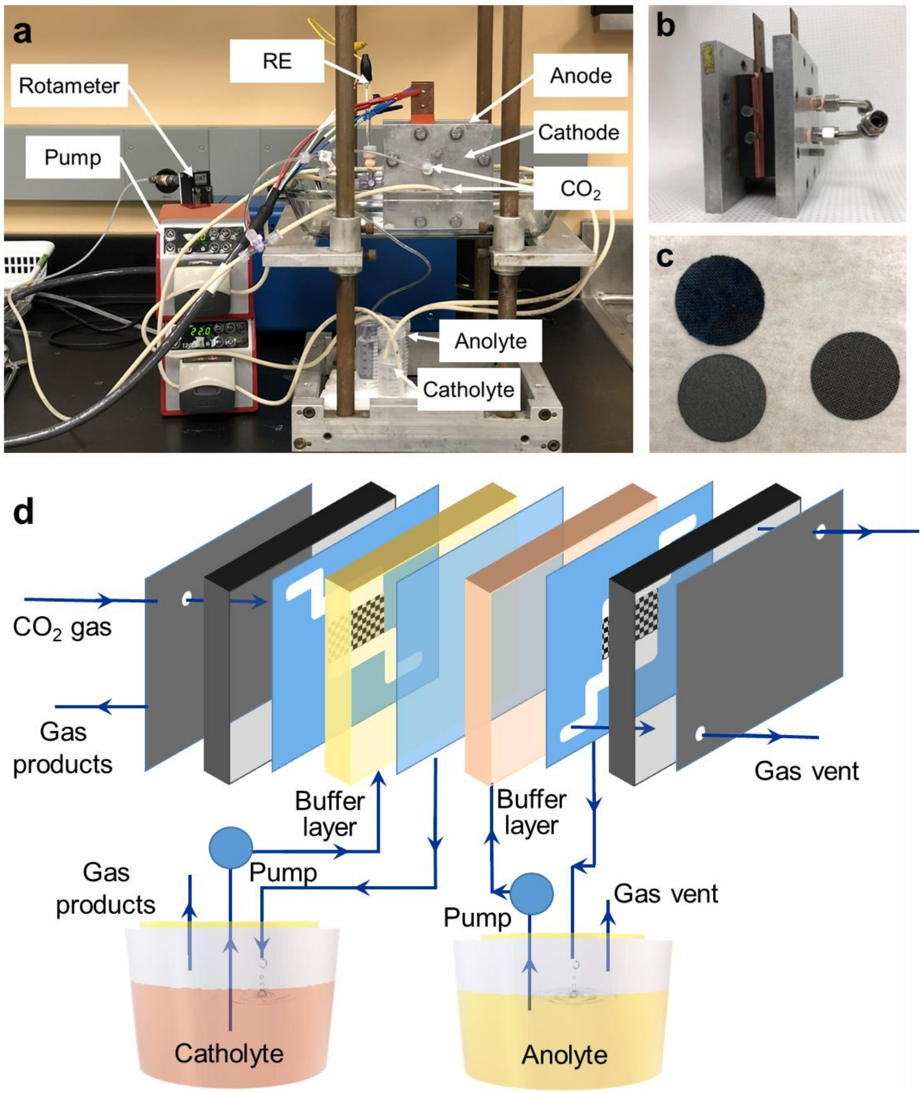

Figure 5-7. (a) GDE cell testing station. (b) GDE cell setup. (c) Electrodes used in the GDE cell. (d) A schematic of the full GDE cell featuring a buffer layer of circulating liquid-phase electrolyte.

5.4.2. 1D Diffusion/Transport Model

Although the electrode kinetics of the catalyst are important, the catalyst's interaction with the electrolyte is also crucial for CO_2RR. The thickness of the diffusion layer can be calculated as a function of the gas-evolving current density, bubble departure diameter, pressure, and fluid flow velocity. The hydrodynamic BL thickness is modeled as a 1-D diffusion system to reduce the complex multi-phases transportations with the formation and evolutions of the bubble. In the BL concentration gradient is characterized by adjacent to the electrode and BL thickness directly correlates to the reaction's limiting current densities and polarization losses.

The variation in the partial currents for H_2 and CO are direct results of the variation in the mass transfer boundary layer thickness at the cathode surface and are not due to changes in the bulk CO_2 concentration.[91] Here, we showed the calculations of BL thickness for three mostly used setups: H-cell, GDE cell (flow-through system), and AFT cell (flow-by system).

The thickness of the diffusion layer, δ_{i}, is assumed equal to the diffusivity of the species of interest, D_{i} (here is the dissolved CO_2), divided by the mass transfer coefficient, k_{m}, present in the system:

$$\delta_{\mathrm{i}} = \frac{D_{\mathrm{i}}}{k_{\mathrm{m}}} \qquad \text{(Eqn. 5-1)}$$

Convective bulk flow and bubble-induced momentum from gas-evolution are contributed to the mass transfer coefficient, k_{m}. So k_{m} is the summary of mass transfer coefficient for convective flow, k_{conv}, and mass transfer coefficient for bubble-induced momentum from gas-evolution, k_{bubble}:

$$k_{\mathrm{m}} = k_{\mathrm{conv}} + k_{\mathrm{bubble}} \qquad \text{(Eqn. 5-2)}$$

Mass transfer coefficient for convective flow can be found using the correlation where the average mass transfer coefficient calculated from the Sherwood number (*Sh*) is

$$k_{\mathrm{conv}} = \frac{\overline{Sh} D_{\mathrm{i}}}{L} = \frac{0.664 D_{\mathrm{i}}}{L} Re_L^{0.5} Sc^{0.333} \qquad \text{(Eqn. 5-3)}$$

$$Re_L = \frac{\rho N D^2}{\mu} = \frac{\rho V D}{\mu}, \qquad \text{(Eqn. 5-4)}$$

where the characteristic length, *L*, is the length of the electrode in direction of flow. The Reynolds number can be approximated from the stirring or flow conditions of the electrolyte. *D* in Eqn. 5-4 is the hydrodynamic diameter of the electrodes. In the H-cell setup, the planar electrodes were immersed in the electrolyte with the electrolyte stirred by a stirred bar. *N* in Eqn. 5-4 is the stirring speed, which is 600 rpm here. Regarding the GDE cell and AFT cell, the Reynolds number can be calculated by the flow rate, *V*.

As suggested by T. Burdyny and et al.,[87] to describe the effects of bubble break-off where fluid immediately replaces the departing bubble, Sh_1,[258] the Rousar correlation, and to describe the combined effects of bubble growth and wake flow, Sh_2, Vogt's correlation for low electrode bubble coverage ($\Theta < 0.5$).

$$k_{\mathrm{bubble}} = \frac{Sh_{\mathrm{bubble}}\, D_{\mathrm{i}}}{d_{\mathrm{b}}} \qquad \text{(Eqn. 5-5)}$$

$$Sh_{\mathrm{bubble}} = (Sh_1^2 + Sh_2^2)^{0.5} \qquad \text{(Eqn. 5-6)}$$

$$Sh_1 = \sqrt{\frac{12}{\pi} Re_{\mathrm{G}}^{0.5} Sc^{0.5} \Theta^{0.5}} \qquad \text{(Eqn. 5-7)}$$

$$Sh_2 = \frac{2}{\sqrt{5}} Re_{\mathrm{G}}^{0.5} Sc^{0.34} \left(1 - \frac{\sqrt{8}}{3}\frac{R_{\mathrm{a}}}{R}\Theta^{0.5}\right)(1+\Theta) \qquad \text{(Eqn. 5-8)}$$

where Θ represents the fraction of the electrode area covered by bubbles during a bubble's residence time and thus not available for reactions. The ratio R_{a}/R in Eqn. 5-8 represents the ratio of the inactive electrode area below a nucleated bubble as it grows. The Reynolds and Schmidt numbers for gas-evolution are described as:

$$Re_{\mathrm{G}} = \frac{V_{\mathrm{gas}}}{A}\frac{d_{\mathrm{b}}}{v} \qquad \text{(Eqn. 5-9)}$$

$$Sc = \frac{v}{D} \qquad \text{(Eqn. 5-10)}$$

For gas-evolution the bubble departure diameter, d_b, acts as the characteristic length scale, while v is the kinematic viscosity of the electrolyte. The bubble departure diameter is an experimentally determined quantity that depends upon the morphology and wettability of a catalyst's surface.

The volume flux from gas-evolution (V_gas/A) represents the effective gas velocity and is defined as:

$$\frac{V_\mathrm{gas}}{A} = \frac{j_\mathrm{evolved}}{n_\mathrm{e}F}\frac{RT}{P} \qquad \text{(Eqn. 5-11)}$$

5.4.3. 2D Reaction/Diffusion Model

Figure 5-1e shows a schematic of the electrochemical cell for CO_2RR, especially in the BL. The cell has a well-mixed catholyte region with the species: dissolved CO_2, bicarbonate anions ($\mathrm{HCO_3^-}$), carbonate anions ($\mathrm{CO_3^{2-}}$), formate anions ($\mathrm{HCOO^-}$), hydroxide anions ($\mathrm{OH^-}$), protons ($\mathrm{H^+}$), potassium cations (K^+), and CO and H_2. Electroneutrality is assumed for all ionic species. The 2D model assumes the concentration of these species only varied in the BL.

Three electrochemical charge-transfer reactions occur on the surface of CF:

$$\mathrm{CO_2(aq) + H_2O + 2e^- \rightarrow CO + 2OH^-} \qquad \text{(Rxn. 5- 1)}$$

$$\mathrm{CO_2(aq) + H_2O + 2e^- \rightleftharpoons HCOO^- + OH^-} \qquad \text{(Rxn. 5- 2)}$$

$$\mathrm{2H_2O + 2e^- \rightleftharpoons H_2 + 2OH^-} \qquad \text{(Rxn. 5- 3)}$$

The CO, $\mathrm{HCOO^-}$ and H_2 localized current densities are calculated using Tafel kinetics:

$$i_\mathrm{loc,CO} = i_\mathrm{0,\,CO}\,(\frac{C_\mathrm{CO_2}}{C_\mathrm{CO_2,ref}})exp(\frac{-2F\,\beta_\mathrm{CO}\,\eta_\mathrm{CO}}{RT}) \qquad \text{(Eqn. 5-12)}$$

$$i_\mathrm{loc,HCOO^-} = i_\mathrm{0,HCOO^-}\,(\frac{C_\mathrm{CO_2}}{C_\mathrm{CO_2,ref}})exp(\frac{-2F\,\beta_\mathrm{HCOO^-}\,\eta_\mathrm{HCOO^-}}{RT}) \qquad \text{(Eqn. 5-13)}$$

$$i_{\mathrm{loc,H_2}} = i_{0,\,\mathrm{H_2}}\,(\frac{C_{\mathrm{H^+}}}{C_{\mathrm{H^+,ref}}})exp(\frac{-2F\,\beta_{\mathrm{H^+}}\,\eta_{\mathrm{H^+}}}{RT}) \qquad \text{(Eqn. 5-14)}$$

The exchange-current densities, $i_{0,k}$, and transfer coefficients, β_k, are obtained through the Tafel slops from experimental testing (**Table 5-1**, **Figure 5-6**). k represents above different electrochemical reactions. Reference concentrations for both CO_2 and H^+ are taken as the same as the initial values. The surface overpotential is given by:

$$\eta_k = (\phi_{\mathrm{s}} - \phi_{\mathrm{l}}) - (U_k^{\mathrm{o}} - \frac{2.303RT}{F}\mathrm{pH}) \qquad \text{(Eqn. 5-15)}$$

where U_k^{o} is the standard reduction potentials. [259] ϕ_{s} and ϕ_{l} are the electronic potential and ionic potential, respectively.

Table 5-1. Experimental data for the CO_2RR and HER reaction kinetics.

Reaction	Tafel Slope (mV·dec^{-1})	Intercept	$i_{0,k}$ (mA·cm^{-2})	β_k(-)	U_k^{o} (V)	$s_{j,k}$
CO formation	0.147	0.452	8.42×10^{-4}	-0.201	-0.109	+1
HCOOH formation	0.150	0.604	9.40×10^{-5}	-0.197	-0.03	+1
H_2 evolution	0.897	0.633	1.97×10^{-1}	-0.033	0	+1

Note: The performance data was collected with Ag NP/CF as the electrode in the H-cell. The Tafel slopes and intercepts are derived from **Figure 5-8**.

The charge-transfer reactions contribute to the source terms for gas-phase species H_2 and CO, as well as liquid-phase species $\mathrm{HCOO^-}$, H^+, and $\mathrm{OH^-}$ through:

$$R_{\mathrm{CT},j} = -M_j \sum_k \frac{s_{j,k} a_{\mathrm{v}} i_k}{n_k F} \qquad \text{(Eqn. 5-16)}$$

where F is Faraday's constant; n_k is the number of electrons transferred, which is 2 for all of three charge-transfer reactions; $s_{j,k}$ is the stoichiometric coefficient for species j in reaction k.

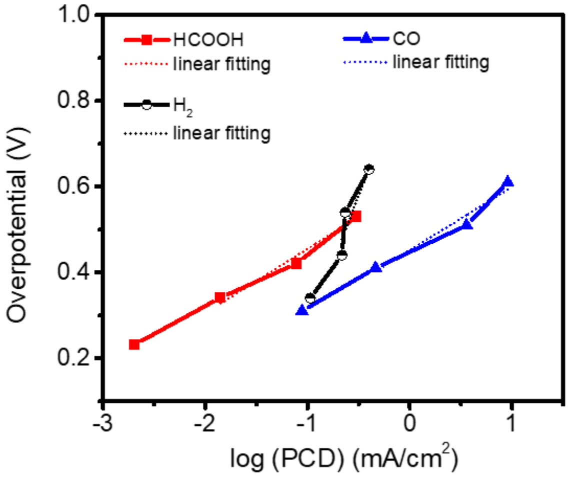

Figure 5-8. (a) Tafel analysis for CO, formate, and H_2 formation.

As CO_2 dissolved in the $KHCO_3$ solution, it readily reacts with water to form carbonic acid. While H_2CO_3 is weak, diprotic acid and can undergo two steps of ionization to form (bi)carbonates. All the buffer chemical equilibrium reactions are shown as following:

$$\mathrm{CO_2(aq) + H_2O \overset{k_1,k_{-1}}{\Longleftrightarrow} H^+ + HCO_3^-},\ \text{with } K_1 = 10^{-6.37} \qquad \text{(Rxn. 5- 4)}$$

$$\mathrm{HCO_3^- \overset{k_2,k_{-2}}{\Longleftrightarrow} H^+ + CO_3^{2-}},\ \text{with } K_2 = 10^{-10.32}\ \mathrm{M} \qquad \text{(Rxn. 5- 5)}$$

$$\mathrm{CO_2(aq) + OH^- \overset{k_3,k_{-3}}{\Longleftrightarrow} HCO_3^-},\ \text{with } K_3 = K_1/K_w \qquad \text{(Rxn. 5- 6)}$$

$$\mathrm{HCO_3^- + OH^- \overset{k_4,k_{-4}}{\Longleftrightarrow} H_2O + CO_3^{2-}},\ \text{with } K_4 = K_2/K_w \qquad \text{(Rxn. 5- 7)}$$

$$\mathrm{H_2O \overset{k_w,k_{-w}}{\Longleftrightarrow} H^+ + OH^-},\ \text{with } K_w = 10^{-14}\ \mathrm{M}^2 \qquad \text{(Rxn. 5- 8)}$$

The mass balance for each species within the Bl can be written as:

$$\nabla \cdot n_j = R_{CT,j} + R_{B,j} \qquad \text{(Eqn. 5-17)}$$

where n_j is the mass flux of species j; $R_{CT,i}$and $R_{B,i}$ are the volumetric charge-transfer reactions and homogeneous bulk reactions source term, respectively.

The flux of aqueous species can be broken into diffusion and migration terms (Nernst–Planck):

$$n_j = -D_j \rho_l \nabla \omega_j + z_j u_j F \rho_{\mathrm{l}} \omega_j \nabla \phi_{\mathrm{l}} \tag{Eqn. 5-18}$$

where z_j is the charge and u_j is the mobility of aqueous species j, respectively, ρ_l is the liquid density, and ϕ_{l} is the liquid-phase potential. The liquid-phase effective diffusivity and mobility are shown in **Table 5-2** from Reference[234, 256].

Table 5-2. Model constant parameters.[234]

Species	Diffusion Coefficient, D_j, ($10^{-9}\cdot m^2\cdot s^{-1}$)	Mobility, u_j, ($10^{-7}\cdot m^2\cdot V^{-1}\cdot s^{-1}$)
CO_2 (aq)	1.91	-
$\mathrm{HCO_3^-}$	1.185	0.462
$\mathrm{CO_3^{2-}}$	0.923	0.359
$\mathrm{HCOO^-}$	1.493 [260]	Nernst–Einstein relationship (u_j=D_j^{eff}/RT)
$\mathrm{H^+}$	9.311	3.626
$\mathrm{OH^-}$	5.273	2.054
K^+	1.957	0.762
CO	2.23 [261]	-
H_2	6.30 [262]	-

Charge conservation and Ohm's law govern the electronic potential ϕ_{s} and current i_s:

$$\nabla \cdot i_{\mathrm{s}} = -\nabla \cdot i_{\mathrm{l}} = -r_{\mathrm{v}} \sum_k i_k \tag{Eqn. 5-19}$$

$$i_{\mathrm{s}} = -\sigma_{\mathrm{s,m}}^{\mathrm{eff}} \nabla \phi_{\mathrm{s}} \tag{Eqn. 5-20}$$

where i_{s} is the current density in the solid phase, i_{l} is the current density in the liquid phase, i_k is the local partial current density for reaction k, $\sigma_{\mathrm{s,m}}^{\mathrm{eff}}$ is the effective electrical conductivity of the solid material in medium m, corrected by the Bruggeman correlation. r_{v} is the roughness coefficient, which is a fitting parameter for tuning the current density as the same as the experimental data in H-cell. The value of it is 35 for all the three models with different Bl thicknesses.

Source terms resulting from homogenous bulk reactions for the aqueous species j are calculated using apparent rate constants measured by R. Zeebe et al (Eqn. 5-21).[263] Forward reaction-rate constants for equation n, k_n, are listed in **Table 5-3** and reverse reaction rate constants are calculated from Eqn. 5-22, in which K_n is the equilibrium constants from reported data.[256]

$$R_{\mathrm{B},j} = M_j \sum_{n} s_j\left(k_n \prod_{s_j<0} c_j - k_{-n} \prod_{s_j>0} c_j\right) \qquad \text{(Eqn. 5-21)}$$

$$k_{-n} = \frac{k_n}{K_n} \qquad \text{(Eqn. 5-22)}$$

The electrolyte potential is set to zero as a reference. The electronic potential is set as -1.2 V vs. RHE at the catalyst surface. At the end of BL, the concentration of species is set as the same as the bulk electrolyte.

The above equations are solved using COMSOL Multiphysics 5.3. Other model parameters are listed in **Table 5-3**.

Table 5-3. Model constant parameters.

Parameter	Value	Unit
T, temperature	293.15	K
P, pressure	1	atm
The diameter of carbon fiber	1.2	µm
Width of the electrode	2	µm
Width of electrolyte	BL thickness, from E.2.	µm
Height	14.5	µm
CO_2(aq) reference conc. (concentration)	33	mM
CO_3^{2-} reference conc.	0.001	mM
$HCOO^-$ reference conc.	0.001	mM
HCO_3^- reference conc.	500	mM
K^+ reference conc.	500	mM

CO reference conc.	0.01	mM
H_2 reference conc.	0.01	mM
pH	7.2	
r_{v}, roughness coefficient	35	Fitting parameter
k_1	3.71×10^{-2}	s^{-1}
k_2	59.44	s^{-1}
k_3	2.23×10^{3}	$L \cdot mol^{-1} \cdot s^{-1}$
k_4	6.0×10^{9}	$L \cdot mol^{-1} \cdot s^{-1}$

5.5. Supporting Tables

Table S5-1. CO_2RR performance of AFT cell with Ag NP/CF cathode.

Cell voltages	FE(CO)	FE(H_2)	FE(HCOOH)	Current density, J	Partial current density, J_{CO}	Production rate of CO
(V)	(% ± 3.5%)	(% ± 3.5%)	(% ± 3.5%)	(mA cm^{-2})	(mA cm^{-2})	(mL/min/cm^2)
-1.6	30	67	2.9	-3.8	-2.5	0.02
-1.8	36	60	2.2	-8.8	-3.2	0.04
-2	44	52	3.3	-36.3	-16.1	0.22
-2.2	79	20	1.2	-89.9	-70.9	0.99
-2.4	78	19	2.3	-157.2	-123.1	1.72
-2.6	77	21	2.6	-237.9	-182.2	2.54
-2.8	78	18	3.1	-339.8	-265.3	3.70
-3	70	26	4.0	-479.8	-335.0	4.67
-3.2	61	36	3.7	-621.5	-378.3	5.27

Table S5-2. CO_2RR performance of GDE cell with Ag NP/CF cathode.

Cell voltages	FE(CO)	FE(H_2)	FE(HCOOH)	Current density, J	Partial current density, J_{CO}	Production rate of CO
(V)	(% ± 3.5%)	(% ± 3.5%)	(% ± 3.5%)	(mA cm^{-2})	(mA cm^{-2})	(mL/min/cm^2)

-2	39	55	2.5	-3.4	-1.3	0.02
-2.2	69	26	1.8	-13.2	-9.1	0.13
-2.4	73	23	3.8	-19.2	-14.0	0.19
-2.6	75	21	2.6	-49.3	-36.8	0.51
-2.8	71	26	1.4	-109.6	-78.4	1.09
-3	66	29	3.7	-190.7	-125.9	1.75
-3.2	59	38	0.4	-292.0	-171.4	2.39

Table S5-3. CO_2RR performance of H-cell with 3DOM $Sn_{0.3}Ti_{0.7}O_2$ ternary cathode.

Potential	FE(CO)	FE(HCOOH)	FE(H_2)	Current density, J	Partial current density, J_{CO}	Production rate of CO
(V vs. RHE)	(% ± 2.5%)	(% ± 2.0%)	(% ± 2.5%)	(mA cm^{-2})	(mA cm^{-2})	(mL/min/cm^{2})
-0.34	42	1.5	54	0.4	0.2	0.002
-0.54	91	1.6	6	3.5	3.2	0.04
-0.74	92	4.0	3	16.2	14.8	0.21
-0.94	91	3.8	3	34.0	30.9	0.43
-1.13	69	12.6	17	54.1	37.2	0.52

Table S5-4. CO_2RR performance of AFT cell with 3DOM $Sn_{0.3}Ti_{0.7}O_2$ ternary cathode.

Cell voltages	FE(CO)	FE(HCOOH)	FE(H_2)	Current density, J	Partial current density, J_{CO}	Production rate of CO
(V)	(% ± 2.5%)	(% ± 2.0%)	(% ± 2.5%)	(mA cm^{-2})	(mA cm^{-2})	(mL/min/cm^{2})
-1.6	44	2	47	-4.9	-2.2	0.03
-2	63	4	32	-34.6	-21.6	0.30
-2.4	88	3	5	-148.8	-130.8	1.82
-2.8	90	4	4	-324.3	-293.0	4.08
-3.2	84	9	5	-597.1	-502.5	7.00

Chapter 6. Conclusion and Perspectives

6.1. Conclusions

Electrochemical conversion of CO_2 provides an unprecedented opportunity to develop new clean technologies and further tackle the issue of global warming. In this thesis, approaches to nanostructured catalysts (**Chapters 3**, **4**) along with electrodes and cell design (**Chapter 5**) were successfully implemented to perform efficient CO_2RR.

In **Chapter 3**, a bimetallic Bi-Sn catalyst was synthesized and investigated for a highly efficient conversion of CO_2 into formate. Due to the orbital interaction of Bi-Sn and Sn-O, the composition and morphology optimized electrode (Bi-Sn/CF) led to 96 % Faradaic efficiency for formate at -1.14 V vs. RHE with a high production rate of 0.74 mmol h^{-1} cm^{-2}. Additionally, the electrode demonstrated excellent durability of 100 hours of continuous operation with no degradation in current density and Faradaic efficiency. The present work gives suggestions to the rational design of catalysts for future CO_2RR studies by presenting a facile synthesis technique for nanostructured bimetallic catalysts.

In **Chapter 4**, 3DOM ternary Sn-Ti-O catalysts were successfully produced, representing a simple but highly effective artificial material for CO_2RR. DFT calculations combined with different physical and chemical characterizations revealed the nature of the electron density reconfiguration among Sn, Ti, and O atoms. A balance between exposure of active sites and the degree of electron density shift was imperative for achieving a highly efficient 3DOM catalyst. In particular, it was inferred that the crucial electron density transfer from Ti to Sn enabled the dissociative adsorption of COOH*, directly producing CO with cathodic energy efficiency over 71.5%. The existence of Ti not only effectively creates an electron bank that contributes to the activation of catalytic reactions, but it also plays an important role in strengthening the 3DOM structure in order to maintain a high EE_{ca} for over 200 hours within a wide potential window. Insights gained through these quantitative analyses of electron density configuration can be further exploited as promising design principles for high-performance catalysts, making the electrochemical process more sustainable for practical applications.

In **Chapter 5**, a prototype aqueous flow-through (AFT) cell was developed that showed remarkably improved activities for continuous CO_2RR, offering the opportunity to lower the high cell potentials required to drive CO_2RR chemistry at meaningful rates of production. A 10-fold BL thickness decrease from flow-by to flow-through is an important contributor to the 10-fold increase in catalyst activity. Computational transport models also described the dependence of species concentration distributions on BL, which are in good agreement with the hypothesis of BL effect on the cells' performance. With both CO_2 and HCO_3^- acting as the carbon sources, AFT cell technology provides an alternative approach to adsorb gaseous CO_2 from flue gases into carbonate electrolyte for CO_2RR without using pure gas-phase CO_2 stream in practical applications. This concept sheds light on the engineering of electrodes and electrolytic cells for electrochemistry processes and energy storage systems.

6.2. Recommended Future Work

Based on the results of the studies conducted in this thesis research, the following recommendations are proposed for future work.

Further development of the catalytic and functional materials. Until very recently, with the emergence of nanotechnology, the development of various types of catalysts to efficiently improve the performance of CO_2RR materials become of great importance. Binary and ternary composites have shown to be an effective method, nevertheless, there are still plenty of unknown combinations and effects of combination styles, e.g. ensemble and segregated mixing, ordering patterns.

Utilization of advanced characterization technologies. More advanced in-operando spectroscopy and characterization technologies, such as XAFS, attenuated total reflection surface-enhanced infrared absorption spectroscopy (ATR-SEIRAS), high angle annular dark-field STEM (HAADF-STEM), can be employed to facilitate the development revelation of the materials evolutions during CO_2RR with a collision of the electrons, ions, reaction species.

Comprehensive multiscale simulation. The present 2D simulation model only considered the diffusion and reactions in the BL. However, the gas bubbles formation, evolution, and break also play a role in the coverage ratio on the surface of the catalyst. The further realistic model is required to consider bubbles evolutions and transports. Additionally, the carbon fibers are too simple in the present 2D model and might lose some essential transport features related to the structures.

Investigations on a more realistic CO_2***RR system.*** To make the CO_2RR processes having a wide application and achieving the industrial target, the electrolytic cell is required to utilize CO_2 in low concentrations, even directive use CO_2 in the atmosphere and from the waste gas in other industrial processes, such as cement or power plants. Once the CO_2RR systems meet the requirements to couple with the established industrial processes and smart energy-grids, this system can lead us to the end of the tunnel and to approach the goal of carbon capture and utilization.

References

(1) Hori, Y.; Wakebe, H.; Tsukamoto, T.; Koga, O., ***Electrochim. Acta***, **1994**, *39*, 11, 1833-1839.

(2) Kenis, P. J. A.; Dibenedetto, A.; Zhang, T., ***ChemPhysChem***, **2017**, *18*, 22, 3091-3093.

(3) Kuhl, K. P.; Cave, E. R.; Abram, D. N.; Jaramillo, T. F., ***Energy Environ. Sci.***, **2012**, *5*, 5, 7050-7059.

(4) Azuma, M.; Hashimoto, K.; Hiramoto, M.; Watanabe, M.; Sakata, T., ***J. Electrochem. Soc.***, **1990**, *137*, 6, 1772-1778.

(5) Álvarez, A.; Bansode, A.; Urakawa, A.; Bavykina, A. V.; Wezendonk, T. A.; Makkee, M.; Gascon, J.; Kapteijn, F., ***Chem. Rev.***, **2017**, *117*, 14, 9804-9838.

(6) Liu, M.; Pang, Y.; Zhang, B.; De Luna, P.; Voznyy, O.; Xu, J.; Zheng, X.; Dinh, C. T.; Fan, F.; Cao, C.; de Arquer, F. P. G.; Safaei, T. S.; Mepham, A.; Klinkova, A.; Kumacheva, E.; Filleter, T.; Sinton, D.; Kelley, S. O.; Sargent, E. H., ***Nature***, **2016**, *537*, 7620, 382-386.

(7) Gao, S.; Lin, Y.; Jiao, X.; Sun, Y.; Luo, Q.; Zhang, W.; Li, D.; Yang, J.; Xie, Y., ***Nature***, **2016**, *529*, 7584, 68-71.

(8) Chen, L.; Guo, S. X.; Li, F.; Bentley, C.; Horne, M.; Bond, A. M.; Zhang, J., ***ChemSusChem***, **2016**, *9*, 11, 1271-1278.

(9) Dinh, C.-T.; Burdyny, T.; Kibria, M. G.; Seifitokaldani, A.; Gabardo, C. M.; de Arquer, F. P. G.; Kiani, A.; Edwards, J. P.; De Luna, P.; Bushuyev, O. S.; Zou, C.; Quintero-Bermudez, R.; Pang, Y.; Sinton, D.; Sargent, E. H., ***Science***, **2018**, *360*, 6390, 783-787.

(10) Li, Y. C.; Lee, G.; Yuan, T.; Wang, Y.; Nam, D.-H.; Wang, Z.; García de Arquer, F. P.; Lum, Y.; Dinh, C.-T.; Voznyy, O.; Sargent, E. H., ***ACS Energy Lett.***, **2019**, *4*, 6, 1427-1431.

(11) Pan, Y.; Lin, R.; Chen, Y.; Liu, S.; Zhu, W.; Cao, X.; Chen, W.; Wu, K.; Cheong, W.; Wang, Y.; Zheng, L.; Luo, J.; Lin, Y.; Liu, Y.; Liu, C.; Li, J.; Lu, Q.; Chen, X.; Wang, D.; Peng, Q.; Chen, C.; Li, Y., ***J. Am. Chem. Soc.***, **2018**, *140*, 12, 4218-4221.

(12) Duan, Y. X.; Meng, F. L.; Liu, K. H.; Yi, S. S.; Li, S. J.; Yan, J. M.; Jiang, Q., ***Adv. Mater.***, **2018**, *30*, 14, 1706194.

(13) Mikkelsen, M.; Jørgensen, M.; Krebs, F. C., ***Energy Environ. Sci.***, **2010**, *3*, 1, 43-81.

(14) Wang, W.; Himeda, Y.; Muckerman, J. T.; Manbeck, G. F.; Fujita, E., ***Chem. Rev.***, **2015**, *115*, 23, 12936-12973.

(15) Jouny, M.; Luc, W.; Jiao, F., ***Ind. Eng. Chem. Res.***, **2018**, *57*, 6, 2165-2177.

(16) Sordakis, K.; Tang, C.; Vogt, L. K.; Junge, H.; Dyson, P. J.; Beller, M.; Laurenczy, G., ***Chem. Rev.***, **2017**, *118*, 372-433.

(17) Kattel, S.; Liu, P.; Chen, J. G., ***J. Am. Chem. Soc.***, **2017**, *139*, 29, 9739-9754.

(18) Ju, W.; Bagger, A.; Hao, G.-P.; Varela, A. S.; Sinev, I.; Bon, V.; Roldan Cuenya, B.; Kaskel, S.; Rossmeisl, J.; Strasser, P., ***Nat. Commun.***, **2017**, *8*, 1, 944.

(19) Cano, Z. P.; Banham, D.; Ye, S.; Hintennach, A.; Lu, J.; Fowler, M.; Chen, Z., ***Nat. Energy***, **2018**, *3*, 4, 279-289.

(20) Amini, K.; Gostick, J.; Pritzker, M. D., ***Adv. Funct. Mater.***, **2020**, 1910564.

(21) Li, G.; Lu, F.; Dou, X.; Wang, X.; Luo, D.; Sun, H.; Yu, A.; Chen, Z., ***J. Am. Chem. Soc.***, **2020**, *142*, 7, 3583-3592.

(22) Seh, Z. W.; Kibsgaard, J.; Dickens, C. F.; Chorkendorff, I.; Nørskov, J. K.; Jaramillo, T. F., ***Science***, **2017**, *355*, 6321.

(23) Endrődi, B.; Bencsik, G.; Darvas, F.; Jones, R.; Rajeshwar, K.; Janáky, C., ***Prog. Energ. Combust.***, **2017**, *62*, 133-154.

(24) Zhang, L.; Zhao, Z. J.; Gong, J., ***Angew. Chem. Int. Edit.***, **2017**, *56*, 38, 11326-11353.

(25) Currie, R.; Mottaghi-Tabar, S.; Zhuang, Y.; Simakov, D. S. A., ***Ind. Eng. Chem. Res.***, **2019**, *58*, 29, 12964-12980.

(26) Currie, R.; Fowler, M. W.; Simakov, D. S. A., ***Chem. Eng. J.***, **2019**, *372*, 1240-1252.

(27) Liu, C.; Gallagher, J. J.; Sakimoto, K. K.; Nichols, E. M.; Chang, C. J.; Chang, M. C.; Yang, P., ***Nano Lett.***, **2015**, *15*, 5, 3634-3639.

(28) Mondal, M.; Khanra, S.; Tiwari, O.; Gayen, K.; Halder, G., ***Environ. Prog. Sustain.***, **2016**, *35*, 6, 1605-1615.

(29) Wu, J.; Risalvato, F. G.; Sharma, P. P.; Pellechia, P. J.; Ke, F. S.; Zhou, X. D., ***J. Electrochem. Soc.***, **2013**, *160*, 9, F953-F957.

(30) Ren, B.; Croiset, E.; Ricardez–Sandoval, L., ***J. Catal.***, **2020**, *383*, 273-282.

(31) Ren, B.; Li, J.; Wen, G.; Ricardez−Sandoval, L.; Croiset, E., ***J. Phys. Chem. C***, **2018**, *122*, 37, 21151-21161.

(32) Chen, Y.; Kanan, M. W., ***J. Am. Chem. Soc.***, **2012**, *134*, 4, 1986-1989.

(33) Li, F.; MacFarlane, D. R.; Zhang, J., ***Nanoscale***, **2018**, *10*, 14, 6235-6260.

(34) Duan, X.; Xu, J.; Wei, Z.; Ma, J.; Guo, S.; Wang, S.; Liu, H.; Dou, S., ***Adv. Mater.***, **2017**, *29*, 41, 1701784.

(35) Centi, G.; Quadrelli, E. A.; Perathoner, S., ***Energy Environ. Sci.***, **2013**, *6*, 6, 1711-1731.

(36) Del Castillo, A.; Alvarez-Guerra, M.; Solla-Gullón, J.; Sáez, A.; Montiel, V.; Irabien, A., ***Appl. Energy***, **2015**, *157*, 5.746, 165-173.

(37) Zhou, Q.; Liu, L.; Croiset, E.; Tan, Z.; Liu, Q.; Yang, J., ***RSC Adv.***, **2019**, *9*, 35, 20075-20086.

(38) Li, Y.; Wang, L. a.; Tan, Z.; Zhang, Z.; Hu, X., ***Sep. Purif. Technol.***, **2019**, *219*, 47-54.

(39) Greenwood, N.; Earnshaw, A., *Chemistry of the Elements 2nd Edition*. Butterworth-Heinemann: 1997.

(40) Baturina, O. A.; Lu, Q.; Padilla, M. A.; Xin, L.; Li, W.; Serov, A.; Artyushkova, K.; Atanassov, P.; Xu, F.; Epshteyn, A., ***ACS Catal.***, **2014**, *4*, 10, 3682-3695.

(41) Zhuang, T.-T.; Liang, Z.-Q.; Seifitokaldani, A.; Li, Y.; De Luna, P.; Burdyny, T.; Che, F.; Meng, F.; Min, Y.; Quintero-Bermudez, R.; Dinh, C. T.; Pang, Y.; Zhong, M.; Zhang, B.; Li, J.; Chen, P.-N.; Zheng, X.-L.; Liang, H.; Ge, W.-N.; Ye, B.-J.; Sinton, D.; Yu, S.-H.; Sargent, E. H., ***Nat. Catal.***, **2018**, *1*, 6, 421-428.

(42) Wang, Y.; Wang, Z.; Dinh, C.-T.; Li, J.; Ozden, A.; Golam Kibria, M.; Seifitokaldani, A.; Tan, C.-S.; Gabardo, C. M.; Luo, M.; Zhou, H.; Li, F.; Lum, Y.; McCallum, C.; Xu, Y.; Liu, M.; Proppe, A.; Johnston, A.; Todorovic, P.; Zhuang, T.-T.; Sinton, D.; Kelley, S. O.; Sargent, E. H., ***Nat. Catal.***, **2019**, *3*, 2, 98-106.

(43) Ren, D.; Deng, Y.; Handoko, A. D.; Chen, C. S.; Malkhandi, S.; Yeo, B. S., ***ACS Catal.***, **2015**, *5*, 5, 2814-2821.

(44) Ross, M. B.; Dinh, C. T.; Li, Y.; Kim, D.; De Luna, P.; Sargent, E. H.; Yang, P., ***J. Am. Chem. Soc.***, **2017**, *139*, 27, 9359-9363.

(45) Ma, M.; Djanashvili, K.; Smith, W. A., ***Angew. Chem. Int. Edit.***, **2016**, *55*, 23, 6680 – 6684.

(46) Kuhl, K. P.; Hatsukade, T.; Cave, E. R.; Abram, D. N.; Kibsgaard, J.; Jaramillo, T. F., ***J. Am. Chem. Soc.***, **2014**, *136*, 40, 14107-14113.

(47) Huang, J.; Mensi, M.; Oveisi, E.; Mantella, V.; Buonsanti, R., ***J. Am. Chem. Soc.***, **2019**, *141*, 6, 2490-2499.

(48) Wang, Y.; Cao, L.; Libretto, N. J.; Li, X.; Li, C.; Wan, Y.; He, C.; Lee, J.; Gregg, J.; Zong, H.; Su, D.; Miller, J. T.; Mueller, T.; Wang, C., ***J. Am. Chem. Soc.***, **2019**, *141*, 42, 16635-16642.

(49) Li, Q.; Fu, J.; Zhu, W.; Chen, Z.; Shen, B.; Wu, L.; Xi, Z.; Wang, T.; Lu, G.; Zhu, J.; Sun, S., ***J. Am. Chem. Soc.***, **2017**, *139*, 12, 4290-4293.

(50) Luc, W.; Collins, C.; Wang, S.; Xin, H.; He, K.; Kang, Y.; Jiao, F., ***J. Am. Chem. Soc.***, **2017**, *139*, 5, 1885-1893.

(51) Kim, D.; Xie, C.; Becknell, N.; Yu, Y.; Karamad, M.; Chan, K.; Crumlin, E. J.; Nørskov, J. K.; Yang, P., ***J. Am. Chem. Soc.***, **2017**, *139*, 24, 8329-8336.

(52) Wang, X.; Wang, Z.; García de Arquer, F. P.; Dinh, C.-T.; Ozden, A.; Li, Y. C.; Nam, D.-H.; Li, J.; Liu, Y.-S.; Wicks, J.; Chen, Z.; Chi, M.; Chen, B.; Wang, Y.; Tam, J.; Howe, J. Y.; Proppe, A.; Todorović, P.; Li, F.; Zhuang, T.-T.; Gabardo, C. M.; Kirmani, A. R.; McCallum, C.; Hung, S.-F.; Lum, Y.; Luo, M.; Min, Y.; Xu, A.; O'Brien, C. P.; Stephen, B.; Sun, B.; Ip, A. H.; Richter, L. J.; Kelley, S. O.; Sinton, D.; Sargent, E. H., ***Nat. Energy***, **2020**.

(53) García de Arquer, F. P.; Dinh, C.-T.; Ozden, A.; Wicks, J.; McCallum, C.; Kirmani, A. R.; Nam, D.-H.; Gabardo, C.; Seifitokaldani, A.; Wang, X.; Li, Y. C.; Li, F.; Edwards, J.; Richter, L. J.; Thorpe, S. J.; Sinton, D.; Sargent, E. H., ***Science***, **2020**, *367*, 6478, 661-666.

(54) Yang, F.; Ma, X.; Cai, W.-B.; Song, P.; Xu, W., ***J. Am. Chem. Soc.***, **2019**, *141*, 51, 20451-20459.

(55) Nam, D.-H.; Bushuyev, O. S.; Li, J.; De Luna, P.; Seifitokaldani, A.; Dinh, C.-T.; García de Arquer, F. P.; Wang, Y.; Liang, Z.; Proppe, A. H.; Tan, C. S.; Todorović, P.; Shekhah, O.; Gabardo, C. M.; Jo, J. W.; Choi, J.; Choi, M.-J.; Baek, S.-W.; Kim, J.; Sinton, D.; Kelley, S. O.; Eddaoudi, M.; Sargent, E. H., ***J. Am. Chem. Soc.***, **2018**, *140*, 36, 11378-11386.

(56) Liu, M.; Liu, M.; Wang, X.; Kozlov, S. M.; Cao, Z.; De Luna, P.; Li, H.; Qiu, X.; Liu, K.; Hu, J.; Jia, C.; Wang, P.; Zhou, H.; He, J.; Zhong, M.; Lan, X.; Zhou, Y.; Wang, Z.; Li, J.; Seifitokaldani, A.; Dinh, C. T.; Liang, H.; Zou, C.; Zhang, D.; Yang, Y.; Chan, T.-S.; Han, Y.; Cavallo, L.; Sham, T.-K.; Hwang, B.-J.; Sargent, E. H., ***Joule***, **2019**, *3*, 7, 1703-1718.

(57) Liu, S.; Tao, H.; Zeng, L.; Liu, Q.; Xu, Z.; Liu, Q.; Luo, J. L., ***J Am Chem Soc***, **2017**, *139*, 6, 2160-2163.

(58) Zhang, S.; Kang, P.; Meyer, T. J., ***J. Am. Chem. Soc.***, **2014**, *136*, 5, 1734-1737.

(59) Han, N.; Ding, P.; He, L.; Li, Y.; Li, Y., ***Adv. Energy Mater.***, **2019**, *10*, 11, 1902338.

(60) Daiyan, R.; Saputera, W. H.; Masood, H.; Leverett, J.; Lu, X.; Amal, R., ***Adv. Energy Mater.***, **2020**, *10*, 11, 1902106.

(61) Jiang, K.; Siahrostami, S.; Zheng, T.; Hu, Y.; Hwang, S.; Stavitski, E.; Peng, Y.; Dynes, J.; Gangisetty, M.; Su, D.; Attenkofer, K.; Wang, H., ***Energy Environ. Sci.***, **2018**, *11*, 4, 893-903.

(62) Ren, S.; Joulié, D.; Salvatore, D.; Torbensen, K.; Wang, M.; Robert, M.; Berlinguette, C. P., ***Science***, **2019**, *365*, 6451, 367-369.

(63) Abdinejad, M.; Seifitokaldani, A.; Dao, C.; Sargent, E. H.; Zhang, X.-a.; Kraatz, H. B., ***ACS Appl. Energy Mater.***, **2019**, *2*, 2, 1330-1335.

(64) Ross, M. B.; De Luna, P.; Li, Y.; Dinh, C.-T.; Kim, D.; Yang, P.; Sargent, E. H., ***Nat. Catal.*** , **2019**, *2*, 8, 648-658.

(65) Yoo, J. S.; Christensen, R.; Vegge, T.; Nørskov, J. K.; Studt, F., ***ChemSusChem***, **2016**, *9*, 4, 358-363.

(66) Guan, C.; Zhang, D.; Pan, Y.; Iguchi, M.; Ajitha, M. J.; Hu, J.; Li, H.; Yao, C.; Huang, M.-H.; Min, S.; Zheng, J.; Himeda, Y.; Kawanami, H.; Huang, K.-W., ***Inorg. Chem.***, **2017**, *56*, 1, 438-445.

(67) Yan, J. M.; Li, S. J.; Yi, S. S.; Wulan, B. R.; Zheng, W. T.; Jiang, Q., ***Adv. Mater.***, **2018**, *30*, 12, 1703038.

(68) Wang, L. L.; Cao, X. L.; Wang, Y. J.; Li, Q. X., ***Catalysts***, **2015**, *5*, 3, 1388-1398.

(69) Abraham, B. G.; Maniam, K. K.; Kuniyil, A.; Chetty, R., ***Fuel Cells***, **2016**, *16*, 5, 656-661.

(70) Hoffman, Z. B.; Gray, T. S.; Moraveck, K. B.; Gunnoe, T. B.; Zangari, G., ***ACS Catal.***, **2017**, *7*, 8, 5381-5390.

(71) Kim, S.; Dong, W. J.; Gim, S.; Sohn, W.; Park, J. Y.; Yoo, C. J.; Jang, H. W.; Lee, J., ***Nano Energy***, **2017**, *39*, 44-52.

(72) Koh, J. H.; Won, D. H.; Eom, T.; Kim, N.-K.; Jung, K. D.; Kim, H.; Hwang, Y. J.; Min, B. K., ***ACS Catal.***, **2017**, *7*, 8, 5071-5077.

(73) Su, P.; Xu, W.; Qiu, Y.; Zhang, T.; Li, X.; Zhang, H., ***ChemSusChem***, **2018**, *11*, 848 –853.

(74) Zheng, X.; De Luna, P.; García de Arquer, F. P.; Zhang, B.; Becknell, N.; Ross, M. B.; Li, Y.; Banis, M. N.; Li, Y.; Liu, M.; Voznyy, O.; Dinh, C. T.; Zhuang, T.; Stadler, P.; Cui, Y.; Du, X.; Yang, P.; Sargent, E. H., ***Joule***, **2017**, *1*, 4, 794-805.

(75) Lei, F.; Liu, W.; Sun, Y.; Xu, J.; Liu, K.; Liang, L.; Yao, T.; Pan, B.; Wei, S.; Xie, Y., ***Nat. Commun.***, **2016**, *7*, 1, 12697

(76) Bai, X.; Chen, W.; Zhao, C.; Li, S.; Song, Y.; Ge, R.; Wei, W.; Sun, Y., ***Angew. Chem. Int. Edit.***, **2017**, *129*, 12387–12391.

(77) Alayoglu, S.; Nilekar, A. U.; Mavrikakis, M.; Eichhorn, B., ***Nat. Mater.***, **2008**, *7*, 333.

(78) Back, S.; Kim, J. H.; Kim, Y. T.; Jung, Y., ***ACS Appl. Mater. Inter.***, **2016**, *8*, 35, 23022-23027.

(79) De Luna, P.; Hahn, C.; Higgins, D.; Jaffer, S. A.; Jaramillo, T. F.; Sargent, E. H., ***Science***, **2019**, *364*, 6438, eaav3506.

(80) Verma, S.; Hamasaki, Y.; Kim, C.; Huang, W.; Lu, S.; Jhong, H.-R. M.; Gewirth, A. A.; Fujigaya, T.; Nakashima, N.; Kenis, P. J. A., ***ACS Energy Lett.***, **2018**, *3*, 1, 193-198.

(81) Gu, J.; Heroguel, F.; Luterbacher, J.; Hu, X., ***Angew. Chem. Int. Edit.***, **2018**, *57*, 11, 2943-2947.

(82) Gu, J.; Hsu, C.-S.; Bai, L.; Chen, H. M.; Hu, X., ***Science***, **2019**, *364*, 6445, 1091-1094.

(83) Huang, Z.-F.; Song, J.; Du, Y.; Xi, S.; Dou, S.; Nsanzimana, J. M. V.; Wang, C.; Xu, Z. J.; Wang, X., ***Nat. Energy***, **2019**, *4*, 4, 329-338.

(84) Deng, W.; Zhang, L.; Li, L.; Chen, S.; Hu, C.; Zhao, Z. J.; Wang, T.; Gong, J., ***J. Am. Chem. Soc.***, **2019**, *141*, 7, 2911-2915.

(85) Liang, Z.-Q.; Zhuang, T.-T.; Seifitokaldani, A.; Li, J.; Huang, C.-W.; Tan, C.-S.; Li, Y.; De Luna, P.; Dinh, C. T.; Hu, Y.; Xiao, Q.; Hsieh, P.-L.; Wang, Y.; Li, F.; Quintero-Bermudez, R.; Zhou, Y.; Chen, P.; Pang, Y.; Lo, S.-C.; Chen, L.-J.; Tan, H.; Xu, Z.; Zhao, S.; Sinton, D.; Sargent, E. H., ***Nat. Commun.***, **2018**, *9*, 1, 3828.

(86) Wen, G.; Lee, D. U.; Ren, B.; Hassan, F. M.; Jiang, G.; Cano, Z. P.; Gostick, J.; Croiset, E.; Bai, Z.; Yang, L.; Chen, Z., ***Adv. Energy Mater.***, **2018**, *8*, 31, 1802427.

(87) Burdyny, T.; Graham, P. J.; Pang, Y.; Dinh, C.-T.; Liu, M.; Sargent, E. H.; Sinton, D., ***ACS Sustain. Chem. Eng.*** , **2017**, *5*, 5, 4031-4040.

(88) Higgins, D.; Hahn, C.; Xiang, C.; Jaramillo, T. F.; Weber, A. Z., ***ACS Energy Lett.***, **2018**, *4*, 1, 317-324.

(89) Singh, M. R.; Kwon, Y.; Lum, Y.; Ager, J. W.; Bell, A. T., ***J. Am. Chem. Soc.***, **2016**, *138*, 39, 13006-13012.

(90) Zheng, T.; Jiang, K.; Wang, H., ***Adv. Mater.***, **2018**, *30*, 48, 1802066.

(91) Clark, E. L.; Resasco, J.; Landers, A.; Lin, J.; Chung, L.-T.; Walton, A.; Hahn, C.; Jaramillo, T. F.; Bell, A. T., ***ACS Catal.***, **2018**, *8*, 7, 6560-6570.

(92) Zhu, D. D.; Liu, J. L.; Qiao, S. Z., ***Adv. Mater.***, **2016**, *28*, 18, 3423-3452.

(93) Li, J.; Chen, G.; Zhu, Y.; Liang, Z.; Pei, A.; Wu, C.-L.; Wang, H.; Lee, H. R.; Liu, K.; Chu, S.; Cui, Y., ***Nat. Catal.***, **2018**, *1*, 8, 592-600.

(94) Lin, R.; Guo, J.; Li, X.; Patel, P.; Seifitokaldani, A., ***Catalysts***, **2020**, *10*, 5, 473.

(95) Jiang, B.; Zhang, X. G.; Jiang, K.; Wu, D. Y.; Cai, W. B., ***J. Am. Chem. Soc.***, **2018**, *140*, 8, 2880-2889.

(96) Kibria, M. G.; Edwards, J. P.; Gabardo, C. M.; Dinh, C.-T.; Seifitokaldani, A.; Sinton, D.; Sargent, E. H., ***Adv. Mater.***, **2019**, *31*, 31, 1807166.

(97) Gabardo, C. M.; Seifitokaldani, A.; Edwards, J. P.; Dinh, C.-T.; Burdyny, T.; Kibria, M. G.; O'Brien, C. P.; Sargent, E. H.; Sinton, D., ***Energy Environ. Sci.***, **2018**, *11*, 9, 2531-2539.

(98) Won, D. H.; Choi, C. H.; Chung, J.; Chung, M. W.; Kim, E.-H.; Woo, S. I., ***ChemSusChem***, **2015**, *8*, 18, 3092-3098.

(99) Zhao, C.; Wang, J., ***Chem. Eng. J.***, **2016**, *293*, 161-170.

(100) Daiyan, R.; Lu, X.; Ng, Y. H.; Amal, R., ***Catal. Sci. Technol.***, **2017**, *7*, 12, 2542-2550.

(101) Pander, J. E.; Baruch, M. F.; Bocarsly, A. B., ***ACS Catal.***, **2016**, *6*, 11, 7824-7833.

(102) Zhao, Y.; Liang, J.; Wang, C.; Ma, J.; Wallace, G. G., ***Adv. Energy Mater.***, **2018**, *8*, 10, 1702524.

(103) Choi, S. Y.; Jeong, S. K.; Kim, H. J.; Baek, I. H.; Park, K. T., ***ACS Sustain. Chem. Eng.*** , **2016**, *4*, 3, 1311-1318.

(104) Fu, Y.; Li, Y.; Zhang, X.; Liu, Y.; Qiao, J.; Zhang, J.; Wilkinson, D. P., ***Appl. Energy***, **2016**, *175*, 5.746, 536-544.

(105) Li, Y.; Qiao, J.; Zhang, X.; Lei, T.; Girma, A.; Liu, Y.; Zhang, J., ***ChemElectroChem***, **2016**, *3*, 10, 1618-1628.

(106) Li, F.; Chen, L.; Knowles, G. P.; MacFarlane, D. R.; Zhang, J., ***Angew. Chem. Int. Edit.***, **2017**, *129*, 2, 520-524.

(107) DiMeglio, J. L.; Rosenthal, J., ***J. Am. Chem. Soc.***, **2013**, *135*, 24, 8798-8801.

(108) Medina-Ramos, J.; DiMeglio, J. L.; Rosenthal, J., ***J. Am. Chem. Soc.***, **2014**, *136*, 23, 8361-8367.

(109) Medina-Ramos, J.; Pupillo, R. C.; Keane, T. P.; DiMeglio, J. L.; Rosenthal, J., ***J. Am. Chem. Soc.***, **2015**, *137*, 15, 5021-5027.

(110) Zhang, Z.; Chi, M.; Veith, G. M.; Zhang, P.; Lutterman, D. A.; Rosenthal, J.; Overbury, S. H.; Dai, S.; Zhu, H., ***ACS Catal.***, **2016**, *6*, 9, 6255-6264.

(111) Wang, Y.; Zhou, J.; Lv, W.; Fang, H.; Wang, W., ***Appl. Surf. Sci.***, **2016**, *362*, 394-398.

(112) Irtem, E.; Andreu, T.; Parra, A.; Hernández-Alonso, M.; García-Rodríguez, S.; Riesco-García, J.; Penelas-Pérez, G.; Morante, J., ***J. Mater. Chem. A***, **2016**, *4*, 35, 13582-13588.

(113) Yadav, V.; Purkait, M., ***RSC Adv.***, **2015**, *5*, 84, 68551-68557.

(114) Won, D. H.; Choi, C. H.; Chung, J.; Chung, M. W.; Kim, E. H.; Woo, S. I., ***ChemSusChem***, **2015**, *8*, 18, 3092-3098.

(115) Du, D.; Lan, R.; Humphreys, J.; Sengodan, S.; Xie, K.; Wang, H.; Tao, S., ***ChemistrySelect***, **2016**, *1*, 8, 1711-1715.

(116) Zhang, R.; Lv, W.; Lei, L., ***Appl. Surf. Sci.***, **2015**, *356*, 24-29.

(117) Yu, J.; Liu, H.; Song, S.; Wang, Y.; Tsiakaras, P., ***Appl.Catal. A-Gen.***, **2017**, *545*, 159-166.

(118) Choi, S. Y.; Jeong, S. K.; Kim, H. J.; Baek, I.-H.; Park, K. T., ***ACS Sustain. Chem. Eng.*** , **2016**, *4*, 3, 1311-1318.

(119) Chang, K.; Wang, T.; Chen, J. G., ***Appl. Catal. B-Environ.***, **2017**, *206*, 704-711.

(120) Detweiler, Z. M.; White, J. L.; Bernasek, S. L.; Bocarsly, A. B., ***Langmuir***, **2014**, *30*, 25, 7593-7600.

(121) Lee, C. H.; Kanan, M. W., ***ACS Catal.***, **2014**, *5*, 1, 465-469.

(122) He, Z.; Shen, J.; Ni, Z.; Tang, J.; Song, S.; Chen, J.; Zhao, L., ***Catal. Commun.***, **2015**, *72*, 38-42.

(123) Kortlever, R.; Peters, I.; Koper, S.; Koper, M. T., ***ACS Catal.***, **2015**, *5*, 7, 3916-3923.

(124) Zhou, F.; Li, H.; Fournier, M.; MacFarlane, D. R., ***ChemSusChem***, **2017**, *10*, 7, 1509-1516.

(125) Min, X.; Kanan, M. W., ***J. Am. Chem. Soc.***, **2015**, *137*, 14, 4701-4708.

(126) Klinkova, A.; De Luna, P.; Dinh, C. T.; Voznyy, O.; Larin, E. M.; Kumacheva, E.; Sargent, E. H., ***ACS Catal.***, **2016**, *6*, 12, 8115-8120.

(127) Gao, S.; Jiao, X.; Sun, Z.; Zhang, W.; Sun, Y.; Wang, C.; Hu, Q.; Zu, X.; Yang, F.; Yang, S.; Liang, L.; Wu, J.; Xie, Y., ***Angew. Chem. Int. Edit.***, **2016**, *55*, 2, 698-702.

(128) Qu, K.; Zheng, Y.; Dai, S.; Qiao, S. Z., ***Nano Energy***, **2016**, *19*, 373-381.

(129) Zhang, S.; Kang, P.; Ubnoske, S.; Brennaman, M. K.; Song, N.; House, R. L.; Glass, J. T.; Meyer, T. J., ***J. Am. Chem. Soc.***, **2014**, *136*, 22, 7845-7848.

(130) Sreekanth, N.; Nazrulla, M. A.; Vineesh, T. V.; Sailaja, K.; Phani, K. L., ***Chem. Commun.***, **2015**, *51*, 89, 16061-16064.

(131) Kim, J.-H.; Woo, H.; Choi, J.; Jung, H.-W.; Kim, Y.-T., ***ACS Catal.***, **2017**, *7*, 3, 2101-2106.

(132) Humphrey, J. J. L.; Plana, D.; Celorrio, V.; Sadasivan, S.; Tooze, R. P.; RodrÃ-guez, P.; FermÃ-n, D. J., ***ChemCatChem***, **2016**, *8*, 5, 952-960.

(133) Firet, N. J.; Smith, W. A., ***ACS Catal.***, **2017**, *7*, 1, 606-612.

(134) Ma, S.; Luo, R.; Gold, J. I.; Yu, A. Z.; Kim, B.; Kenis, P. J. A., ***J. Mater. Chem. A***, **2016**, *4*, 22, 8573-8578.

(135) Hsieh, Y.; Senanayake, S. D.; Zhang, Y.; Xu, W.; Polyansky, D. E., ***ACS Catal.***, **2015**, *5*, 9, 5349-5356.

(136) Ma, S.; Sadakiyo, M.; Heima, M.; Luo, R.; Haasch, R. T.; Gold, J. I.; Yamauchi, M.; Kenis, P. J., ***J. Am. Chem. Soc.***, **2016**, *139*, 1, 47-50.

(137) Wu, J.; Yadav, R. M.; Liu, M.; Sharma, P. P.; Tiwary, C. S.; Ma, L.; Zou, X.; Zhou, X.-D.; Yakobson, B. I.; Lou, J.; Ajayan, P. M., ***ACS Nano***, **2015**, *9*, 5, 5364-5371.

(138) Yamamoto, T.; Tryk, D. A.; Fujishima, A.; Ohata, H., ***Electrochim. Acta***, **2002**, *47*, 20, 3327-3334.

(139) Jensen, S. H.; Sun, X.; Ebbesen, S. D.; Knibbe, R.; Mogensen, M., ***Int. J. Hydrog. Energy***, **2010**, *35*, 18, 9544-9549.

(140) Uhm, S.; Kim, Y. D., ***Curr. Appl. Phys.***, **2014**, *14*, 5, 672-679.

(141) Wu, K.; Birgersson, E.; Kim, B.; Kenis, P. J. A.; Karimi, I. A., ***J. Electrochem. Soc.***, **2015**, *162*, 1, F23-F32.

(142) Rosen, B. A.; Salehi-Khojin, A.; Thorson, M. R.; Zhu, W.; Whipple, D. T.; Kenis, P. J.; Masel, R. I., ***Science***, **2011**, *334*, 6056, 643-644.

(143) Hatsukade, T.; Kuhl, K. P.; Cave, E. R.; Abram, D. N.; Jaramillo, T. F., ***Phys. Chem. Chem. Phys.***, **2014**, *16*, 27, 13814-13819.

(144) Tamilarasan, P.; Ramaprabhu, S., ***J. Mater. Chem. A***, **2015**, *3*, 2, 797-804.

(145) Ampelli, C.; Centi, G.; Passalacqua, R.; Perathoner, S., ***Energy Environ. Sci.***, **2010**, *3*, 3, 292-301.

(146) Narayanan, S.; Haines, B.; Soler, J.; Valdez, T., ***J. Electrochem. Soc.***, **2011**, *158*, 2, A167-A173.

(147) Ma, S.; Sadakiyo, M.; Luo, R.; Heima, M.; Yamauchi, M.; Kenis, P. J. A., ***J. Power Sources***, **2016**, *301*, 219-228.

(148) Irtem, E.; Andreu, T.; Parra, A.; Hernández-Alonso, M. D.; García-Rodríguez, S.; Riesco-García, J. M.; Penelas-Pérez, G.; Morante, J. R., ***J. Mater. Chem. A***, **2016**, *4*, 35, 13582-13588.

(149) Xie, M. S.; Xia, B. Y.; Li, Y.; Yan, Y.; Yang, Y.; Sun, Q.; Chan, S. H.; Fisher, A.; Wang, X., ***Energy Environ. Sci.***, **2016**, *9*, 5, 1687-1695.

(150) Bagger, A.; Ju, W.; Varela, A. S.; Strasser, P.; Rossmeisl, J., ***ChemPhysChem***, **2017**, *18*, 22, 3266-3273.

(151) Seifitokaldani, A.; Gabardo, C. M.; Burdyny, T.; Dinh, C. T.; Edwards, J. P.; Kibria, M. G.; Bushuyev, O. S.; Kelley, S. O.; Sinton, D.; Sargent, E. H., ***J. Am. Chem. Soc.***, **2018**, *140*, 11, 3833-3837.

(152) Jin, L.; Seifitokaldani, A., ***Catalysts***, **2020**, *10*, 5, 481.

(153) De Luna, P.; Quintero-Bermudez, R.; Dinh, C.-T.; Ross, M. B.; Bushuyev, O. S.; Todorović, P.; Regier, T.; Kelley, S. O.; Yang, P.; Sargent, E. H., ***Nat. Catal.***, **2018**, *1*, 2, 103-110.

(154) Chen, Y.; Li, C. W.; Kanan, M. W., ***J. Am. Chem. Soc.***, **2012**, *134*, 49, 19969-72.

(155) Feaster, J. T.; Shi, C.; Cave, E. R.; Hatsukade, T.; Abram, D. N.; Kuhl, K. P.; Hahn, C.; Nørskov, J. K.; Jaramillo, T. F., ***ACS Catal.***, **2017**, *7*, 7, 4822-4827.

(156) Lu, Q.; Rosen, J.; Zhou, Y.; Hutchings, G. S.; Kimmel, Y. C.; Chen, J. G.; Jiao, F., ***Nat. Commun.***, **2014**, *5*, 1, 3242.

(157) Qi, L.; Jonathan, R.; Feng, J., ***ChemCatChem***, **2015**, *7*, 1, 38-47.

(158) Yan, C.; Li, H.; Ye, Y.; Wu, H.; Cai, F.; Si, R.; Xiao, J.; Miao, S.; Xie, S.; Yang, F.; Li, Y.; Wang, G.; Bao, X., ***Energy Environ. Sci.***, **2018**, *11*, 5, 1204-1210.

(159) Cheng, Y.; Zhao, S.; Johannessen, B.; Veder, J. P.; Saunders, M.; Rowles, M. R.; Cheng, M.; Liu, C.; Chisholm, M. F.; De Marco, R.; Cheng, H. M.; Yang, S. Z.; Jiang, S. P., ***Adv. Mater.***, **2018**, *30*, 13, 1706287.

(160) Dutta, A.; Rahaman, M.; Luedi, N. C.; Mohos, M.; Broekmann, P., ***ACS Catal.***, **2016**, *6*, 6, 3804-3814.

(161) Li, Y.; Cui, F.; Ross, M. B.; Kim, D.; Sun, Y.; Yang, P., ***Nano Lett.***, **2017**, *17*, 2, 1312-1317.

(162) Jiang, B.; Zhang, X. G.; Jiang, K.; Wu, D. Y.; Cai, W. B., ***J. Am. Chem. Soc.***, **2018**, *140*, 2880-2889.

(163) Zhang, Y.; Chen, L.; Li, F.; Easton, C. D.; Li, J.; Bond, A. M.; Zhang, J., ***ACS Catal.***, **2017**, *7*, 7, 4846-4853.

(164) Han, N.; Wang, Y.; Yang, H.; Deng, J.; Wu, J.; Li, Y.; Li, Y., ***Nat. Commun.***, **2018**, *9*, 1, 1320.

(165) Zhang, Y.; Li, F.; Zhang, X.; Williams, T.; Easton, C. D.; Bond, A. M.; Zhang, J., ***J. Mater. Chem. A***, **2018**, *6*, 11, 4714-4720.

(166) Zhang, X.; Li, F.; Zhang, Y.; Bond, A.; Zhang, J., ***J. Mater. Chem. A***, **2018**, *6*, 17, 7851-7858.

(167) Cheng, N.; Norouzi Banis, M.; Liu, J.; Riese, A.; Mu, S.; Li, R.; Sham, T.-K.; Sun, X., ***Energy Environ. Sci.***, **2015**, *8*, 5, 1450-1455.

(168) Wang, S.; Guan, B. Y.; Lou, X. W. D., ***J. Am. Chem. Soc.***, **2018**, *140*, 15, 5037-5040.

(169) Yan, G.; Le, Y.; Cheng‐Yang, W.; Zhan, L.; Wen, L. X., ***Adv. Funct. Mater.***, **2015**, *25*, 32, 5184-5189.

(170) Wang, S.; Guan, B. Y.; Lou, X. W., ***Energy Environ. Sci.***, **2018**, *11*, 2, 306-310.

(171) Verdaguer-Casadevall, A.; Li, C. W.; Johansson, T. P.; Scott, S. B.; McKeown, J. T.; Kumar, M.; Stephens, I. E.; Kanan, M. W.; Chorkendorff, I., ***J. Am. Chem. Soc.***, **2015**, *137*, 31, 9808-11.

(172) Lu, T.; Du, Z.; Liu, J.; Ma, H.; Xu, J., ***Green Chem.***, **2013**, *15*, 8, 2215.

(173) Saberi Safaei, T.; Mepham, A.; Zheng, X.; Pang, Y.; Dinh, C.-T.; Liu, M.; Sinton, D.; Kelley, S. O.; Sargent, E. H., ***Nano Lett.***, **2016**, *16*, 11, 7224-7228.

(174) Li, G.; Wang, X.; Seo, M. H.; Hemmati, S.; Yu, A.; Chen, Z., ***J. Mater. Chem. A***, **2017**, *5*, 22, 10895-10901.

(175) Baruch, M. F.; Pander, J. E.; White, J. L.; Bocarsly, A. B., ***ACS Catal.***, **2015**, *5*, 5, 3148-3156.

(176) Hassan, F. M.; Batmaz, R.; Li, J.; Wang, X.; Xiao, X.; Yu, A.; Chen, Z., ***Nat. Commun.***, **2015**, *6*, 8597.

(177) Hammer, B.; Nørskov, J. K., ***Adv. Catal.***, **2000**, *45*, 71-129.

(178) Zuckerman, J. J., Applications of119mSn Mössbauer Spectroscopy to the Study of Organotin Compounds. In *Adv. Organomet. Chem.*, Stone, F. G. A.; West, R., Eds. Academic Press: 1971; Vol. 9, pp 21-134.

(179) Asadi, M.; Kumar, B.; Behranginia, A.; Rosen, B. A.; Baskin, A.; Repnin, N.; Pisasale, D.; Phillips, P.; Zhu, W.; Haasch, R.; Klie, R. F.; Kral, P.; Abiade, J.; Salehi-Khojin, A., ***Nat. Commun.***, **2014**, *5*, 1, 4470.

(180) Qiu, B.; Cai, L.; Wang, Y.; Lin, Z.; Zuo, Y.; Wang, M.; Chai, Y., ***Adv. Funct. Mater.***, **2018**, *28*, 17, 1706008.

(181) Zhang, Y., ***Inorg. chem.***, **1982**, *21*, 11, 3886-3889.

(182) Wang, R.; Higgins, D. C.; Lee, D. U.; Prabhudev, S.; Hassan, F. M.; Chabot, V.; Lui, G.; Jiang, G.; Choi, J. Y.; Rasenthiram, L.; Fu, J.; Botton, G.; Chen, Z., ***Nano Energy***, **2016**, *20*, 57-67.

(183) Kresse, G.; Furthmüller, J., ***Phys. Rev. B***, **1996**, *54*, 16, 11169.

(184) Kresse, G.; Furthmüller, J., ***Comp. Mater. Sci.***, **1996**, *6*, 1, 15-50.

(185) Kresse, G.; Joubert, D., ***Phys. Rev. B***, **1999**, *59*, 3, 1758.

(186) White, J.; Bird, D., ***Phys. Rev. B***, **1994**, *50*, 7, 4954.

(187) Perdew, J. P.; Burke, K.; Ernzerhof, M., ***Phys. Rev. Lett.***, **1996**, *77*, 18, 3865.

(188) von Barth, U.; Hedin, L., ***J. Phys. C Solid State Phys.***, **1972**, *5*, 13, 1629.

(189) Shishkin, M.; Ziegler, T., ***J. Phys. Chem. C***, **2008**, *112*, 49, 19662-19669.

(190) Ren, B.; Dong, X.; Yu, Y.; Wen, G.; Zhang, M., ***Appl. Surf. Sci.***, **2017**, *412*, 374-384.

(191) Ren, B.; Dong, X.; Yu, Y.; Zhang, M., ***Surf. Sci.***, **2017**, *664*, 147-154.

(192) Sreekanth, N.; Phani, K. L., ***Chem. Commun.***, **2014**, *50*, 76, 11143-11146.

(193) Hori, Y.; Kikuchi, K.; Suzuki, S., ***Chem. Lett.***, **1985**, *14*, 11, 1695-1698.

(194) Bai, X.; Chen, W.; Zhao, C.; Li, S.; Song, Y.; Ge, R.; Wei, W.; Sun, Y., ***Angew. Chem. Int. Edit.***, **2017**, *56*, 40, 12219-12223.

(195) Rosen, B. A.; Hod, I., ***Adv. Mater.***, **2018**, *30*, 41, 1706238.

(196) Mariano, R. G.; McKelvey, K.; White, H. S.; Kanan, M. W., ***Science***, **2017**, *358*, 6367, 1187-1192.

(197) Cao, L.; Raciti, D.; Li, C.; Livi, K. J. T.; Rottmann, P. F.; Hemker, K. J.; Mueller, T.; Wang, C., ***ACS Catal.***, **2017**, *7*, 12, 8578-8587.

(198) Morales-Guio, C. G.; Cave, E. R.; Nitopi, S. A.; Feaster, J. T.; Wang, L.; Kuhl, K. P.; Jackson, A.; Johnson, N. C.; Abram, D. N.; Hatsukade, T.; Hahn, C.; Jaramillo, T. F., ***Nat. Catal.***, **2018**, *1*, 10, 764-771.

(199) Fu, J.; Zhu, W.; Chen, Y.; Yin, Z.; Li, Y.; Liu, J.; Zhang, H.; Zhu, J.; Sun, S., ***Angew. Chem. Int. Edit.***, **2019**, *58*, 40, 14100-14103.

(200) Zu, X.; Li, X.; Liu, W.; Sun, Y.; Xu, J.; Yao, T.; Yan, W.; Gao, S.; Wang, C.; Wei, S.; Xie, Y., ***Adv. Mater.***, **2019**, *31*, 15, 1808135.

(201) Li, X.; Bi, W.; Chen, M.; Sun, Y.; Ju, H.; Yan, W.; Zhu, J.; Wu, X.; Chu, W.; Wu, C.; Xie, Y., ***J. Am. Chem. Soc.***, **2017**, *139*, 42, 14889-14892.

(202) Xiao, M.; Zhu, J.; Li, G.; Li, N.; Li, S.; Cano, Z. P.; Ma, L.; Cui, P.; Xu, P.; Jiang, G.; Jin, H.; Wang, S.; Wu, T.; Lu, J.; Yu, A.; Su, D.; Chen, Z., ***Angew. Chem. Int. Edit.***, **2019**, *131*, 28, 9742-9747.

(203) Gao, D.; Zhang, Y.; Zhou, Z.; Cai, F.; Zhao, X.; Huang, W.; Li, Y.; Zhu, J.; Liu, P.; Yang, F.; Wang, G.; Bao, X., ***J. Am. Chem. Soc.***, **2017**, *139*, 16, 5652-5655.

(204) Saravanan, K.; Basdogan, Y.; Dean, J.; Keith, J. A., ***J. Mater. Chem. A***, **2017**, *5*, 23, 11756-11763.

(205) Mowbray, D. J.; Martínez, J. I.; Calle-Vallejo, F.; Rossmeisl, J.; Thygesen, K. S.; Jacobsen, K. W.; Nørskov, J. K., ***J. Phys. Chem. C***, **2010**, *115*, 5, 2244-2252.

(206) Gao, R.; Pan, L.; Wang, H.; Zhang, X.; Wang, L.; Zou, J.-J., ***ACS Catal.***, **2018**, *8*, 9, 8420-8429.

(207) Chen, Z.; Song, Y.; Cai, J.; Zheng, X.; Han, D.; Wu, Y.; Zang, Y.; Niu, S.; Liu, Y.; Zhu, J.; Liu, X.; Wang, G., ***Angew. Chem. Int. Edit.***, **2018**, *57*, 18, 5076-5080.

(208) Robinson, W. E.; Bassegoda, A.; Reisner, E.; Hirst, J., ***J. Am. Chem. Soc.***, **2017**, *139*, 29, 9927-9936.

(209) Yoon, Y.; Hall, A. S.; Surendranath, Y., ***Angew. Chem. Int. Edit.***, **2016**, *55*, 49, 15282-15286.

(210) Wang, S.; Guan, B. Y.; Lu, Y.; Lou, X. W. D., ***J. Am. Chem. Soc.***, **2017**, *139*, 48, 17305-17308.

(211) Liu, G.; Li, J.; Fu, J.; Jiang, G.; Lui, G.; Luo, D.; Deng, Y. P.; Zhang, J.; Cano, Z. P.; Yu, A.; Su, D.; Bai, Z.; Yang, L.; Chen, Z., ***Adv. Mater.***, **2019**, *31*, 6, 1806761.

(212) Park, M. G.; Lee, D. U.; Seo, M. H.; Cano, Z. P.; Chen, Z., ***Small***, **2016**, *12*, 20, 2707-2714.

(213) Tang, J.; Daiyan, R.; Ghasemian, M. B.; Idrus-Saidi, S. A.; Zavabeti, A.; Daeneke, T.; Yang, J.; Koshy, P.; Cheong, S.; Tilley, R. D.; Kaner, R. B.; Amal, R.; Kalantar-Zadeh, K., ***Nat. Commun.***, **2019**, *10*, 1, 4645.

(214) Miagava, J.; Rubbens, A.; Roussel, P.; Navrotsky, A.; Castro, R. H. R.; Gouvêa, D.; Rohrer, G., ***J. Am. Ceram. Soc.***, **2016**, *99*, 2, 631-637.

(215) Yang, H. G.; Sun, C. H.; Qiao, S. Z.; Zou, J.; Liu, G.; Smith, S. C.; Cheng, H. M.; Lu, G. Q., ***Nature***, **2008**, *453*, 7195, 638-641.

(216) Losurdo, M.; Suvorova, A.; Rubanov, S.; Hingerl, K.; Brown, A. S., ***Nat. Mater.***, **2016**, *15*, 9, 995-1002.

(217) Li, G.; Li, K.; Yang, L.; Chang, J.; Ma, R.; Wu, Z.; Ge, J.; Liu, C.; Xing, W., ***ACS Appl. Mater. Inter.***, **2018**, *10*, 44, 38117-38124.

(218) Xiang, R.; Peng, L.; Wei, Z., ***Chem. Eur. J.***, **2019**, *25*, 42, 9799-9815.

(219) Wan, J.; Chen, W.; Jia, C.; Zheng, L.; Dong, J.; Zheng, X.; Wang, Y.; Yan, W.; Chen, C.; Peng, Q.; Wang, D.; Li, Y., ***Adv. Mater.***, **2018**, *30*, 11, 1705369.

(220) Chen, I. L.; Wei, Y.-C.; Lu, K.-T.; Chen, T.-Y.; Hu, C.-C.; Chen, J.-M., ***Nanoscale***, **2015**, *7*, 37, 15450-15461.

(221) Chen, I. L.; Chen, T.-Y.; Hu, C.-C.; Lee, C.-H., ***J. Mater. Chem. A***, **2013**, *1*, 6, 2039-2049.

(222) Waychunas, G. A., ***Am. Mineral.***, **1987**, *72*, 1-2, 89-101.

(223) Joly, Y.; Bunău, O.; Lorenzo, J.-E.; Galera, R.-M.; Grenier, S.; Thompson, B. In *Self-consistency, spin-orbit and other advances in the FDMNES code to simulate XANES and RXD experiments*, J. Phys.: Conf. Ser., IOP Publishing: 2009; p 012007.

(224) Cabaret, D.; Bordage, A.; Juhin, A.; Arfaoui, M.; Gaudry, E., ***Phys. Chem. Chem. Phys.***, **2010**, *12*, 21, 5619-5633.

(225) Bunău, O.; Joly, Y., ***J. Phys.: Condens. Matter***, **2009**, *21*, 34, 345501.

(226) Bourke, J. D.; Chantler, C. T.; Joly, Y., ***J. Synchrotron Rad.***, **2016**, *23*, 2, 551-559.

(227) Yan, J. M.; Li, S. J.; Yi, S. S.; Wulan, B. R.; Zheng, W. T.; Jiang, Q., ***Adv. Mater.***, **2018**, *30*, 12, 1703038.

(228) Lu, Z.; Wang, B.; Hu, Y.; Liu, W.; Zhao, Y.; Yang, R.; Li, Z.; Luo, J.; Chi, B.; Jiang, Z.; Li, M.; Mu, S.; Liao, S.; Zhang, J.; Sun, X., ***Angew. Chem. Int. Edit.***, **2019**, *58*, 9, 2622-2626.

(229) Wang, J.; Huang, X.; Xi, S.; Lee, J. M.; Wang, C.; Du, Y.; Wang, X., ***Angew. Chem. Int. Edit.***, **2019**, *58*, 38, 13532-13539.

(230) Dou, H.; Jiang, B.; Xu, M.; Zhang, Z.; Wen, G.; Peng, F.; Yu, A.; Bai, Z.; Sun, Y.; Zhang, L.; Jiang, Z.; Chen, Z., ***Angew. Chem. Int. Edit.***, **2019**, *131*, 39, 14107-14113.

(231) Di, J.; Zhu, C.; Ji, M.; Duan, M.; Long, R.; Yan, C.; Gu, K.; Xiong, J.; She, Y.; Xia, J.; Li, H.; Liu, Z., ***Angew. Chem. Int. Edit.***, **2018**, *57*, 45, 14847-14851.

(232) Bao, J.; Zhang, X.; Fan, B.; Zhang, J.; Zhou, M.; Yang, W.; Hu, X.; Wang, H.; Pan, B.; Xie, Y., ***Angew. Chem. Int. Edit.***, **2015**, *127*, 25, 7507 –7512.

(233) Sosa-Hernández, E. M.; Montejano-Carrizales, J. M.; Alvarado-Leyva, P. G., ***Eur. Phys. J. D***, **2016**, *70*, 10, 208.

(234) Singh, M. R.; Goodpaster, J. D.; Weber, A. Z.; Head-Gordon, M.; Bell, A. T., ***Proc. Natl. Acad. Sci. U. S. A.***, **2017**, *114*, 42, E8812-E8821.

(235) Suter, S.; Haussener, S., ***Energy Environ. Sci.***, **2019**, *12*, 5, 1668-1678.

(236) Goyal, A.; Marcandalli, G.; Mints, V. A.; Koper, M. T. M., ***J. Am. Chem. Soc.***, **2020**, *142*, 9, 4154-4161.

(237) Dinh, C.-T.; García de Arquer, F. P.; Sinton, D.; Sargent, E. H., ***ACS Energy Lett.***, **2018**, *3*, 11, 2835-2840.

(238) Jouny, M.; Luc, W.; Jiao, F., ***Nat. Catal.***, **2018**, *1*, 10, 748-755.

(239) von Barth, U.; Hedin, L., ***J. Phys. C: Solid State Phys.***, **1972**, *5*, 13, 1629.

(240) Green, I. X.; Tang, W.; Neurock, M.; Yates, J. T., ***Science***, **2011**, *333*, 6043, 736-739.

(241) Chetri, P.; Basyach, P.; Choudhury, A., ***Chem. Phys.***, **2014**, *434*, 1-10.

(242) Zhuang, T.-T.; Pang, Y.; Liang, Z.-Q.; Wang, Z.; Li, Y.; Tan, C.-S.; Li, J.; Dinh, C. T.; De Luna, P.; Hsieh, P.-L.; Burdyny, T.; Li, H.-H.; Liu, M.; Wang, Y.; Li, F.; Proppe, A.; Johnston, A.; Nam, D.-H.; Wu, Z.-Y.; Zheng, Y.-R.; Ip, A. H.; Tan, H.; Chen, L.-J.; Yu, S.-H.; Kelley, S. O.; Sinton, D.; Sargent, E. H., ***Nat. Catal.***, **2018**, *1*, 12, 946-951.

(243) Whipple, D. T.; Finke, E. C.; Kenis, P. J., ***Electrochem. Solid St.***, **2010**, *13*, 9, B109-B111.

(244) Li, H.; Oloman, C., ***J. Appl. Electrochem.***, **2006**, *36*, 10, 1105.

(245) Dunwell, M.; Lu, Q.; Heyes, J. M.; Rosen, J.; Chen, J. G.; Yan, Y.; Jiao, F.; Xu, B., ***J. Am. Chem. Soc.***, **2017**, *139*, 10, 3774-3783.

(246) Bueno, P. R.; Leite, E. R.; Bulhões, L. O. S.; Longo, E.; Paiva-Santos, C. O., ***J. Eur. Ceram. Soc.***, **2003**, *23*, 6, 887-896.

(247) Jiao, H.; Jiao, S.; Song, W.-L.; Chen, H.; Wang, M.; Tu, J.; Fang, D., ***J. Electrochem. Soc.***, **2019**, *166*, 13, E401-E406.

(248) Chen, Y.; Lewis, N. S.; Xiang, C., ***Energy Environ. Sci.***, **2015**, *8*, 12, 3663-3674.

(249) Yang, H.; Lin, Q.; Zhang, C.; Yu, X.; Cheng, Z.; Li, G.; Hu, Q.; Ren, X.; Zhang, Q.; Liu, J.; He, C., ***Nat. Commun.***, **2020**, *11*, 1, 593.

(250) Thomas, G. T.; Pierre, B.; Adrian, M.; Victoria, M.-O.; Paul, R. S.; Dan, B.; Jens, E.; Jeff, G.; Antoni, F.-C., ***J. Electrochem. Soc.***, **2020**.

(251) Aghighi, M.; Hoeh, M. A.; Lehnert, W.; Merle, G.; Gostick, J., ***J. Electrochem. Soc.***, **2016**, *163*, 5, F384-F392.

(252) Kok, M. D. R.; Khalifa, A.; Gostick, J. T., ***J. Electrochem. Soc.***, **2016**, *163*, 7, A1408-A1419.

(253) Hashiba, H.; Weng, L.-C.; Chen, Y.; Sato, H. K.; Yotsuhashi, S.; Xiang, C.; Weber, A. Z., ***J. Phys. Chem. C***, **2018**, *122*, 7, 3719-3726.

(254) Verma, S.; Lu, X.; Ma, S.; Masel, R. I.; Kenis, P. J., ***Phys. Chem. Chem. Phys.***, **2016**, *18*, 10, 7075-84.

(255) Singh, M. R.; Papadantonakis, K.; Xiang, C.; Lewis, N. S., ***Energy Environ. Sci.***, **2015**, *8*, 9, 2760-2767.

(256) Weng, L. C.; Bell, A. T.; Weber, A. Z., ***Phys. Chem. Chem. Phys.***, **2018**, *20*, 25, 16973-16984.

(257) Resasco, J.; Chen, L. D.; Clark, E.; Tsai, C.; Hahn, C.; Jaramillo, T. F.; Chan, K.; Bell, A. T., ***J. Am. Chem. Soc.***, **2017**, *139*, 32, 11277-11287.

(258) Kok, M. D. R.; Jervis, R.; Tranter, T. G.; Sadeghi, M. A.; Brett, D. J. L.; Shearing, P. R.; Gostick, J. T., ***Chem. Eng. Sci.***, **2019**, *196*, 104-115.

(259) Wen, G.; Rehman, S.; Tranter, T. G.; Ghosh, D.; Chen, Z.; Gostick, J. T.; Pope, M. A., ***Chem. Mater.***, **2020**, *32*, 11, 4518–4526.

(260) Winkelmann, J., Diffusion coefficient of formic acid in water at infinite dilution. In *Diffusion in Gases, Liquids and Electrolytes*, Springer: 2018; pp 1946-1946.

(261) Cadogan, S. P.; Maitland, G. C.; Trusler, J. P. M., ***J. Chem. Eng. Data***, **2014**, *59*, 2, 519-525.

(262) Kallikragas, D. T.; Plugatyr, A. Y.; Svishchev, I. M., ***J. Chem. Eng. Data***, **2014**, *59*, 6, 1964-1969.

(263) Schulz, K. G.; Riebesell, U.; Rost, B.; Thoms, S.; Zeebe, R., ***Mar. chem.***, **2006**, *100*, 1-2, 53-65.